



Design and Analysis of Integrated Optical Waveguide Structures and their Coupling to Silicon-based Light Emitters

D I S S E R T A T I O N

zur Erlangung des akademischen Grades

**Doctor rerum naturalium
(Dr. rer. nat.)**

vorgelegt

**der Fakultät Mathematik und Naturwissenschaften
der Technischen Universität Dresden**

von

Dipl. nat. Susette Germer

geboren am 24.12.1986 in Grimma

Eingereicht am 03.12.2014

Die Dissertation wurde in der Zeit vom 01 / 2011 bis
12 / 2014 am Helmholtz-Zentrum Dresden-Rossendorf angefertigt.

Germer, Susette

Susette.Germer@gmail.com

24.12.1986 in Grimma, Matrikelnummer 3744123

TU Dresden, Fakultät Mathematik und Naturwissenschaften, Fachrichtung Physik

1. Hochschullehrer: Prof. Dr. Manfred Helm (TU Dresden)
2. Hochschullehrer: Prof. Dr. Heitmann (TU Bergakademie Freiberg)

Betreuer: Dr. habil. Lars Rebohle

Termin der Abgabe: 03.12.2014

ABSTRACT

A major focus is on integrated Silicon-based optoelectronics for the creation of low-cost photonics for mass-market applications. Especially, the growing demand for sensitive and portable optical sensors in the environmental control and medicine follows in the development of integrated high resolution sensors [1]. In particular, since 2013 the quick on-site verification of pathogens, like legionella in drinking water pipes, is becoming increasingly important [2, 3]. The essential questions regarding the establishment of portable biochemical sensors are the incorporation of electronic and optical devices as well as the implementations of fundamental cross-innovations between biotechnology and microelectronics.

This thesis describes the design, fabrication and analysis of high-refractive-index-contrast (Δn) photonic structures. Besides silicon nitride (Si_3N_4) strip waveguides, lateral tapers, bended waveguides, two-dimensional photonic crystals (PhCs) the focus lies on monolithically integrated waveguide butt-coupled Silicon-based light emitting devices (Si-based LEDs) [4, 5] for use as bioanalytical sensor components.

Firstly, the design and performance characteristics as single mode regime, confinement factor and propagation losses due to the geometry and operation wavelength ($\lambda = 1550$ nm, 541 nm) of single mode (SM), multi mode (MM) waveguides and bends are studied and simulated. As a result, SM operation is obtained for $\lambda = 1550$ nm by limiting the waveguide cross-section to $0.5 \mu\text{m} \times 1 \mu\text{m}$ resulting in modal confinement factors of 87 %. In contrast, for shorter wavelengths as $\lambda = 541$ nm SM propagation is excluded if the core height isn't further decreased. Moreover, the obtained theoretical propagation losses for the lowest-order TE/TM mode are in the range of 0.3 - 1.3 dB/cm for an interface roughness of 1 nm. The lower silicon dioxide (SiO_2) waveguide cladding should be at least $1 \mu\text{m}$ to avoid substrate radiations. These results are in a good correlation to the known values for common dielectric structures. In the case of bended waveguides, an idealized device with a radius of $10 \mu\text{m}$ was developed which shows a reflection minimum ($S_{11} = -22$ dB) at $\lambda = 1550$ nm resulting in almost perfect transmission of the signal. Additionally, tapered waveguides were investigated for an optimized light coupling between high-aspect-ratio devices. Here, adiabatic down-tapered waveguides were designed for the elimination of higher-order modes and perfect signal transmission.

Secondly, fabrication lines including Electron-beam (E-beam) lithography and reactive ion etching (RIE) with an Aluminum (Al) mask were developed and lead to well fabricated optical devices in the (sub)micrometer range. The usage of focused ion beam (FIB) milling is invented for smoother front faces which were analyzed by scanning electron microscopy (SEM) and atomic force microscopy (AFM). As a result, the anisotropy of the RIE process was increased, but the obtained surface roughness parameters are still too high (10 – 20 nm) demonstrating a more advanced lithography technique is needed for higher quality structures. Moreover, this study presents an alternative fabrication pathway for novel designed waveguides with free-edge overlapping endfaces for improving fiber-chip-coupling.

Thirdly, the main focus lies on the development of a monolithic integration circuit consisting of the Si-based LED coupled to an integrated waveguide. The light propagation between high-aspect-ratio devices is enabled through low-loss adiabatic tapers. This study shows, that the usage of CMOS-related fabrication technologies result in a monolithic manufacturing pathway for the successful implementation of fully integrated Si-based photonic circuits.

Fourth, transmission loss measurements of the fabricated photonic structures as well as the waveguide butt-coupled Si-based LEDs were performed with a generated setup. As a result, free-edge overlapping MM waveguides show propagation loss coefficients of $\alpha \sim 65$ dB/cm in the range of the telecommunication wavelength. The high surface roughness parameters (~ 150 nm) and the modal dispersion in the core are one of the key driving factors. These facts clearly underline the improvement potential of the used fabrication processes. However, electroluminescence (EL) measurements of waveguide butt-coupled Si-based LEDs due to the implanted rare earth (RE) ion (Tb^{3+} , Er^{3+}) and the host material (SiO_2/SiN_x) were carried out. The detected transmission spectra of the coupled $Tb:SiO_2$ systems show a weak EL signal at the main transition line of the Tb^{3+} -ion ($\lambda = 538$ nm). A second emission line was detected in the red region of the spectrum either corresponding to a further optical transition of Tb^{3+} or a Non Bridging Oxygen Hole Center (NBOHC) in SiO_2 . Unfortunately, no light emission in the infrared range was established for the Er^{3+} -doped photonic circuits caused by the low external quantum efficiencies (EQE) of the Er^{3+} implanted Si-based LEDs. Nevertheless, transmission measurements between 450 nm – 800 nm lead again to the result that an emission at $\lambda = 650$ nm is either caused by an optical transition of the Er^{3+} -ion or initialized by the NBOHC in the host. Overall, it is difficult to assess whether or not these EL signals are generated from the implanted ions, thus detailed statements about the coupling efficiency between the LED and the integrated waveguide are quite inadequate. Nevertheless, the principle of a fully monolithically integrated photonic circuit consisting of a Si-based LED and a waveguide has been successfully proven in this study.

KURZFASSUNG

Die Motivation dieser Arbeit begründet sich aus der stetig wachsenden Nachfrage an integrierten optoelektronischen Sensoren auf dem Weltmarkt. Speziell der Bedarf an sensitiven und portablen optischen Sensoren im Bereich der Überwachung der Umweltverschmutzung und Medizin führt zur Entwicklung integrierter hochauflösender Sensorsysteme [1]. Im Mittelpunkt stehen vor allem biochemische Sensoren, die optische und elektronische Komponenten vereinen, und zur Vorortanalyse von gesundheitsschädlichen Substanzen und Bakterien, wie z.B. Östrogen oder Legionellen im Trinkwasser [2, 3], eingesetzt werden können.

Gegenstand der vorliegenden Arbeit sind das Design, die Herstellung und Charakterisierung von Si_3N_4 -Streifenwellenleitern mit hohem Brechungsindexkontrast (Δn) und zweidimensionalen Photonischen Kristallen (PK). Im Vordergrund steht dabei deren Kopplung, u.a. über laterale Taper-Strukturen, mit Silizium-basierten Lichtemittern (Si-LEDs) [4, 5] auf Chipebene für anwendungsorientierte mikrooptische Systeme im Bereich der Sensorik und der Kommunikationstechnik. Die Designparameter der photonischen Strukturen werden optimiert, ihre Leistungsparameter analysiert und diskutiert.

Zunächst werden die Leistungsparameter, wie Monomode-Führung (SM), Confinement-Faktor und effektiver Brechungsindex, einzelner gerade und gebogener Streifenwellenleiter in Abhängigkeit der Geometrie und Wellenlänge (1550 nm, 541 nm) für SM und Multimode (MM) Betrieb theoretisch untersucht. Für den Einsatz im SM-Bereich und unter Verwendung der Telekommunikationswellenlänge ($\lambda = 1550$ nm) sollte der Querschnitt des Wellenleiterkerns bei $0.5 \times 1 \mu\text{m}^2$ liegen, damit eine starke Lichtführung (87 %) und minimale Ausbreitungsverluste (0.3 – 1.3 dB/cm) ermöglicht werden. Für kürzere Wellenlängen, wie z.B. $\lambda = 541$ nm, müsste die vertikale Ausdehnung weiter reduziert werden. Gebogene Strukturen mit Krümmungen im Bereich von $10 \mu\text{m}$ bei einer Wellenlänge von $\lambda = 1550$ nm zeigten ein optimales Transmissionsverhalten und ein Minimum in der Reflexion ($S_{11} = -22$ dB). Außerdem wurde die Lichtführung in Taper-Strukturen untersucht, wobei eine optimale Kopplung zwischen Sensoren-Komponenten mit stark verschiedenen Aspekt-Verhältnissen erzielt wurde.

Weiterhin wurde festgestellt, dass die genutzten Herstellungsverfahren auf Elektronenstrahlolithographie und reaktivem Ionenätzen (RIE) mit Aluminium-Maske (Al) basieren sollten, um verbesserte optische Strukturen im Submikrometer-Bereich zu erzeugen. Im Vordergrund stand dabei die Erhöhung der Anisotropie während des Ätzprozesses. Charakterisiert wurden die erhaltenen Streifenwellenleiter mittels Rasterkraftmikroskopie (AFM) und Rasterelektronenmikroskopie (REM), wobei Oberflächenrauigkeiten im Bereich von 10 - 20 nm festgestellt wurden. Zusätzliches Ionenstrahlschneiden (FIB) führte zur Glättung der Stirnseiten, womit Kopplungsverluste gesenkt werden können. Des Weiteren wurde ein alternativer Herstellungsablauf entwickelt, der erstmals zu Wellenleiterstrukturen mit freistehenden Stirnflächen führte, um die Faser-Chip-Kopplung deutlich zu verbessern.

Der Hauptfokus der vorgelegten Arbeit lag in der Entwicklung einer vollständigen monolithischen Integration des Si-basierten Lichtemitters mit einem Wellenleiter, welche mittels CMOS Herstellungstechnologien erzielt werden konnte. Der damit zu Grunde liegende Neuheitsgrad dieser Arbeit wird durch die Umsetzung auf Chipebene verdeutlicht. Der Einsatz von Tapern unterstützt zusätzlich die Kopplungsproblematik bezüglich der Verbindung von Bauelementen mit stark unterschiedlichen Aspekt-Verhältnissen. Damit ist

eine Anwendung in Richtung Lab-On-Chip Applikationen möglich, wie z.B. Biosensoren, welche vor allem schnelle Vorortmessungen und Analysen wünschen.

Weiterhin wurden die optischen und elektrischen Eigenschaften der integrierten Lichtquelle untersucht, um eine Aussage über die Effizienz des integrierten photonischen Systems machen zu können. Die externe Leistungseffizienz dieser liegt theoretisch zwischen 5 % und 10 %, wobei eine externe Quanteneffizienz von 14 % und 16 % in vergangenen Arbeiten gemessen wurde [4, 5]. Trotz dieser niedrigen Werte, im Vergleich mit einer Laserdiode, kann theoretisch eine Kopplungseffizienz zwischen Wellenleiter und Si-LED von 40 % erreicht werden. Das liegt vor allem an dem hohen Brechungsindexkontrast des Wellenleiters, wodurch eine große numerische Apertur entsteht, die zu weiten Einstrahlwinkeln führt. Weiterhin sollte die untere SiO₂ Schicht eine Mindestdicke von 1 μm aufweisen, damit Strahlungsverluste ins Si Substrat minimiert werden.

Abschließend wurden für die Charakterisierung der Transmissionsverluste in den Streifenwellenleiter und den gekoppelten Si-LEDs spezielle Messplätze aufgebaut. Dabei ergaben sich für die untersuchten MM-Wellenleiterstrukturen mit freistehenden Stirnflächen Ausbreitungsverluste von $\alpha \sim 65$ dB/cm im Bereich der Telekommunikationswellenlänge. Der Gründe dafür liegen vor allem in den hohen Seitenwandrauigkeiten und der Modendispersion im Kern. Trotzdem stimmen diese gute mit den theoretischen Werten überein. Damit wird wiederum klar, dass die verwendeten Herstellungsprozesse ein deutliches Verbesserungspotential aufweisen, aber andererseits ein alternativer Weg für das Problem der Faser-Chip-Kopplung gefunden wurde. Des Weiteren wurden Elektrolumineszenz (EL) Messungen der hergestellten Wellenleiter gekoppelten Si-LEDs in Abhängigkeit des implantierten Ions (Er³⁺, Tb³⁺) und des Matrix-Materials (SiO₂, SiN_x) durchgeführt. Die gemessenen Transmissionspektren der Tb:SiO₂ Systeme zeigten dabei schwache EL Signale im Bereich der Hauptemissionslinie des Tb³⁺-Ions. Außerdem wurde ein zweites Signal bei $\lambda = 650$ nm gemessen, welches entweder einem weiteren optischen Übergang des Ions oder einem nicht-brückenbildenden Sauerstoff im SiO₂ entspricht. Leider, konnte bei den Er³⁺-Systemen keine Emission im Bereich der Telekommunikationswellenlänge beobachtet werden, was entweder auf eine missglückte Kopplung der Bauelemente oder auf die geringe externe Quanteneffizienz des Er³⁺-dotierten LEDs zurückzuführen ist. Jedoch wurden Transmissionsmessungen im Bereich von 450 nm – 800 nm durchgeführt, wobei erneut das EL Signal bei $\lambda = 650$ nm detektiert wurde. Die Ursache dafür liegt wiederum entweder im optischen Übergang des Er³⁺-Ions im sichtbaren Bereich des Spektrums oder an den Sauerstoffdefektzentren im Matrix-Material. Konkrete Aussagen über die Herkunft des Signals und die damit verbundene Kopplungseffizienz zwischen dem Si-basierten Lichtemitter und dem integrierten Wellenleiter sind daher nur schwer möglich und erfordern weitere Untersuchungen in der Zukunft. Zusammenfassend lässt sich sagen, dass erstmals eine monolithische Integration des wellenleitergekoppelten Lichtemitters mittels CMOS Technologien erfolgreich umgesetzt wurde.

DANKSAGUNG

Ich bin der Meinung, dass man diesen viel zu kurz kommenden Abschnitt in einer Dissertation etwas mehr Beachtung schenken sollte; und das eine Umbenennung in "*How can you live four years without seeing the light at the end of the tunnel?*" wohl eher den Zustand des Danksagenden unterstreicht und die Bedeutung des u.a. familiären Rückhalts hervorhebt.

Wie auch immer, ich bin froh und kann mein Glück kaum fassen. Ich freue mich darüber, dass ich tatsächlich erreicht habe, was ich mir erhofft hatte - und das alles nur, weil es Menschen gibt, die mir im Labyrinth des Forscherdaseins mit Wegweisern zur Seite gestanden haben. Dabei stelle ich fachlichen Beistand und private Unterstützung auf eine Stufe.

Dank gilt zunächst meinen beiden Gutachtern, Prof. M. Helm und Prof. J. Heitmann, die sich die Zeit genommen haben diese Arbeit mit Interesse zu lesen. Außerdem möchte ich mich bei Dr. W. Skorupa und Dr. habil. L. Rebohle bedanken, da beide immer ein offenes Ohr für mich hatten und mir mit vielen Ratschlägen sowie ihrem großen Erfahrungsschatz zur Seite standen. Die Prozessierungs- und Messergebnisse dieser Arbeit wären ohne die Ausdauer von C. Neisser und B. Scheumann sowie der Firma GeSim nicht möglich gewesen. Die strukturellen Untersuchungen konnten u.a. durch Hilfe von E. Christalle, R. Wutzler und A. Mrotzek erzielt werden. Dank des Expertenwissens von Dr. A. Madani (IFW, Dresden) wurden die optischen Charakterisierungen der Wellenleiter erst möglich gemacht.

Der unbeschreiblich starke familiäre Rückhalt stellt die Grundlage für die erfolgreiche Fertigstellung dieser Arbeit dar - ein Gruppenticket für diese Achterbahnfahrt wurde gelöst. Deshalb bin ich der Meinung, dass die menschliche Unterstützung des engsten Kreises, sowie meiner Freunde und Kollegen das fundamentale Werkzeug bilden, um letztendlich das Ende des Tunnels zu erreichen und diesen Lebensabschnitt unvergesslich gestalten.

Mein Opa hat's verdient.

Danke!

CONTENS

Abstract	I
Kurzfassung.....	III
Danksagung	V
Puplications & Conference Contributions	IX
List of Figures	X
List of Tables	XII
List of Symbols and Acronyms	XIII
1 Introduction.....	1
1.1 Background.....	1
1.2 Thesis Objectives.....	2
2 Si-based integrated optics	3
2.1 Integrated Optical Sensors	3
2.2 Theory of Waveguiding	4
2.2.1 Planar Waveguides	4
2.2.2 Channel Waveguides and Bends	10
2.2.3 Photonic Crystal Structures.....	15
2.3 Coupling to the Optical Circuit	18
2.3.1 End-fire and Butt-Coupling	20
2.3.2 Prism and Grating Coupling	23
2.3.3 Tapered Waveguides	24
2.4 Losses in Integrated Optical Waveguides	25
3 Simulation Tools used in Design	30
3.1 Matlab.....	30
3.2 Effective Refractive Index Method (ERIM).....	30
3.3 Finite Element Method (FEM)	31
4 Simulation and Design	33

4.1	System Design and Integration Scheme	33
4.1.1	Si-based LED as Light Source	34
4.1.2	Waveguide Design and Coupling Techniques	36
4.1.2.1	SM/MM Waveguides and Bends	36
4.1.2.2	Tapered Waveguides and Photonic Crystals	51
4.1.2.3	Butt-Coupled Si-based Light Emitters	54
5	Fabrication Methods.....	58
5.1	Si-based Light Emitters	59
5.2	Si-based Photonic Structures.....	60
5.2.1	Waveguides, Tapers and Photonic Crystals	60
5.2.2	Butt-Coupled Si-based Light Emitters.....	64
6	Characterization Methods.....	66
6.1	Si-based Light Emitters	66
6.1.1	I(V) and Electroluminescence Measurements	66
6.2	Si-Based Photonic Structures	67
6.2.1	Structural Characteristics.....	67
6.2.2	Transmission Measurements.....	70
7	Results.....	72
7.1	Si-based Light Emitters	72
7.2	Si-based Photonic Structures.....	75
7.3	Butt-Coupled Si-based Light Emitters	84
8	Summary	89
8.1	Reflections	89
8.2	Conclusion	90
9	Future Prospects	91
10	List of Literature	92
11	Source Code MATLAB.....	106
12	Eidesstattliche Erklärung	109

PUBLICATIONS & CONFERENCE CONTRIBUTIONS

- [1] J. Fiedler, V. Herra, R. Hübner, M. Voelskow, S. Germer, B. Schmidt, W. Skorupa, "High-fluence Ga-implanted silicon - The effect of annealing and cover layers," *Journal of Applied Physics* **116**, 024502 (2014). [doi: 10.1063/1.4887450]
- [2] S. Germer, L. Rebohle, W. Skorupa, *Patent* 6453-p1306-130514, 25 4 2013 (submitted)
- [3] S. Germer, C. Cherkouk, L. Rebohle, M. Helm, W. Skorupa, "Basic structures of integrated photonic circuits for smart biosensor applications," *SPIE Proceedings* **8744 Optical Sensors** 87740P (2013). [doi: 10.1117/12.2014920]
- [4] S. Germer, C. Cherkouk, L. Rebohle, M. Helm, W. Skorupa, "Si-based light emitter in an integrated photonic circuit for smart biosensor applications," *SPIE Proceedings* **8767 Integrated Photonics: Materials, Devices, and Applications II** (2013). [doi: 10.1117/12.2017275]
- [5] L. Rebohle, R. Wutzler, S. Germer, J. Lehmann, M. Helm, W. Skorupa, "Er- and Nd-implanted MOS light emitting devices and their use for integrated photonic applications," *SPIE Proceedings* **8431 Silicon Photonics and Photonic Integrated Circuits III** 843116 (10 May 2012). [doi: 10.1117/12.921755]
- [6] S. Germer, „Silizium-Photonik: Fusionsfeld für Mikroelektronik und Biotechnologie,“ *8. Technologietag Mitteldeutschland*, Dresden, Germany, 2014 (invited talk)
- [7] S. Germer, L. Rebohle, M. Helm and W. Skorupa, "Basic structures of integrated photonic circuits for smart biosensor applications," *SPIE Optics and Optoelectronics*, Prague, Czech Republic, 2013 (talk)
- [8] S. Germer, L. Rebohle, M. Helm and W. Skorupa, "Si-based light emitter in an integrated photonic circuit for smart biosensor applications," *SPIE Microtechnologies*, Grenoble, France, 2013 (poster)
- [9] S. Germer, L. Rebohle, M. Helm and W. Skorupa, "Basic structures of integrated photonic circuits for smart biosensor applications," *2 th Doctoral students conference on optics – DocDoc*, Jena, Germany, 2012 (poster)
- [10] S. Germer, L. Rebohle, M. Helm and W. Skorupa, "Si-based light emitters in integrated photonic circuits for smart biosensor applications," *DPG Spring Meeting*, Stuttgart, Germany, 2012 (talk)
- [11] C. Günz, S. Germer, J. Lehmann, L. Rebohle, M. Helm, W. Skorupa, "Investigation of rare earth implanted SiO₂ thin films for Down-conversion applications in Photovoltaic's," *International topical workshop on Subsecond thermal processing of Advanced Materials – SubTherm*, Dresden, Germany, 2011 (poster)
- [12] S. Germer, L. Rebohle, M. Helm and W. Skorupa, "Si-based light emitters in integrated photonic circuits for smart biosensor applications," *1th Doctoral students conference on optics – DocDoc*, Jena, Germany, 2011 (poster)

LIST OF FIGURES

TIR AT TWO INTERFACES DEMONSTRATING THE CONCEPT OF A SLAB WAVEGUIDE.....	5
WAVE REPRESENTATION OF TE AND TM MODES IN A PLANAR WAVEGUIDE.....	5
WAVE REPRESENTATION OF TE- AND TM-LIKE MODES IN A CHANNEL WAVEGUIDE.....	11
REPHENSIVE CHANNEL WAVEGUIDES.....	11
FIELD PROFILES FOR THE FUNDAMENTAL MODES IN A RECTANGULAR WAVEGUIDE	13
WAVEGUIDE 90° - BEND WITH A DISTORTED LATERAL MODE SHAPE AND A CONNECTED STRAIGHT WAVEGUIDE.....	14
PHOTONIC CRYSTAL STRUCTURES OF DIFFERENT DIMENSIONS	15
ONE-DIMENSIONAL PHC	15
TWO-DIMENSIONAL PHCs	16
BAND DIAGRAM OF THE BULK PHC WITH A POINT DEFECT	17
COUPLING TECHNIQUES	18
RADIATION APERTURE OF A WAVEGUIDE FOR DIFFERENT ANGLES OF INPUT COUPLING.....	19
SCHEMA OF BUTT-COUPLING A LASER DIODE/WAVEGUIDE WITH AN INTEGRATED 2. WAVEGUIDE	21
LATERAL DOWN/UP- AND VERTICAL UP-TAPERED WAVEGUIDES	24
BAND GAP (E_G) BEHAVIOR FOR Si_3N_4 FILMS WITH DIFFERENT Si EXCESS	26
SCHEMATIC DIAGRAM OF THE TRANSMISSION LOSS MECHANISM IN SOI-BASED OPTICAL FIBERS.....	28
GENERALIZED RECTANGULAR WAVEGUIDE.....	31
THREE DIFFERENT Si-BASED INTEGRATED PHOTONIC CIRCUITS.....	33
SCHEMATIC CROSS-SECTION OF Si-BASED LEDs	35
NORMALIZED EL SPECTRA OF Gd^{3+} , Tb^{3+} , Eu^{3+} , Nd^{3+} AND Er^{3+} -IMPLANTED Si-BASED LEDs.....	35
TWO DIFFERENT BUTT-COUPLING METHODS	36
PROPAGATION ANGLES FOR FUNDAMENTAL TE/TM ($m = 0$).....	37
NORMALIZED DISPERSION V-B PLOTS.....	39
CALCULATED N_{EFF} VALUES	41
VARIATIONS OF THE SCATTERING LOSSES	42
ERIS OF THE QUASI-TE AND TM MODES FOR Si_3N_4	43
CALCULATED ERIS OF THE QUASI-TE AND TM MODES FOR Si_3N_4 WAVEGUIDES.....	44
OBTAINED MODE PROFILES FOR $0.5 \times 1 \mu m^2$ Si_3N_4 -WAVEGUIDES AT 1550 NM BY COMSOL.....	45
OBTAINED MODE PROFILES $0.5 \times 1 \mu m^2$ Si_3N_4 -WAVEGUIDES AT 541 NM BY COMSOL.....	46
INFLUENCE OF THE BOX LAYER THICKNESS	46
MODE PROFILE OF THE TE0 MODE	47
OBTAINED MODE PROFILES FOR TRAPEZOIDAL WAVEGUIDES	48
OBTAINED MODE PROFILES OF THE ESTIMATED RECTANGULAR WAVEGUIDES	49
FUNDAMENTAL MODE PROFILES OF CURVED WAVEGUIDES WITH DIFFERENT BEND RADII.....	50
S-PARAMETERS PLOT (DB) AS FUNCTIONS OF THE FREQUENCY	51
LIGHT PROPAGATION IN SHORT (NON-ADIABATIC) AND LONG (ADIABATIC) Si_3N_4 TAPERS	52

PROPAGATION OF THE TE ₀ -LIKE MODE.....	53
IN-PLANE TE WAVE PROPAGATION IN 2D PHC WAVEGUIDES	54
STRUCTURE OF THE TWO LEDs BUTT-COUPLED TO AN INTEGRATED WAVEGUIDE	55
PROCESSING SCHEME FOR THE FABRICATION OF SI-BASED LEDs.....	59
SCHEMATICS SHOWING THE FABRICATION STEPS OF THE PHOTOLITHOGRAPHY	61
SCHEMATICS SHOWING THE FABRICATION STEPS OF FREE EDGE-OVERLAPPING STRIP WAVEGUIDES.....	62
FABRICATION LINE OF THE OPTICAL DEVICES FABRICATED BY E-BEAM LITHOGRAPHY	63
FABRICATION SCHEME FOR WAVEGUIDE BUTT-COUPLED SI-BASED LIGHT EMITTERS	64
MEASUREMENT SETUP WITH AN OPTOMETER AT THE DARKBOX	66
SPECTRALLY RESOLVED EL MEASUREMENTS WITH A MICROSCOPE	67
ELLIPSOmetry SETUP	68
SCHEMA OF A SCANNING ELECTRON MICROSCOPE	69
SCHEMA AND FUNCTIONING OF AN ATOMIC FORCE MICROSCOPE	69
TRANSMISSION MEASUREMENT SETUP	70
TRANSMISSION MEASUREMENT SETUP WITH SPECIAL LENSED FIBER	71
I(V) CURVES OF ER:SiO ₂ LEDs WITH AL TOP ELECTRODE	72
I(V) CURVES OF ER:SiO ₂ LEDs.....	73
EL SPECTRUM OF Tb:SiO ₂ LEDs WITH ITO FRONT ELECTRODES	73
EL SPECTRUM WITH THE MOST COMMON TRANSITION STATES	74
EL SPECTRUM OF ER:SiN _x LEDs.....	75
DISPERSION CURVES OF THE DEPOSITED SiO ₂ , Si ₃ N ₄ AND IMPLANTED SiN _x LAYERS.....	76
3 x 3 μM SCAN OF A Si ₃ N ₄ -BASED FABRICATED WAVEGUIDE WITH A CROSS-SECTION OF 0.5 x 1 μM ²	77
SM/MM WAVEGUIDES.....	78
SM WAVEGUIDES (1 x 1 μM ²)	79
SEM PICTURE OF FREE EDGE-OVERLAPPING STRIP WAVEGUIDES.....	79
STRAIGHT WAVEGUIDES FABRICATED BY E-BEAM LITHOGRAPHY AND RIE	80
TAPERED AND BENDED WAVEGUIDE.....	81
SMOOTHED WAVEGUIDE FRONTS BY FIB TECHNIQUE	82
PROCESSED TWO-DIMENSIONAL PHC.....	82
MEASUREMENT RESULTS OF A MM WAVEGUIDE (1 x 50 μM ²).....	83
BUTT-COUPLED SI-BASED LEDs.....	84
EL SPECTRA OF MEASURED VERTICAL EL INTENSITY.....	85
EL SPECTRA OF DEVELOPED Tb:SiN _x LEDs WITH INTEGRATED SM OR MM WAVEGUIDES	86
EL SPECTRA OF WAVEGUIDE COUPLED ER:SiO ₂ AND ER:SiN _x LEDs.....	87

LIST OF TABLES

TABLE 1: SUMMARY OF THE OBTAINED VALUES FROM FIGURE 22 (A, B)	38
TABLE 2: SUMMARY OF THE OBTAINED VALUES FROM FIGURE 22 (A, B)	38
TABLE 3: SUMMARY OF THE OBTAINED VALUES FROM FIGURE 22 (C, D)	38
TABLE 4: SUMMARY OF THE OBTAINED VALUES FROM FIGURE 22 (C, D)	39
TABLE 5: V NUMBERS, B VALUES AND CRITICAL HEIGHTS H_{MAX}	40
TABLE 6: ERI'S OF THE FIRST LOW-ORDER MODES IN AN ASYMMETRICAL WAVEGUIDE	41
TABLE 7: OPTICAL PARAMETERS N_{EFF} , B AND Γ_{MODE} FOR A CROSS-SECTION OF $0.5 \times 1 \mu m^2$ AT 1550 NM	45
TABLE 8: OVERVIEW OF THE ORIGINAL RECTANGULAR WAVEGUIDE	48
TABLE 9: ELLIPSOMETRY DATA OF THE DEPOSITED LAYERS DUE TO THE IMPORTANT WAVELENGTHS	76

LIST OF SYMBOLS AND ACRONYMS

AFM	Atomic Force Microscopy
α	Transmission loss coefficient
CMOS	Complementary Metal-Oxide-Semiconductor
Δn	Refractive Index Difference
E-Beam lithography	Electron-Beam lithography
EL	Electroluminescence
Er	Erbium
ERIM	Effective Refractive Index Method
ERI	Effective Refractive Index
EQE	External Quantum Efficiency
f	Frequency
FEM	Finite Element Method
FIB milling	Focused Ion Beam milling
h	Core Height
h_{\max}	Critical Height
ITO	Indium Thin Oxide
$I(V)$	Current(Voltage)
λ	Wavelength
LOCOS	Local Oxidation of Silicon
LPCVD	Liquid Phase Chemical Vapor Depositor
MM	Multimode
MFD ($2 \omega_0$)	Mode Field Diameter
NA	Numerical Aperture
n_{eff}	Effective Refractive Index
NBOHC	Non Bridging Oxygen Hole Centre
PhC	Photonic Crystal
RE	Rare Earth
RIE	Reactive Ion Etching
RI	Refractive Index
REM	Rasterelektronenmikroskopie
S-parameter	Scattering parameter
SEM	Scanning Electron Microscopy
SM	Single mode
Si	Silicon
Si-based LED	Silicon-based Light Emitter
Si_3N_4	Silicon Nitride
SiO_2	Silicon Dioxide
SiON	Silicon Oxy Nitride
SiN_x	Silicon Nitride (12 % Si excess)
SOI	Silicon-On-Insulator
Tb	Terbium
TE mode	Transversal Electric mode
TEM	Transverse Electro Magnetic
TM mode	Transversal Magnetic mode
TIR	Total Internal Reflection
V	Normalized frequency
w	Core Width

1 INTRODUCTION

1.1 BACKGROUND

The rapidly growing demand for integrated sensors with increased performance, miniaturization and lower cost in the medical diagnostics, healthcare market, environmental control, pharmaceutical and food industries is the motivation for Si-based optoelectronics [1, 2]. This far-ranging technology takes aims at the advantage of the cost-effectiveness and known performance characteristics of Si-based electronic components, like light emitting devices [4, 5] and detectors, by integrating optical components, e.g. waveguides or PhCs, on portable and wireless Si-based platforms [6, 7, 8, 9, 10].

The common analytical technologies are based on non-portable laboratory systems as gas-liquid-chromatography with additional sample preparation steps and long analysis times. Thus the development of sensor applications focused more and more on lab-on-chip technologies, which benefit from the advantages of current silicon technology, like resource savings and large-scale production by the usage of CMOS fabrication techniques. On-chip integrated designs are the main objective that allows participating in key aspects of the global photonics industry, such as the 1.3 μm and 1.55 μm telecommunication systems. New concepts and practical issues for accomplishing complete miniature sensor modules for chemical and biochemical applications have been demonstrated and constitute the basic building blocks for the implementation of all-Si integrated photonic and optoelectronic circuits [11, 12, 13, 14, 15, 16, 17, 18].

The main drawback of optical biosensors relates to the unresolved manufacturability issues encountered when attempting monolithic integration of the light source and the detector [19, 20]. Most of these optical sensing devices were realized by coupling the light from an external laser diode via a waveguide or optical fiber into a photo detector [21, 22, 23]. Furthermore, the evanescent field of the guided light in the waveguide structure excites a specified dye-labeled antigen (analyte) which is immobilized by its antibody on the functionalized waveguide surface. The detection of the fluorescence in such systems requires the difficult handling of an expensive dye. Additionally, the portability is limited by the external laser and/or detector. However, precise positioning is relevant for best signal achievement.

Previously, a realized sensor concept [5, 3, 24] showed the high potential of the Si-based LED working as the light source for the development of a smart biosensing system, which allows miniaturization effects, cost savings and an increased portability. Further miniaturization and integration of more essential system units, e.g. a waveguide and a photodiode, can be achieved by a basic structure of an integrated photonic circuit to combine microelectronic and optical components.

1.2 THESIS OBJECTIVES

A large part of this thesis is devoted to the design and fabrication of high-index-contrast strip waveguides, waveguide bends, two-dimensional PhCs, lateral tapers as optical interconnects and butt-coupled Si-based LEDs according to the operation wavelengths of 541 nm and 1550 nm. The optimized fabrication processes are based on well-developed CMOS integration technologies, e.g. E-beam lithography and RIE, on silicon substrates. Characterizations of the manufactured photonic structures are carried out by AFM and SEM as well as by transmission measurements via end-fire coupling. In more details the objectives were:

1. To design, analyze and fabricate high-performance photonic structures like straight and bended waveguides, lateral tapers as well as two-dimensional PhCs for SM and MM operation at 1550 nm and 541 nm,
2. To develop an integration pathway for the fabrication of waveguide butt-coupled Si-based LEDs on a silicon substrate,
3. To characterize the fabricated photonic structures as well as the waveguide butt-coupled Si-based LEDs by a generated transmission measurement setup for optical loss characteristics.

In Chapter 2 a general overview of Si-based integrated optics, as waveguides and PhCs is given. Their propagation theory and losses as well as common coupling techniques are presented.

Chapter 3 contains innovative theoretical methods and principal simulation techniques that have been used in this thesis to design and analyse photonic structures and coupled optoelectrical devices.

Chapter 4 gives a general idea of the integrated photonic circuit with its microelectronic and optical components. Besides theoretical investigations of different photonic structures the coupling concept to integrated Si-based LEDs is explained too.

Chapter 5 deals with the fabrication techniques for the manufacturing of the Si-based LEDs, photonic structures and the integrated photonic circuit.

Chapter 6 looks at main experimental methods, e.g. current-voltage (I(V)) and electroluminescence (EL) techniques for the characterization of fabricated Si-based LEDs as well as the used Scanning Electron Microscopy (SEM), Atomic Force Microscopy (AFM) and ellipsometry measurements for structural analysis of the manufactured photonic devices and butt-coupled LEDs. Additionally, a special transmission measurement setup for optical loss characteristics is also presented.

Chapter 7 presents the measurement results of the fabricated Si-based LEDs, photonic structures and the integrated photonic circuit.

Chapter 8 summarizes and evaluates the main findings of this work and gives some future prospects.

2 SI-BASED INTEGRATED OPTICS

The combination of silicon and optics technologies benefits many applications. Researchers released in the middle of the 20th century first papers about “integrated optics” based on the development of the semiconductor laser and low-loss optical fibers [25]. Especially, Shubert and Harris discussed the “potential use of optical waveguides in signal processing and in laser beam circuitries” [25, 26]. Furthermore, integrated optics can combine both the classical advantages of optics, like less signal degradation and portability, and the advantages of integration, e.g. circuit miniaturization and low cost mass production, which are important for the development of integrated optical sensors [27].

This chapter gives a short overview of integrated optical sensor applications, particularly in the field of biological and chemical analysis. Especially, it provides some insight to basic waveguide and PhCs structures as essential building blocks in integrated optoelectronic circuits. An overview of photonic structures that are going to be used in this work is presented, as well as their fundamentals of light propagation. Their optical losses are discussed together with ways to measure them and characterization methods of optical waveguides by common techniques are shown.

2.1 INTEGRATED OPTICAL SENSORS

Two of the main electronic elements on a chip are: transistors to perform logical operations and interconnects for transferring data. The performance of transistors is continuously being improved and described by “Moore’s Law”. The interconnect performance in the past did not get better by shrinking of their dimensions. For this reason, ultimate limitations of electrical interconnects have physical origins and are very difficult to improve by the changing the technology. Therefore, it is essential to replace them by optical waveguides. The research in integrated optics has been driven mostly by the success of the optical fiber technology in telecommunication. The first integration of waveguides and electrical components on the same chip by the usage of a standard 90 nm semiconductor process was done by IBM in 2012 [28]. This investigation allows cheap chip-to-chip as well as computer-to-computer interconnects with speeds up to petabytes pro second.

Furthermore, the development of chemical and biological sensors creates a significant field of science and technology dedicated to the generation of integrated optical devices for monitoring chemical reactions at surfaces. Integrated optical sensors show a high potential for portable, low-cost and miniaturized “lab-on-chip” systems for analysis in the fields of monitoring state of health, food contamination, and environmental pollution. As already mentioned, the field of sensing contains many different quantities to measure for which reason the market is fragmented.

The major sensing mechanisms are fluorescence [29], absorption [30] and refractive index (RI) sensing [31, 32, 3]. The most common mechanism is the RI sensing which involves the detection of a wavelength shift according to the binding of macromolecules, small molecules or nanoparticles which results in a RI change of the light guiding waveguide material. Hence, the key element in every photonic circuit is the waveguide. Optical waveguides, like planar and fiber-optic, are based on a core material with high RI surrounded by materials with lower RIs, such as a substrate and the media to be sensed. This arrangement provides coupled light to propagate through the core by total internal reflection (TIR). Most of the light is confined in the guiding layer, but a small portion, named evanescence field, extends out into the substrate and the sensing medium, e.g. the biological sample. The amplitude of this field falls exponentially as the distance from the waveguide surface increases and vanishes at a distance around one-half

the wavelength of the coupled light [33, 34, 35]. The concept of waveguide-based sensors was initially reported by Lukosz and Tiefenthaler in 1983 [36]. It is based on high Δn SiO₂-TiO₂ waveguides with incoupling gratings for humidity measurements. Over time, optoelectrical sensing is now well established and sensor systems based on different photonic structures have been developed and demonstrated by numerous investigators. Especially, the usage of Si-based waveguides is a popular strategy, thus the band gap of Si (~ 1.1 eV) is such that the material is transparent to wavelengths commonly used for optical communication (1.3 – 1.6 μm) [34]. Furthermore, the standard CMOS processing techniques allow the design of optical waveguides onto the Si surface.

However, the main hindrance in developing integrated optical sensors is the investigation of integration schemes regarding the structural and technological differences between single optical and electronic components. Thus, optical structures should be monolithically integrated by fabrication processes which are compatible to the whole circuit and require no damaging steps to the host substrate, e.g. Si or Silicon-On-Insulator (SOI). For this reason, a relatively simple design of all components as a suitable optical source and a detector is necessary, too.

2.2 THEORY OF WAVEGUIDING

The following section describes the fundamentals of modes in one and two-dimensional optical waveguides, propagation constants (β , $k_{y,z}$) which lead on to the concept of effective refractive indices (ERI), mode field diameters and geometry parameters for SM and MM wave excitation. Additionally, the theory of light propagation in waveguide bends and PhCs is discussed.

2.2.1 Planar Waveguides

To fully understand the light propagation in an optical waveguide the study of electromagnetic waves is necessary. In the interests of simplification, we start with planar (slab) waveguides which confine the light in one-dimension. The optical ray model enables an easy way to describe the propagation of guided waves in a medium without handling the Maxwell equations [34]. The model involves Snell's Law (1) to explain the behavior of propagating waves in a medium with the RI n_1 between two regions with the RI n_2 . The incident field to these interfaces will be partly transmitted and partly reflected. The relationship between the RIs and the angles of incidence θ_1 and refraction θ_2 are defined as:

$$n_1 \sin \theta_1 = n_2 \sin \theta_2 \quad (1)$$

Moreover, the refractive index difference Δn (2) is mostly used to express the relative difference in refractive index of the core (n_1) and cladding (n_2) and to describe the light guidance of the structure. For example, planar waveguides with a very low index contrast ($\Delta n \ll 1$) are weakly guided mediums [34].

$$\Delta n = \frac{n_1 - n_2}{n_1} \quad (2)$$

In Figure 1, the RI of layer 1 is higher than the RI of the two other surrounding layers (2).

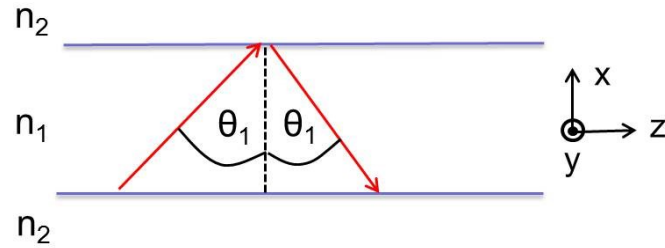


Figure 1: TIR at two interfaces demonstrating the concept of a slab waveguide

It can be demonstrated by Snell's Law (3) that for angles of incident greater than a critical angle θ_c , no light will be transmitted into the surrounded media and total internal reflection (TIR) occurs.

$$\sin \theta_c = \frac{n_2}{n_1} \quad (3)$$

This concept clearly shows how the light is confined by TIR and propagates along the z-direction. Now, two waveguide types must be differentiate: a waveguide is said to be symmetrical if the same boundary conditions will apply at the upper and lower interfaces, and in the case of two different layers, e.g. the substrate is made of Si (n_2) and the upper layers is air (n_3), the waveguide is called asymmetrical.

However, the propagating electromagnetic waves in a waveguide can be analyzed by Maxwell's equations [34]. The solutions are known as modes, which are eigenfunctions of the equation system. A waveguide mode is a field pattern whose amplitude and polarization profiles remain constant along the longitudinal direction of propagation and depends on the operating wavelength, geometry and material composition of the waveguide. There are two types of modes: longitudinal modes (parallel to the wave vector \vec{k}) or standing waves which transport no energy and transverse modes (perpendicular to \vec{k}). Transverse electromagnetic modes (TEM) have neither electric nor magnetic field in the direction of propagation (z). In a metallic or dielectric waveguide, TEM waves cannot propagate, since the Maxwell's equations don't allow a non-zero electric field at the boundaries, exceptions are two-conductor transmission lines such as coaxial cables [34, 35]. Therefore, only transverse electric (TE) and transverse magnetic (TM) modes are possible. These two polarizations differ by the non-zero field component in the z-direction. As depicted in Figure 2, in TE modes or H modes the electric field (E field) is parallel to the interface. Correspondingly, TM modes have only a non-zero E field component perpendicular to the interface, thus they named E modes [34, 35].

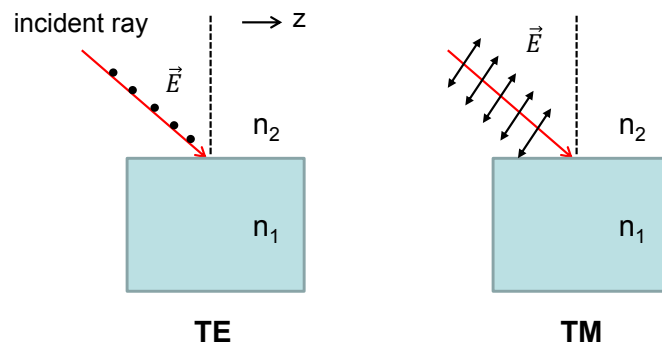


Figure 2: Wave representation of TE and TM modes in a planar waveguide

Furthermore, by the historic Fresnel's formulas the description of reflected and transmitted light at uniform planar interfaces is possible. The reflection coefficients r_{TE} (4) and r_{TM} (5) for the TE and TM polarization are usually written as follows [35]:

$$r_{TE} = \frac{n_1 \cos \theta_1 - n_2 \cos \theta_2}{n_1 \cos \theta_1 + n_2 \cos \theta_2} \quad (4)$$

$$r_{TM} = \frac{n_2 \cos \theta_1 - n_1 \cos \theta_2}{n_2 \cos \theta_1 + n_1 \cos \theta_2} \quad (5)$$

Using Snell's law (1), and incident angles greater than θ_c and an imposed phase shift ϕ of the reflected wave denoted by (6) and (7), (4) and (5) can be transformed into (8) and (9) [35].

$$r = e^{i\phi} \quad (6)$$

$$\phi = kz \pm \omega t \quad (7)$$

$$\phi_{TE} = 2 \tan^{-1} \frac{\sqrt{\sin^2 \theta_1 - \left(\frac{n_2}{n_1}\right)^2}}{\cos \theta_1} \quad (8)$$

$$\phi_{TM} = 2 \tan^{-1} \frac{\sqrt{\frac{n_1^2}{n_2^2} \sin^2 \theta_1 - 1}}{\frac{n_2}{n_1} \cos \theta_1} \quad (9)$$

Additionally, the phase of a wave varies with time (t) and distance (z) and can be quantified by the time and spatial derivation (10), (11) [35],

$$\left| \frac{\partial \phi}{\partial t} \right| = \omega = 2\pi f \quad (10)$$

$$\frac{\partial \phi}{\partial z} = k = \frac{2\pi}{\lambda} \quad (11)$$

where k is the wavevector or propagation constant of the wavefront and related to the wavelength λ in the medium. In free space k is usually named to k_0 , whereby k and k_0 are related by the refractive index n of the medium (12) and λ_0 the wavelength in free space [35]:

$$k = nk_0 = n \frac{2\pi}{\lambda_0} \quad (12)$$

Now, light is propagating in z-direction through a planar waveguide based on a core material with the RI n_1 , a height h , a lower cladding n_2 and an upper cladding n_3 . The wavevectors in z (named as propagation constant β) and y-direction are given by (13), (14).

$$k_z = \beta = n_1 k_0 \sin \theta_1 = [\text{rad}/m] \quad (13)$$

$$k_y = n_1 k_0 \cos \theta_1 \quad (14)$$

Theoretically, a standing wave is formed by reflection at each interface across the waveguide in x-direction. The total phase shift ϕ_t after one "round trip" is introduced of

$$\phi_t = 2n_1 k_0 h \cos \theta_1 - \phi_u - \phi_l = 2m\pi. \quad (15)$$

ϕ_u and ϕ_l are referred as the phase shift at the upper and lower cladding. Corresponding to the integer m and each polarization there will be a series of discrete angles θ_1 , for which (15) can be solved and light will propagate. Therefore, discrete transvers field patterns (modes) will be formed in the x- and y-direction with associated propagating constants k_z (β) and k_y . These constants describe with which velocity the wave propagates in z- and y-direction. Additionally, we can define in equation (17) an ERI n_{eff} for each mode which is equivalent to the mode propagation along the z-direction without reflecting at the interfaces of the waveguide.

$$n_{\text{eff}}^m = n_1 \sin \theta_1 = \frac{\lambda}{2\pi} \beta^m \quad (16)$$

The modes of propagation are identified by naming of the polarization and the value of the integer m . When m is even, the mode is symmetric, when m is odd, the mode is anti-symmetric. The first TE or fundamental mode is described as TE_0 . In addition, the dispersion relations for both polarizations in a symmetrical ($\phi_u = \phi_l$) and an asymmetrical waveguide are given in the following formulas [35]. It can be shown that, with $n_2 < n_{\text{eff}} < n_1$. A comparison of the critical angles or the ERIs for each polarization will show which mode has a stronger confinement inside of the core.

$$TE_{\text{sym}}: \tan\left(\frac{n_1 k_0 h \cos \theta_1 - m\pi}{2}\right) = \frac{\sqrt{\sin^2 \theta_1 - \left(\frac{n_2}{n_1}\right)^2}}{\cos \theta_1} \quad (17)$$

$$TM_{\text{sym}}: \tan\left(\frac{n_1 k_0 h \cos \theta_1 - m\pi}{2}\right) = \frac{\sqrt{\left(\frac{n_1}{n_2}\right)^2 \sin^2 \theta_1 - 1}}{\left(\frac{n_2}{n_1}\right) \cos \theta_1} \quad (18)$$

$$TE_{\text{asym}}: n_1 k_0 h \cos \theta_1 - m\pi = \tan^{-1}\left(\frac{\sqrt{\sin^2 \theta_1 - \left(\frac{n_2}{n_1}\right)^2}}{\cos \theta_1}\right) + \tan^{-1}\left(\frac{\sqrt{\sin^2 \theta_1 - \left(\frac{n_3}{n_1}\right)^2}}{\cos \theta_1}\right) \quad (19)$$

$$TM_{\text{asym}}: n_1 k_0 h \cos \theta_1 - m\pi = \tan^{-1}\left(\frac{\sqrt{\left(\frac{n_1}{n_2}\right)^2 \sin^2 \theta_1 - 1}}{\left(\frac{n_2}{n_1}\right) \cos \theta_1}\right) + \tan^{-1}\left(\frac{\sqrt{\left(\frac{n_1}{n_3}\right)^2 \sin^2 \theta_1 - 1}}{\left(\frac{n_3}{n_1}\right) \cos \theta_1}\right) \quad (20)$$

Furthermore, there is a limit of number of modes due to θ_1 which can propagate in the waveguide or in other words there is a critical height h_{max} to design a SM waveguide for a given wavelength λ . This can be obtained for both polarizations by enforcing $m = 0$ in (17)-(20). In principle, the core should be thin enough such that the second order mode ($m = 1$) is cut-off. Additionally, the operating wavelength determines a maximum number of possible modes. For example, in an asymmetrical waveguide h_{max} for both polarizations is defined as [37]:

$$h_{max}(TE) = \frac{\tan^{-1} \left(\frac{\sqrt{\sin^2 \theta_1 - \left(\frac{n_3}{n_1}\right)^2}}{\cos \theta_1} \right)}{n_1 k_0 \cos \theta_1} \quad (21)$$

$$h_{max}(TM) = \frac{\tan^{-1} \left(\frac{\sqrt{\left(\frac{n_1}{n_3}\right)^2 \sin^2 \theta_1 - 1}}{\left(\frac{n_3}{n_1}\right) \cos \theta_1} \right)}{n_1 k_0 \cos \theta_1} \quad (22)$$

In particular, the mode properties of a waveguide are characterized in terms of dimensionless normalized waveguide parameters. For example, in a step-index planar waveguide, where the RI profile is characterized by a sharp decrease at both cladding interfaces, the normalized frequency, also known as the V number is defined as:

$$V = \frac{2\pi}{\lambda} h \sqrt{n_1^2 - n_2^2} \quad (23)$$

$$NA = \frac{1}{n_0} \sqrt{n_1^2 - n_2^2} \quad (24)$$

In formula (24)) the numerical aperture (**NA**) of the waveguide is given which determines a maximum angle of the incident ray so that the transmitted beam is guided in the core where n_0 is the RI of the medium around the waveguide. A high **NA** usually relates to a large beam divergence for the fundamental mode exiting the waveguide end, but this beam divergence also depends on the core diameter. Additionally, such a waveguide is strongly guiding and supports a large number of modes, thus a smaller core is required for SM guidance. Especially, bend losses are reduced for high bend radii [38].

However, the propagation constant β can be expressed by the normalized guide index b , as it is shown in formula (25).

$$b = \frac{n_{eff}^2 - n_2^2}{n_1^2 - n_2^2} \quad (25)$$

Furthermore, V and b have the same definition in both waveguide types, but an additional asymmetric parameter δ is needed in the case of an asymmetrical waveguide, as seen below.

$$\delta = \frac{n_2^2 - n_3^2}{n_1^2 - n_2^2} \quad (26)$$

Thus, we can use formula (25) and (26) to express the normalized dispersion relations for the TE and TM modes in an asymmetrical waveguide [39], as shown in (27) and (28).

$$TE_m: V\sqrt{1-b} = m\pi + \tan^{-1} \sqrt{\frac{b}{1-b}} + \tan^{-1} \sqrt{\frac{b+\delta}{1-b}} \quad (27)$$

$$TM_m: V\sqrt{1-b} = m\pi + \tan^{-1} \left(\frac{n_1}{n_2} \sqrt{\frac{b}{1-b}} \right) + \tan^{-1} \left(\frac{n_1}{n_3} \sqrt{\frac{b+\delta}{1-b}} \right) \quad (28)$$

Moreover, TE_m and TM_m modes have characteristic cut-off frequencies V_m^c below which waves cannot propagate through the waveguide core and the normalized guide index b (25) is equal to zero. In contrast, it is important to note that the fundamental mode TE_0 in a symmetrical waveguide will never be cut-off, because the dispersion relations for TE and TM polarizations allow a solution when $m = 0$ [35]. Moreover, symmetric weakly guiding waveguides ($\Delta n \ll 1$) show equal propagation constants of the TE_m and TM_m modes whereby the cut-off values are still the same, thus they are not polarization dependent but named degenerate. The waves are travelling with the same phase velocity and cannot be distinguishing (V - b curves merge), their mode patterns are not seen distinctly and forming a superimposed field distribution. In contrast, integrated optic circuits often use asymmetric strongly guiding waveguides where the RI of the core media widely varies from the RIs of the claddings resulting in high light confinement [34]. The disadvantage appears from different propagation constants leading to polarization dependence, modal dispersion as well as propagation losses, detailed explained in chapter 2.4. Furthermore, an increased core height leads to higher propagation constants, creates similar TE/TM mode profiles in y - and z -direction and reduces the polarization dependence.

Anyhow, the definition for characteristic cut-off frequencies V_m^c in an asymmetrical waveguide for both polarizations is given in (29) and (30). These formulas are also useful for the design of a SM waveguide by choosing $m = 1$.

$$TE_m: V_m^c = m\pi + \tan^{-1}(\sqrt{\delta}) \quad (29)$$

$$TM_m: V_m^c = m\pi + \tan^{-1} \left(\frac{n_1}{n_3} \sqrt{\delta} \right) \quad (30)$$

However, propagation angles leading to TIR generate solutions which consist of an incident, a reflected and a transmitted wave to obey Maxwell's equations. Thus, the transmitted wave must be a not-traveling wave with an exponentially decay refereed as evanescent wave [40]. The trend of the amplitude of the evanescent wave of every mode m can be described by a characteristic penetration depth σ (31) into the cladding layer whereas the field amplitude is equal to $1/e$ in relation to the direction of propagation [40].

$$\sigma^m = \frac{\lambda}{2\pi\sqrt{n_1^2 \sin^2 \theta^m - n_2^2}} \quad (31)$$

Additionally, unbounded modes, referred as radiation modes, exist below the cut-off frequency. They are indiscrete solutions of Maxwell's equation and arise in the cladding when the field oscillates faster than exponentially decaying [41]. The modes radiate power which flows out of the guide during propagation. Moreover, in waveguides also appear cladding modes, which are

guided by TIR at the cladding/air interface and are trapped in the cladding. Both mode types can lead to mode coupling with higher-order modes of the core, resulting in increased loss of the core power. Such leaky modes will be discussed further in this work in chapter 2.4.

Furthermore, the propagation angle of the light determines the order of the mode, meaning that steeper angles lead to high-order modes which penetrate deeper into the upper and lower cladding in comparisons to low-order modes of the waveguide. In low-order modes, the electric and magnetic fields are concentrated near the core and are smaller in penetration depth. High-order modes show angles near the critical angle causes a slow decay of the evanescent field and a deeply wave penetration into the claddings. Especially, weakly guiding waveguides show higher penetration depths compared to strongly guiding waveguides ($\Delta n \gg 0$). By increasing the RI contrast, the confinement can be improved, but this also means that the waveguide core should be reduced in size to keep the waveguide single mode. Then, however, the geometrical features not only become very small but have to be very accurately fabricated [42]. Generally, mostly biochemical sensors are based on weakly guiding waveguides where the evanescent field of the mode interacts with the medium being tested, e.g. [11, 12, 13].

Additionally, this parameter is used for the definition of the mode field diameter $2\omega_0$ (MFD) of a mode. For many applications, the guided mode(s) should have a spatial extent small as possible. If the guided fields are narrow, the devices can be packed denser on the optical chips. However, we can quantify the MFD as being the core height h plus the $1/e$ distance on either side as shown in formula (32) [41].

$$2\omega_0 = h + 2\sigma \quad (32)$$

If the core height is in the order of λ or smaller, there is a rapid increase of the MFD, because the portion of the field in the core is subject to the condition of the diffraction limit [41], i.e.

$$2\omega_0 > \frac{\lambda}{2n_1}. \quad (33)$$

Secondly, as the core height decreases the spatial extent of the mode decreases until a limit above the mode expands rapid and the waveguide becomes weaker with increasing confinement loss within the core [41].

2.2.2 Channel Waveguides and Bends

Recall, one-dimensional (planar) waveguides support two types of transversal electromagnetic modes (TEM) - either TE_m or TM_m modes by confining the light in one dimension and if the light propagates a long a given direction (z axis) the light spread out in the perpendicular direction. Channel or rectangular waveguides allow TIR not only across the core thickness but also at the lateral boundaries. In addition, many waveguide types show larger lateral dimensions than transversal and the vertical index contrast often is very low. In that case, the modes of two-dimensional waveguides are called hybrid modes, i.e. all E and H field components exist. Fortunately, the TEM modes are strongly polarized along the x - or y -direction due to the RI and therefore an approximation can be made according to the major component of the E field [34].

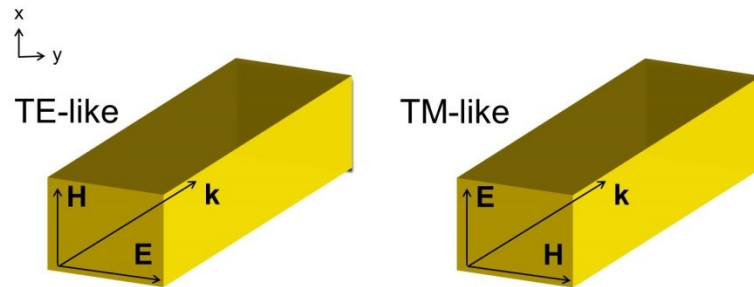


Figure 3: Wave representation of TE- and TM-like modes in a channel waveguide

As illustrated in Figure 3, the TE-like modes having the main E field component (but not only) along the x axis and behave very similar to the TE modes in a planar optical waveguide (E_{mn}^x / TE_{mn} / HE_{mn}). Accordingly, quasi-TM or TM-like modes are referred to as E_{mn}^y or TM_{mn} (EH_{mn}) modes, have E^y as the major component of the E field (but not only) and are closely related to the TM mode in a slab waveguide [43, 44]. Therefore, whereas the numerical solutions for slab waveguides were exact, there is no equivalent procedure (except through limiting boundary conditions) to exactly solve the eigenvalue equations of even the simplest channel waveguides [41]. The mixing of polarization increases as the aspect ratio becomes symmetric, thus the strength of waveguiding enhances. Thus, the most common techniques for solving the eigenvalue equations and illustrating the mode intensity profiles and field distribution are computational methods like the finite difference method (FDM), the finite element method (FEM) and the effective index method (EIM) for finding ERIs, whereas the latter are used in this work and explained in detail in chapter 3.

However, a few channel waveguides are based on rectangular cross-sections. Several geometries are shown in Figure 4, where the light guiding layer is in yellow marked.

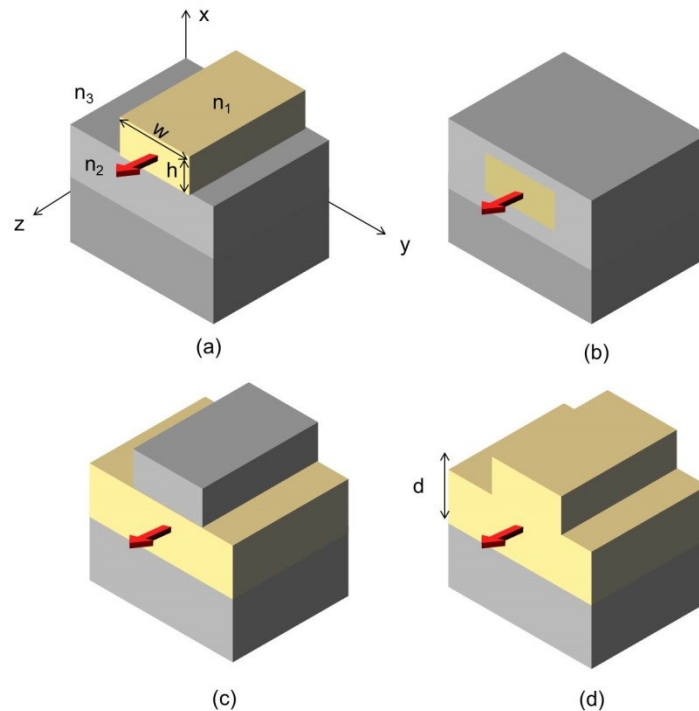


Figure 4: Representative channel waveguides (a) Strip waveguide, (b) Buried channel waveguide, (c) Strip-loaded waveguide, (d) Rib waveguide [34]

Rib waveguides (Figure 4 (d)) are comparable with strip waveguides except that the strip is made by etching away the core material outside of the core region. Their light confinement is less strong as in strip waveguides, like shown in Figure 4 (a). One advantage is that the mode doesn't interact much with the boundaries, thus the propagation loss is decreased by less light scattering [41]. Conversely, strip waveguides are similar to buried-channel structures (Figure 4 (b)), but with a lower upper cladding (usually air). This geometry allows small cores and tight bending radii with a very strong light confinement. The core size for a SM structure at 1.3 - 1.55 μm telecommunication wavelength can be a few hundred nanometers according to the core material [34]. This waveguide geometry offers the possibility to realize ultra-dense photonic devices, which can further decrease the cost of silicon photonics and is a strong argument for the usage in this work. However, the silicon microphotonic application, e.g. a biosensor, determines the material and geometry of the used waveguide.

Anyhow, in chapter 2.2.1 it was already mentioned that any given time-harmonic electromagnetic wave with the angular frequency ω propagating through a medium (μ , ϵ) must satisfy the source-free Maxwell's equations given by [45]

$$\vec{\nabla} \times \vec{E} = -i\omega\mu\vec{H}, \quad (34)$$

$$\vec{\nabla} \times \vec{H} = i\omega\epsilon\vec{E}. \quad (35)$$

Formula (34) and (35) can be manipulated into wave equations for the electric and magnetic fields, e.g.

$$\vec{\nabla}^2 \vec{E} + (k^2 n^2 - \beta^2) \vec{E} = 0, \quad (36)$$

$$\vec{\nabla}^2 \vec{H} + (k^2 n^2 - \beta^2) \vec{H} = 0. \quad (37)$$

These both equations are referred as Helmholtz equations, where the wavenumber k in formula (38) is real-valued for lossless media and complex-valued for lossy media.

$$k = \omega\sqrt{\mu\epsilon}. \quad (38)$$

The solutions in (39) and (40) of the Helmholtz equations take the form of plane waves propagating in +z-direction through an arbitrary medium with the propagation constant β and are characterized by a z-dependence of $e^{-\gamma z}$ [45].

$$\vec{E} = \vec{E} \exp i(\omega t - \vec{k}\vec{r}) = \vec{E} \exp i(\omega t - \beta z), \quad (39)$$

$$\vec{H} = \vec{H} \exp i(\omega t - \vec{k}\vec{r}) = \vec{H} \exp i(\omega t - \beta z). \quad (40)$$

Additionally, β may be written in terms of the wave attenuation constant α and the phase constants γ as

$$\beta = \alpha + i\gamma. \quad (41)$$

The sign conventions for α and γ are taken so that both are positive for a wave propagating in +z-direction. The propagation constant has a zero real part ($\alpha = 0$, $\beta = i\gamma$) when the wave

travels without attenuation (no losses) or is complex-valued when losses are present [45]. Insofar the effective refractive index n_{eff} can be expressed by

$$n_{\text{eff}} = \beta + i\delta_z \quad (42)$$

whereas δ_z corresponds to the damping along the propagation direction [45].

Another possible evaluation of the quality of the light guidance and energy centering in the waveguide core is the estimation of the mode confinement factor Γ^{mode} . A guided mode is defined as the fraction of its energy in the core region. Γ^{TE} can be either larger or smaller than Γ^{TM} , but the difference between them is small [46]. Furthermore, for modes of the same polarization a low-order mode is more confined than a high-order mode, which is similar to the dependence of the penetration depth [46]. Especially, the SM guidance of the dominant TE or TM mode is important in many photonic applications. Thus, the following approximate formula can be used to estimate the confinement factor Γ^{mode} of a mode in an asymmetric waveguide [46]:

$$\Gamma^{\text{TE}} = \frac{V_x * V_y}{2 + V_x * V_y} = \frac{h * w * \left(\frac{2\pi}{\lambda}\right)^2 \sqrt{(n_1^2 - n_2^2)} * \sqrt{(n_{\text{eff}}^2 - n_3^2)}}{2 + h * w * \left(\frac{2\pi}{\lambda}\right)^2 \sqrt{(n_1^2 - n_2^2)} * \sqrt{(n_{\text{eff}}^2 - n_3^2)}} \quad (43)$$

The effective mode confinement factor Γ^{mode} is defined as its fractional power in the $h \times w$ two-dimensional guiding core and can be found by multiplying its two normalized frequency factors in the x- and y-direction [46]. Γ^{mode} ranges between 0 and 1, whereby for the TM mode a similar term can be derived taking into account the ERI (n_{eff}) of the mode.

However, a more detailed analysis of the guided modes in a rectangular waveguide can be performed by using FEM. Here, the waveguide cross-section plays a crucial role in determining light confinement as a strip waveguide in practices. Figure 5 shows calculated mode patterns or field distributions of the first quasi-TE and quasi-TM modes of a waveguide.

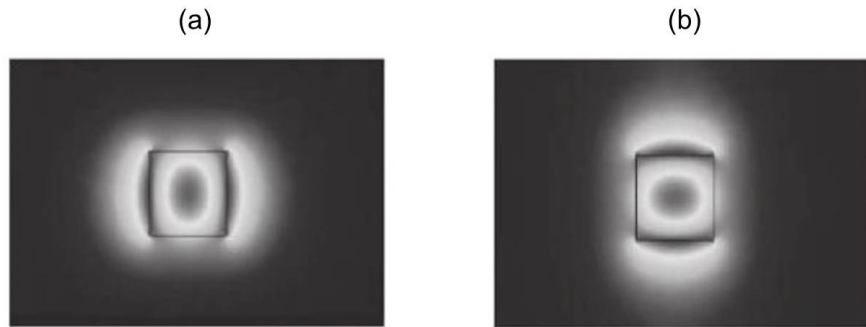


Figure 5: Field profiles for the fundamental TE-like (a) and TM-like (b) modes in a rectangular waveguide [34, 47]

The field pattern is formed by the superposition of two plane waves travelling in different directions which give a standing wave pattern in x- and y-directions. The TE field profile (a) is characterized by higher field intensity at the side walls, whilst the TM mode (b) has relatively small amplitude at the side walls, but much higher amplitude at the top and bottom interfaces [34]. Additionally, Figure 5 (b) shows a large localized field distribution near the waveguide surface and also Reed [34] found that shrinking waveguides to small dimensions opens the application area of evanescent field biosensors.

However, various types of fabrication techniques, e.g. lithography and etching, are involved in the manufacturing of the whole Si-based photonic circuit. The front and side wall roughness is the most important property of the waveguide related to the light in- and out coupling and the light transmission [48, 49, 50]. This parameter is mostly increased by the imperfection of the lithography and etching process. Therefore the latter are the key technologies in achieving smoothly etched designs [34]. More often, though, deviations from the rectangular shape, e.g. trapezoidal waveguides [51, 52], occur during the fabrication. In addition, the precise thickness of the lower cladding [53], e.g. Silicon dioxide (SiO_2) layer as shown in Figure 4 (a, b), is significant, regarding to the penetration depth of the optical field into the Si substrate. These points are dealt in more detail with in chapter 4 and chapter 5.

However, all waveguides discussed so far in chapter 2.2 have been depicted as simple straight two-dimensional structures in the z-direction. More particular, light guiding to various parts of the photonic circuit requires bending of the waveguide into different directions. A curved waveguide allows a gradual transition from one direction to another that can have negligible losses [35]. Figure 6 shows a waveguide bend with a distorted lateral mode shape connected to a straight waveguide.

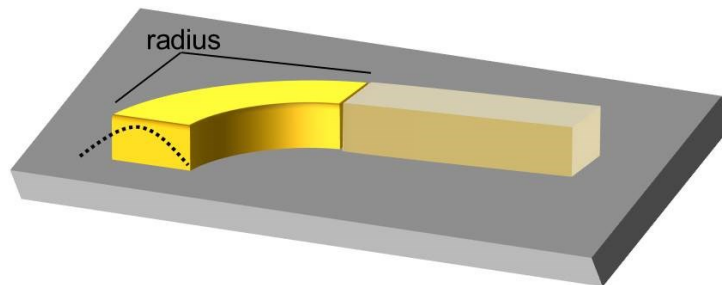


Figure 6 [35]: Waveguide 90° - bend with a distorted lateral mode shape and a connected straight waveguide

The light at the outer left cladding with the longer arc bend propagates more quickly than light at the inner cladding to maintain the phase relationship across the mode. There is no way for the light in the cladding to extend the velocity up to unguided light in the same material to maintain the mode. The mode bounces along the core-cladding interface and will eventually hit the interface at an angle that does not result in TIR. Thus, the light will be radiated and lost from the mode resulting in a distorted mode shape [35]. Additionally, the mode mismatch between the straight part of the bended waveguide and the curvature is a result of the mode shift slightly to the outside of the bend [54]. The already mentioned strip waveguides show here potential for improvement through their large Δn , thus they can tolerate tighter bends [35], because they allow a bigger range of possible TIR angles. Nevertheless, there is a significant drawback: Scattering losses are much higher in these structures [54]. However, in a mathematical view, the bending loss is a highly nonlinear function of the bend radius. The bending loss α_B of a decreased bend radius is low up a critical radius R_c [45], e.g.

$$\alpha_B = C e^{R/R_c} \quad (44)$$

where C is a constant. R_c depends strongly on Δn as well as on the core height. For weakly guiding waveguides it can be in the order of several millimeters, while for strongly guiding structures, e.g. strip waveguides, it can be a few tens of microns [45]. For the most theoretical studies, numerical techniques, e.g. beam propagation method (BPM), are used instead of difficult approximated techniques, but quite often it is difficult to take advantage from such methods for the design of the bend [55]. In this work, two-dimensional FEM simulations and scattering parameter estimations for different operation frequencies of low-order modes for different bend radii of the waveguide were carried out.

2.2.3 Photonic Crystal Structures

Photonic crystals (PhCs) are regular arrays of materials (A,B) with different RIs and can be seen as optical semiconductors for photons with a photonic band gap, wherein no electromagnetic eigenmodes exist, as similar to the electronic band structure of ordinary semiconductors [56]. Figure 7 shows the schematic illustration of one-dimensional (1D), two-dimensional (2D) and three-dimensional (3D) PhCs.

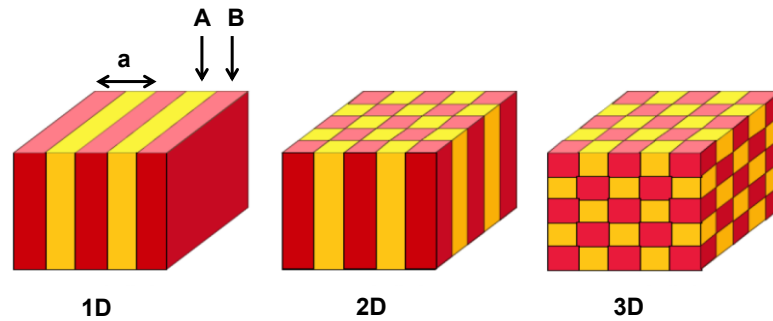


Figure 7 [56]: Photonic crystal structures of different dimensions are based on two dielectrics with low RI (A) and high RI (B), whereby a is the lattice constant

If the lattice constant a , the spatial period of the layer stack, is in the order of the half wavelength of the electromagnetic wave, the PhC will maximal reflect the light. These forbidden frequencies or wavelengths lie in the photonic band gap and cannot propagate through the crystal [57]. However, this work focuses on theoretically and experimental results of one- and two-dimensional PhCs as depicted in Figure 7. A one-dimensional PhC, named “Bragg stack” (Figure 8 (a)), simply bases on two periodically repeated dielectric layers with different RIs (A, B) that are repeated by a lattice constant a . The wave propagation is comparable to the charge-carrier transport inside a semiconductor, where the periodic potential of the atoms has a similar effect as the periodically variation of the RI in the shown PhC. The dispersion relations (band diagrams), frequency ω versus wavenumber k , of a uniform dielectric and a Bragg stack are illustrated in Figure 8 (b).

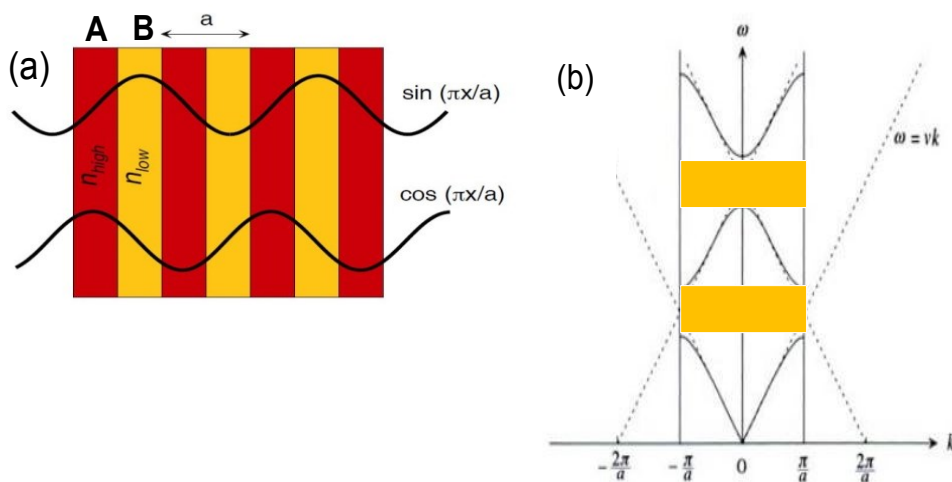


Figure 8 [58, 56]: (a) One-dimensional PhC with an RI periodicity a , Band diagram of a uniform dielectric (dashed lines) and a Bragg stack (solid lines) in the first Brillouin zone, band gap (yellow bars) appears by the folding of two “dashed” dispersion lines

When an electromagnetic wave enters the PhC, some of it reflects at the interfaces, some is transmitted by Bragg diffraction [56]. If the waves are out of phase they will cancel out each other by destructive interference. Thus, the total wave will not be reflected back and is propagating through the layer stack only slightly attenuated. This means, that the dielectric periodicity of the RI in a Bragg stack splits the degenerated plane waves of a uniform medium into $\cos(\pi x/a)$ and $\sin(\pi x/a)$ standing waves by forming the lower and upper edges of the photonic band gap (Figure 8 (b)) [58]. The former has E field peaks in the higher dielectric material (n_{high}) and so will lie at a lower frequency than the latter. Moreover, for a wavelength inside the band gap ($\lambda \sim 2a$) the scattered waves are in phase and will exactly constructively interfere. The light will be reflected back and the total standing wave is attenuated, e.g. a mirror reflects selected wavelengths. This means, that a complete photonic band gap is a frequency or wavelength range in which there are no propagating solutions of the Maxwell's equations ((34), (35)) for any wavevector \mathbf{k} , surrounded by allowed states above and below the gap [58]. However, for a two-dimensional PhC exists, corresponding to the polarization, two basic topologies which are illustrated in Figure 9 (a, c): high RI rods surrounded by a low RI material (Air) or low RI holes (Air) etched in a high RI material [58]. The PhC forces in-plane light confinement, whereas guiding in the third dimension is due to TIR in the high RI material. The crystal responds differently to the TE and TM polarization, where TE is the polarization with the E field component in the plane and around the holes/rods, and TM polarization with the E field component parallel to the rods/holes [58]. In Figure 9 (b, d), the frequencies are plotted around the boundary of the first Brillouin zone. That means that a PhC with a TM band gap (Figure 9 (b)) will filter out this polarization, while allowing the TE polarization to pass through. Moreover, Maxwell's equations ((34), (35)) are scale-invariant, thus the frequency ω is given in units of $2\pi c/a$, whereby the same solutions can be applied to any frequency simply by choosing the used lattice constant a [58].

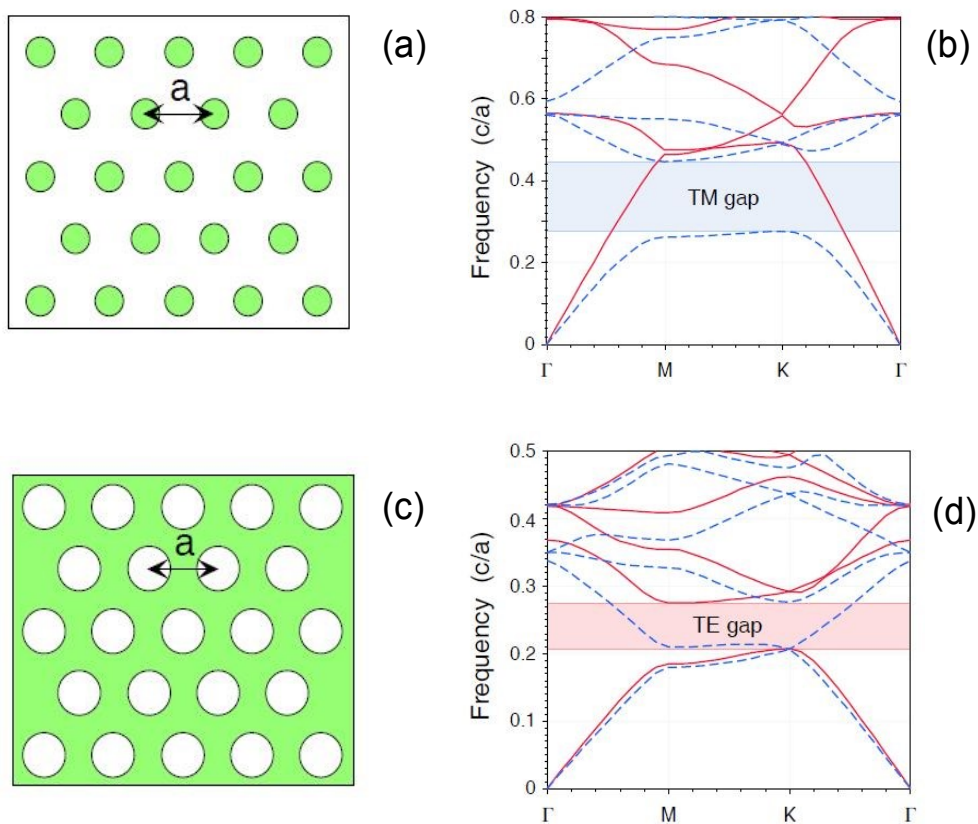


Figure 9 [58]: Two-dimensional PhCs based on a hexagonal lattice, dielectric rods in air (a), and air holes etched into a dielectric (c), calculated band diagrams (b, d) and photonic band gaps (bars)

Nevertheless, calculations of the complete band gap of two-dimensional PhCs are significantly difficult considering all crystal directions and polarizations. The key elements which must be taken into account are the geometrical arrangement, the RI contrast of the materials and the volume-ratio of the high and low RI materials [56]. However, various theoretical and experimental techniques have been developed since Yablonovitch [59] and John [60] discovered the first one-dimensional PhCs in 1987. As already mentioned two-dimensional PhCs show polarization sensitivity and allow an actively changing of the optical parameters which open a broad application spectrum for integrated Si-based photonic circuits. The high localization level of PhC structures enables compact, high efficient photonic devices like filters [61], beam splitter [62], waveguides with extreme small bending radii [63] and optical resonators [64].

Furthermore, most of the mentioned applications are based on the possibility to extend the optical properties of a PhC by a specific disturbance of the lattice periodicity, referred to as defects. Depending on the dimensionality they are considered as point defects (micro resonators/cavities) and line defects (photonic/defect waveguides) [65]. Especially, the coupling between micro resonators and defect waveguides allow the development of new devices and integrated photonic circuits [66]. The great benefit of these modified PhC is that light can propagate around the defects with a frequency (or wavelength) inside of the band gap [56, 67]. In one dimension, light can be confined in a single defect plane, e.g. in a Bragg stack with an extra dielectric layer with a different RI. In a two-dimensional PhC, light can be localized by a point line or a line defect, e.g. by removing dielectric material, as illustrated in Figure 10 (a, b).

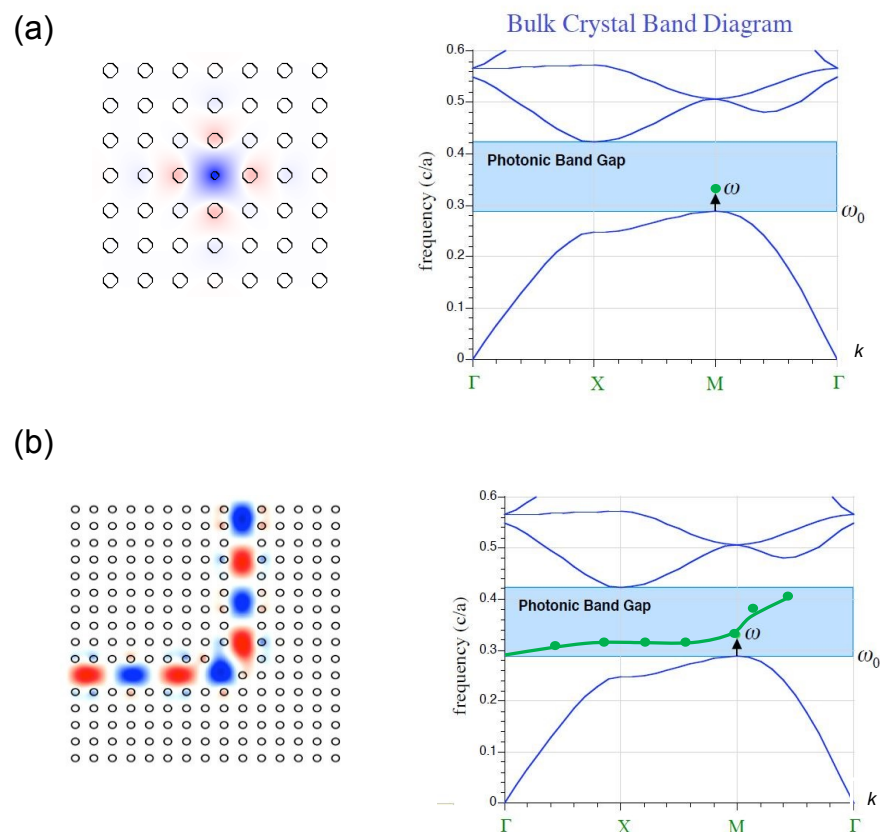


Figure 10 [66]: Band diagram of the bulk PhC with a point defect (a) and 90° bended line defect (b), Bulk crystal band diagrams; shown mode profiles are marked with an arrow at the certain frequency

The point defect (a) is working like a cavity with perfectly reflecting walls. The light with a certain frequency within the band gap winds up the defect and cannot leave, because the crystal does not allow states at that frequency [65]. A line defect (b) can be seen as a linear array of point defects which creates a defect band with frequencies in the photonic band gap and extend along the defect, but decay exponentially into the rest of the crystal [65]. Moreover, lossless sharp bends of defect waveguides enable flexible and high power transmission between all devices on the photonic circuit. Light back scattering inside of the bended line defects or scattering into the bulk crystal is forbidden by Bloch's theorem [66] and the band gap. Thus, reflection allows that the light can be steered around the corner. However, any discontinuity will ruin the discrete translational symmetry of the lattice and can push down or pull up a single frequency or a frequency band (defect bend) from the continuum above or below the gap into the gap itself [65].

2.3 COUPLING TO THE OPTICAL CIRCUIT

Optical light coupling of optical fibers, light sources and detectors to an integrated photonic circuit and light coupling between various photonic components as waveguides of different cross-section in the micrometer range on the circuit, is conceptually trivial. Requirements for the optical coupling techniques are low cost, high coupling efficiencies, mode selectivity and scalability to high volume production rates [68, 69]. There exist a variety of possible techniques for performing the coupling task, the most common are [34, 35, 69]: end-fire coupling, butt-coupling, prism coupling, grating coupling and taper coupling. Especially, the connection between photonic structures of different geometry by laterally or vertically tapered waveguides improves the gradual transition of the light and the coupling situation also to external fibers. The tapered section can act as a mode size converter that transforms the input mode shape of the fundamental mode, because the standard SM fibers are very large in size compared to Si-based SM waveguides [34]. However, each of the mentioned coupling methods has a set of advantages and disadvantages. The trick is to find the best solution for the respective application. In the chapters below the basic coupling techniques will be shortly discussed, with a focus on end-fire, butt- and taper-coupling which have been used in this work. An overview of the principles of all coupling techniques is shown schematically in Figure 11.

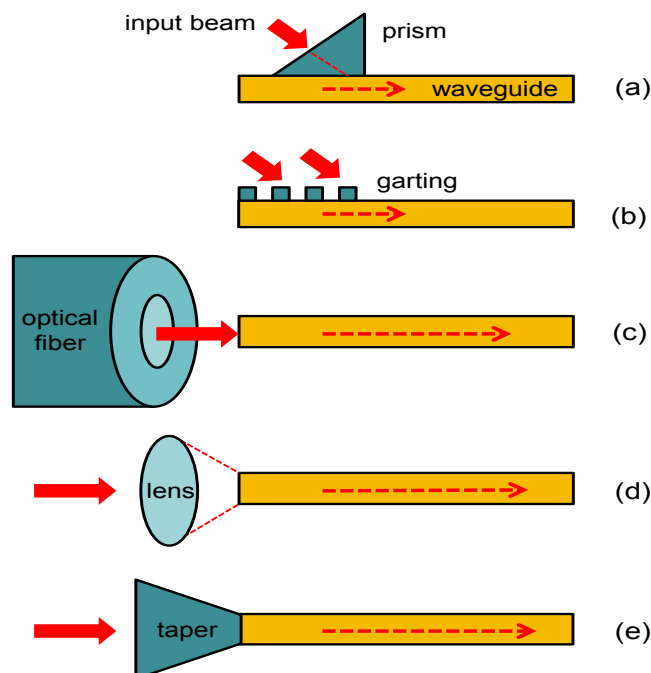


Figure 11 [69]: Coupling techniques – prism coupling (a), grating coupling (b), butt-coupling (c), end-fire coupling (d), taper coupling (e)

Moreover, the output coupling from the integrated circuit or photonic structure to a detector is also an important aspect which usually performed with equipment which had already been used for the input coupling of the beam. Generally, the transmission of the guided modes at the endface of the waveguide/fiber depends on the acceptance angle ($2\theta_a$) of the waveguide/fiber, which is defined by the numerical aperture (NA, (24)). Anyhow, loss mechanisms as scattering or mode conversion, which will be discussed in the following chapter 2.4, can decrease or increase the confined energy in the core and cause in a smaller or greater effective aperture angle ϵ' . Fundamentally, the output angle radiation characteristic (NA_{out}) of a straight waveguide is determined by the input aperture (NA_{in}), unless NA_{in} is less than $NA_{waveguide}$ [70]. For example, an asymmetric input coupling situation of the beam leads to a symmetric output coupling distribution (Figure 12 (b)) [70]. It is also possible that mode conversion results in a partly "refilled" NA of the output field distribution (Figure 12 (c)). However, an overview of the radiation aperture of different coupling situations is illustrated in Figure 12.

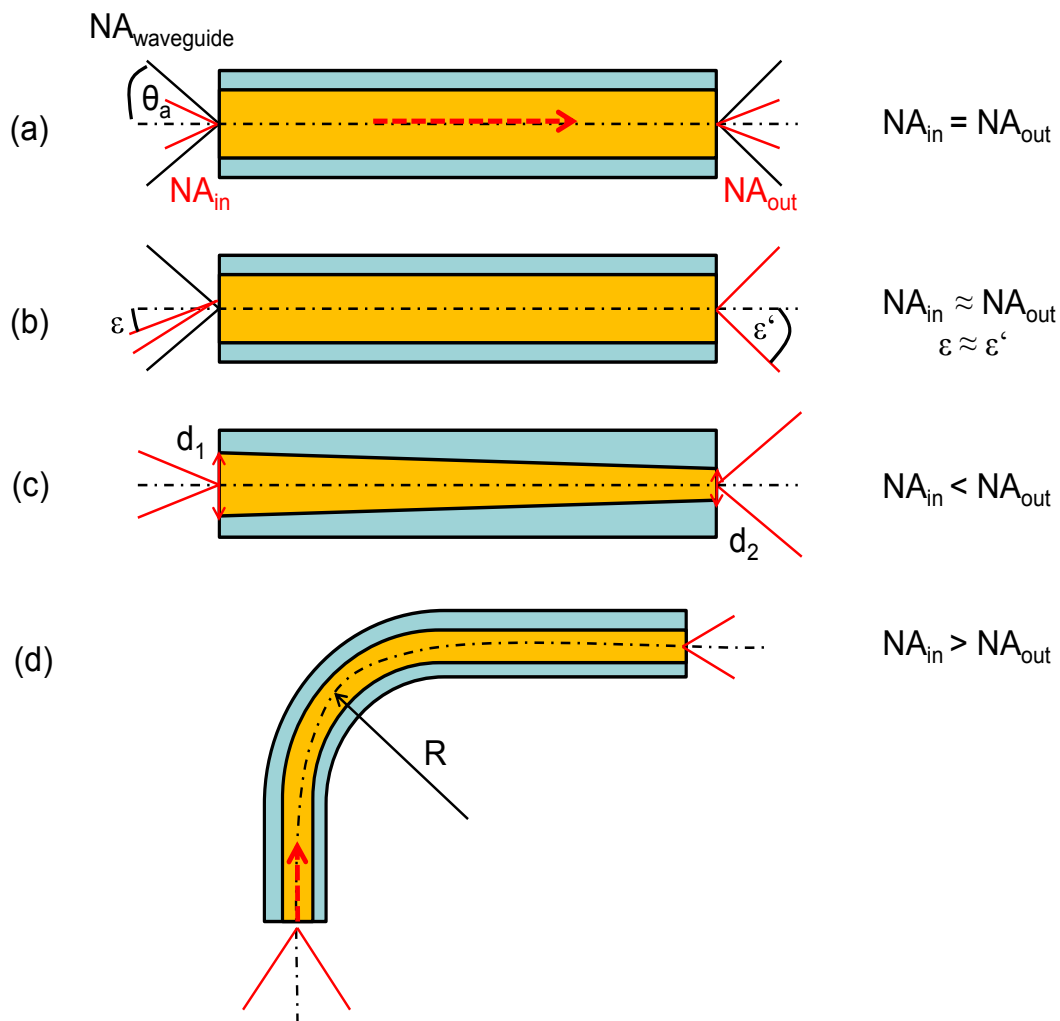


Figure 12 [70]: Radiation aperture of a waveguide for different angles of input coupling; (a) symmetric input coupling leads to symmetric output coupling, (b) symmetric output situation caused by asymmetric input situation, (c) tapered waveguide results in a change of the numeric aperture (NA), (d) waveguide bend shows less output transmission caused by scattering losses

2.3.1 End-fire and Butt-Coupling

End-fire and butt-coupling are very similar techniques, involving focusing light onto the end of the waveguide, either via a lens or by “butting” two waveguides or devices up to one another [35]. Both coupling options are based upon the modal overlap between the mode field of the “transmitting” and of the “receiving” device. End-fire coupling is mostly used for coupling the light into or out of a photonic circuit, e.g. by using an external light source or detector. In contrast, butt-coupling will be helpful for waveguide-waveguide interconnections [69]. However, in both procedures the introduced light can potentially excite all modes of the waveguide, because phase matching to a particular propagation constant of a specific mode does not occur. One again, the overlap integral of the modes determines the coupling efficiency which depends on the experimental alignment and the size and shape differences of the coupled devices. The alignment problem can be accomplished using stages positioned by piezoelectric micrometers [69] or accurately etched slots (V-grooves) in the substrate to achieve less coupling losses [68, 69].

In general, not all rays entering the waveguide or fiber core will continue to be propagated down its length. The geometry concerned with launching a light beam into a photonic structure is subjected to the terms and conditions of the TIR and the acceptance angle θ_a [34]. Rays to be transmitted by the TIR within the core must be incident on the waveguide core within the acceptance angle defined by the conical half angle θ_a as shown in Figure 12. Moreover, formula (45) describes the maximum angle to the axis at which light may enter the waveguide in order to be propagated.

$$\theta_a = \sin^{-1} \sqrt{(n_1^2 - n_2^2)} = \sin^{-1} NA \quad (45)$$

However, the coupling efficiency is given either as the fraction of the total power in the optical beam, which is coupled into (or out of) the waveguide, or in terms of a coupling loss in dB [69]. In the case of mode-selective couplers it can be determine independently for each mode, while multimode couplers are usually described by an overall efficiency [69]. Anyhow, sometimes it is possible to specify the relative efficiencies of various modes of a MM waveguide. Even so, the definition of the coupling efficiency η_c^m and the coupling loss L_c^m (dB) are given by [69]

$$\eta_c^m = \frac{P_m}{P_{in}} = \frac{\text{power coupled into (out of) the "m"th order mode}}{\text{total power in optical beam prior to coupling}} \quad (46)$$

and

$$L_c^m = 10 \log \frac{P_{in}}{P_m} = [dB]. \quad (47)$$

However, in the case of direct focusing or end-fire coupling the coupling efficiency η_c^m can be calculated from the overlap integral of the field pattern of the incident beam and the waveguide mode, as show in

$$\eta_c^m = \frac{[\int A(x)B_m^*(x)dx]^2}{\int A(x)A^*(x)dx \int B_m(x)B_m^*(x)dx} \quad (48)$$

where $\mathbf{A}(\mathbf{x})$ and $\mathbf{B}_m(\mathbf{x})$ are the amplitude distributions of the input beam and the m th mode [69]. In practice, gas-laser beams were coupled to the fundamental mode because of the good modal match between the Gaussian beam profile and the TE_0 waveguide mode shape. In theory, the coupling efficiency could be nearly 100 %, but usually 60 % in practice can be achieved [69]. Furthermore, the reflection \mathbf{R} from the waveguide endface is an important parameter, determined by the RIs of the media involved in coupling and described by the Fresnel equations [35]. In formula (49) the definition of \mathbf{R} is given by an approximation that the waveguide endface is due to the normal incidence of the beam.

$$R = \left| \frac{n_1 - n_2}{n_1 + n_2} \right|^2 \quad (49)$$

For an air/silicon nitride (Si_3N_4) interface, $n_1 = 1$ and $n_2 = 2$, this reflection is approximately 11 %. This means in particular, the quality of the waveguide endface is important and should be optimized due to the fabrication steps, e.g. etching parameters [35].

However, butt-coupling is most often used to couple a light source, e.g. laser diode, or a waveguide to another waveguide. As illustrated in Figure 13, the thicknesses of the light emitting layer of the light source (or a waveguide) h_L and the waveguide core h_c should be approximately equal, thus the field distribution of the fundamental laser mode (or the 1. waveguide) is well matched to TE_0 mode of the 2. waveguide [69].

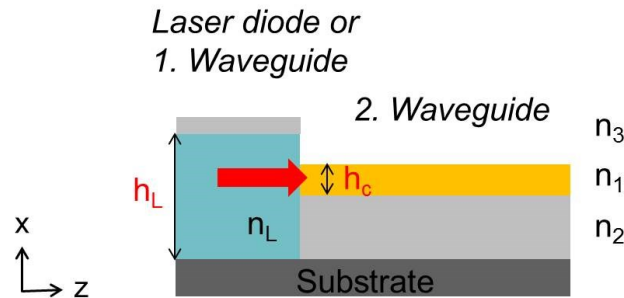


Figure 13 [69]: Schema of butt-coupling a laser diode/waveguide with an integrated 2. waveguide

This method is advantageous because in contrast to prisms, grating and taper coupling the relatively uncollimated beam of the injection laser diverges at a half-angle of typically 10 – 20° [69]. The other methods are very sensitive to the angle of incidence which requires special lenses for collimation of the input beam. Anyhow, the coupling efficiency between a laser diode (or waveguide) operating at the TE_0 mode and a 2. waveguide, as shown in Figure 13, is given by [69]

$$\eta_c^m = \frac{64}{(m+1)^2 \pi^2} \frac{n_{L1} n_1}{(n_{L1} + n_1)^2} \cos^2 \left(\frac{\pi h_c}{2 h_L} \right) \frac{1}{\left[1 - \left(\frac{h_c}{(m+1) h_L} \right)^2 \right]^2} \frac{h_c}{h_L} \cos^2 \left(\frac{m\pi}{2} \right). \quad (50)$$

Note that in the given equation (50) all waveguide modes are assumed to be well confined and that the light “transmitting” layer of the light source is thicker than the core of the coupled waveguide ($h_L > h_c$). The first factor in formula (50) is just a normalization term, while the second factor takes account of reflections at the laser/waveguide-waveguide interface, as already mentioned in formula (49). The other terms consider the modal overlap and the area mismatch in the field distributions of both devices. Moreover, there is no coupling to odd-order

waveguiding modes, because the fields have cancelling loops when their overlap integrals are taken with the even ($m = 0$) laser mode [69]. For instance, the coupling efficiency for the lowest-order waveguide mode can theoretically approach 100 %, if the thicknesses become equal. Thus, coupling into higher modes is nearly zero. Additionally, the coupling efficiency η_c is most sensitive to misalignment in lateral (z) and vertical (x) direction. Equation (51) shows, how a lateral displacement factor x of the waveguide relative to the laser decreases the coupling efficiency [69]

$$\frac{P_m}{P_{in}} = \cos^2\left(\frac{\pi x}{h_L}\right), \quad (51)$$

where P_{in} is the coupled power for $x = 0$, and it is assumed that $h_L > h_c$ and $x \leq (h_L - h_c)/2$. Anyhow, the vertical displacement in z -direction is also very critical and must be controlled with accuracy on the order of a wavelength to minimize the modulation of the effective reflectivity between the both endfaces [69]. The facts presented so far demonstrate the good efficiency of the butt-coupling method by means of light coupling between different devices taking into account the submicrometer alignment by piezoelectric stages and micrometer screws.

Furthermore, Quimby [71] theoretically investigated the coupling efficiency η_c for three different light sources to a fiber/waveguide: point source, lambertain source, laser source. The first one involves isotropic emission, in which light appears from a point, e.g. a rare earth (RE) element as Er^{3+} , in a homogenous medium. Since the light is distributed uniformly with angle, the point source coupling efficiency η_{c_point} into the photonic device is approximately given by

$$\eta_{c_point} = \frac{1}{4} \frac{NA^2}{n_0^2}, \quad (52)$$

where n_0 corresponds to the RI outside the waveguide, in which the point source is embedded. That is particularly the case for higher numerical aperture (NA) waveguides/fibers, which accept larger fraction of the emitted light from the point source [71]. Even so, it should be borne in mind that the point source is very close to the end of the optical device, because the solid angle for light collection (θ_a) is limited by the core diameter.

However, a LED belongs to lambertian light sources, also known as extended sources, in which the light is emitted over some surface area A_s [71]. Here, the estimated coupling efficiency η_{c_lamb} is given in formula (53) and is four times higher than that of the point source. Moreover, equation (53) assumes that the area of the light emitter A_s is bigger than the area of the coupled waveguide A_{wg} (or fiber: $A_F = \pi a^2$), because the coupling efficiency depends on the size of the emitting area compared with the area of the coupled waveguide.

$$\eta_{c_lamb} = \frac{A_{wg}}{A_s} \frac{NA^2}{n_0^2} \quad (53)$$

Obviously, another important definition is the laser coupling efficiency η_{c_L} , as show in formula (54). Here, the angular distribution θ (half angle) of the laser has to be taken into account (60), which determines the value m of the distribution (55).

$$\eta_{c_L} = 1 - \left(1 - \frac{NA^2}{n_0^2}\right)^{m+1/2} \quad (54)$$

$$m = \frac{\ln 0.5}{\ln(\cos \theta^\circ)} \quad (55)$$

2.3.2 Prism and Grating Coupling

The coupling methods described can be used when the endface of the waveguide is exposed. In some integrated circuits only the device surface is freely accessible for light in- and out-coupling. However, for coupling to occur to an individual mode, the phase-match condition in formula (56) must be fulfilled.

$$\beta = k_z = k_0 n_3 \sin \theta_a \quad (56)$$

The incident beam is defined by an angle θ_a at the waveguide surface and will propagate in the upper cladding n_3 with a propagation constant $k_0 n_3$ in z-direction. Thus, the components of the phase velocities of the waves in the beam and in the waveguide mode must be the same in the direction of propagation (z) [69]. This is the case, if $\beta \geq k_0 n_3$, whereby such a condition can never be met, since $\sin \theta_a$ will be less than unity [35]. Therefore a prism or grating is required to couple light into the waveguide, because both can fulfill the phase-match condition (56) if correctly aligned. For prism coupling a maximum coupling efficiency of 80 % for a Gaussian beam shape can be achieved [69]. Anyhow, most semiconductor waveguides have RIs around 3 or 4 and are difficult to couple with prisms, because both the RI and the transparency of the prism material must be considered at the operation wavelength. Additionally, the incident beam needs to be highly collimated to satisfy the critical angle dependence of a certain mode. Thus, prism couplers cannot be used very efficiently with semiconductor lasers, which have a beam divergence of 10 – 20° without using an extra lens. In particular, vibration and temperature variations, and additional mechanical pressure holders for the prism make this method less useful in many practical applications [69].

However, as depicted in Figure 11 (b), a grating is a periodic structure. Usually, the grating is fabricated on the waveguide surface, functions to produce a phase matching between a particular waveguide mode and the optical beam and used as an input and output coupler. An optical mode with the propagation constant β_w will see modulations of the propagation constant due to the lattice constant Λ of the grating. Thus, the propagation constant of the mode β_p is defined by [69]

$$\beta_p = \beta_w + \frac{2p\pi}{\Lambda}, \quad (57)$$

where $p = \pm 1, \pm 2, \pm 3, \dots$, and only the negative p values lead to a phase match [69]. Thus, the phase-match condition for the fundamental mode ($p = -1$) in a waveguide becomes [69]

$$\beta_w - \frac{2\pi}{\Lambda} = k_0 n_3 \sin \theta_a. \quad (58)$$

As in the case of a grating coupler and a Gaussian beam shape, an optimum coupling efficiency of approximately 80 % is theoretically possible [69]. Especially, symmetric profiled gratings (saw tooth profile) have only efficiencies of 10 – 30 %, because of the energy loss into the substrate and the power coupling into higher-order diffracted beams, whereas asymmetrically shaped gratings show greater efficiency of 95 %, respectively [69]. The big advantages of a grating coupler is that, once fabricated, it is an integrated part of the waveguide structure independent of renewed alignment, vibrations or ambient conditions and it can be used on any high RI semiconductor waveguide. Anyhow, the disadvantages of the method are the high-angle dependence, thus the grating coupler cannot be used effectively with the divergent beam of a semiconductor laser, and the difficult fabrication process, which requires high-quality masks and etching techniques [69].

2.3.3 Tapered Waveguides

There are two different types of tapers: in adiabatic tapers the waveguide dimensions change so slowly that mode conversion is negligible [69, 72]. For example, if the input waveguide is multimode all the power in the higher-order modes is radiated away and the taper output enables a single mode signal. In contrast, applications like polarizers and polarization splitting/rotations are based on tapered waveguides for an efficient mode conversion with a very high efficiency (close to 100 %) when the taper is designed appropriately [73]. Moreover, a distinction is made between vertical and lateral tapers as illustrated in Figure 14 [72].

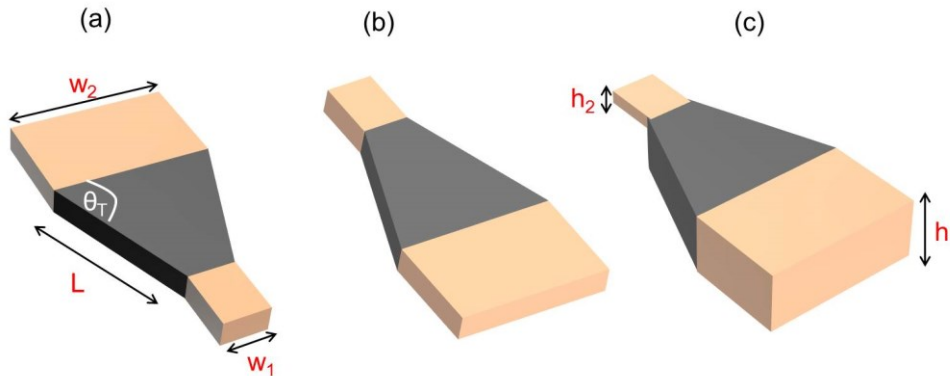


Figure 14 [72]: (a, b) Lateral down/up- and vertical up-tapered (c) waveguides with a taper length L , a taper angle θ_T for the coupling of two different sized waveguides (w_1 , w_2 , h_1 , h_2)

Moreover, Nelson [74] examined theoretically that tapered waveguides lead to less critical coupling tolerances for transverse alignment displacements, but tighter tolerances for angular misalignment. Additionally, such tapers are often used to change the light spot size in order to have better coupling efficiency between two devices of different cross-section. For example, the coupling between a SM fiber with a MFD of $9 \mu\text{m}$ and a Gaussian Beam profile and a $1 \mu\text{m}^2$ waveguide with a other beam profile results to a large modal mismatch between the devices leading to a coupling loss of at least 14 dB [75]. Dai et al. [76] observed almost 100 % mode conversion between the fundamental TM mode and the first higher-order TE mode in a down-tapered submicron SOI rib waveguide for the realization of a polarization splitter-rotator. Galán et al. [77] also found out that direct end-fire coupling between a SOI SM waveguide and a SM fiber produces around 20 dB of coupling losses for TE polarization at 1550 nm input wavelength. However, mode conversion can be depressed by carefully choosing the taper parameters, which is necessary for applications when low-loss propagation of the fundamental TE or TM mode is needed. One design rule is usually to make the tapered section long enough to be “adiabatic” so that higher-order modes are not excited [78]. In addition to the geometry, the RI of the upper cladding plays a important role that the mode conversion could be eliminated or enhanced accordingly due to the mode hybridization by choosing the same material for the upper and lower cladding as in SOI strip waveguide [75]. On the other hand, the hybrid modes can be used to develop new TE/TM converters. Mertens et al. [79] present a tapered device which converts an input TE polarization into a mixture of TE and TM polarization, making it an interesting candidate for coherent receiver chips. Hosseini et al. [80] developed a tapered MM interface device to convert the fundamental and second-order TE modes of different wavelengths into the fundamental mode signals of a SM output waveguide. However, theoretically analyzes of different taper structures can be performed by numerical methods using FEM, mode expansion and propagation tools applied to a staircase approximation of the taper profile [73, 75, 77, 81]. In this context, this work mostly focuses on two-dimensional calculations of adiabatic tapers for an efficient coupling between a SM fiber/the Si-based LED and the different sized waveguides without any mode conversion.

2.4 LOSSES IN INTEGRATED OPTICAL WAVEGUIDES

Four types of losses are generally distinguished, associated with the waveguide design and the quality of the material in which the waveguide is fabricated [35]. Whatever the fabrication process looks like, optical losses within the waveguide can be attributed to scattering losses (volume scattering, surface scattering), absorption losses (band edge and free carrier absorption), radiation losses (bending losses) and conversion losses (dispersion losses) [35, 82]. Furthermore, the theory of the already introduced coupling methods, e.g. end-fire or prism coupling, is useful for waveguide loss measurements. The basic measurement techniques, e.g. the cut-back method, for the determination of optical losses are described at the end of this section.

Generally, an actual loss L [69], e.g. an optical return loss, is represented by the unity **dB** as given by

$$L = 10 \log \left(\frac{I_0}{I} \right) = [dB], \quad (59)$$

where I_0 is the initial and I the returned intensity.

For a quantitative description of the magnitude of the optical loss L in a photonic structure an exponential loss coefficient α (loss per unit length) is used. Here, the intensity at any point z of the waveguide is described by

$$I(z) = I_0 \exp(-\alpha z), \quad (60)$$

where I_0 is the initial intensity at the distance $z = 0$. Moreover, a combination of formula (60) and (61) leads to an expression for the attenuation coefficient α (63), which takes account of all the different loss mechanisms encountered in a waveguide.

$$L = 10 \log \left(\frac{I_0}{I} \right) = 10 \log[\exp(\alpha * z)] \quad (61)$$

$$L = 10 \log(e) * \alpha * z \quad (62)$$

$$\alpha = 4.34 * \alpha' = [dB \text{ cm}^{-1}] \quad (63)$$

Here, the loss is expressed in **dB/cm** which is equivalent to $4.34 * \alpha'$, whereby the unit for α' is cm^{-1} . Moreover, it is worth considering what sort of loss can be tolerated for the integrated photonic circuit. The most expected benchmark in literature for loss is of the order of 1 dB cm^{-1} , because a typically optical circuit is a few cm in length [35]. Especially, losses for SOI waveguides are in the range $0.1 - 0.5 \text{ dB cm}^{-1}$ [35].

However, scattering in an optical waveguide can result from two different sources [35]: surface scattering and volume scattering. The latter is caused by imperfections in the bulk material of the waveguide, e.g. crystalline defects, and depends strongly on the relative size of the imperfections compared to the wavelength in the material. The loss per unit length is proportional to the number of scattering centers per length. Experience shows that in the bulk material Rayleigh scattering is the dominant loss mechanism, which exhibits a λ^{-4} dependence [35]. In the case of wavelengths longer than the correlation length a λ^{-3} dependence can be expected [35]. Accordingly, volume scattering is negligible. In contrast, however, surface

scattering has been studied by many authors with publishing complex approximating methods for the expression of scattering from the surface or interface of the waveguide. Tien [83] introduced 1971 a simpler technique which is based on the specular reflection of power from a surface. This condition is shown in equation (64) and hold for long correlation lengths, which can be assumed in most cases. The specular reflected power P_r of a beam with the incident power P_i is given by [83]

$$P_r = P_i \exp\left(\frac{4\pi\sigma n_1}{\lambda_0} \cos \theta_1\right), \quad (64)$$

where σ is the root-mean-squared (rms) roughness of the waveguide surface, θ_1 the propagation angle of a certain mode and n_1 the RI of the waveguide core material. Given these assumption, Tien [83] produced an expression for the loss coefficient α_s due to interface scattering of the form [34]

$$\alpha_s = \frac{\cos^3 \theta_1}{2 \sin \theta_1} \left(\frac{4\pi n_1 (\sigma_u^2 + \sigma_l^2)^{1/2}}{\lambda_0} \right)^2 \left(\frac{1}{h + \frac{1}{k_{yu}} + \frac{1}{k_{yl}}} \right) = [cm^{-1}], \quad (65)$$

where $\sigma_{u,l}$ is the rms roughness of the upper or lower waveguide interface, $k_{yu/l}$ the y-directed decay constant in the upper/lower cladding, and h the waveguide core thickness. For example, in thin waveguide films made of glasses and oxides, surface variations of ~ 100 nm lead to interface losses of 0.5 – 5 dB/cm [69]. In semiconductors as SOI waveguides thickness variations of ~ 10 nm can result in scattering losses above 30 dB/cm [84].

Absorption losses in a waveguide based on semiconductor materials cannot be neglected. Interband absorption and free carrier absorption are the two main potential sources of absorption losses in semiconductor waveguides [35]. The design of the waveguide material composition is important, because the operating wavelength should not lie below the energy gap of the material [69]. If this is the case, photon absorption occurs resulting in an electron excitation from the valence to the conductive band. For example, the band wavelength of Si is approximately $1.1 \mu\text{m}$, above which Si acts as guiding layer and below it absorbs very strongly, thus photodetectors in the visible light range are based on Si [35]. In comparison, Figure 15 shows the optical band gap E_g of Si_3N_4 due to the Si excess (blue numbers in at %) before (black dots) and after (red dots) 1000°C furnace annealing (FA) [85].

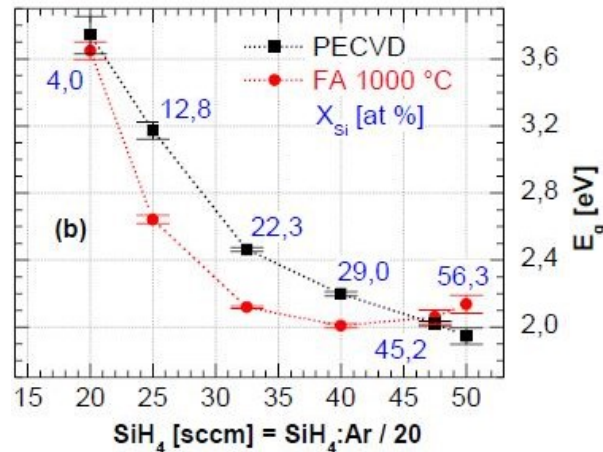


Figure 15 [85]: Band gap (E_g) behavior for Si_3N_4 films with different Si excess before (black dots) and after (red dots) 1000°C furnace annealing

As can be seen from Figure 15, the band gap energies of the deposited Si_3N_4 layers typically range between 1.9 eV and 3.7 eV or $0.65 \mu\text{m} - 0.34 \mu\text{m}$. Additionally, annealed Si-rich Si_3N_4 layers show a red-shift of the band gap energy [85]. However, free carrier absorption is significant in semiconductor materials, too. This occurs, when photons transmit their energy to electrons in the conduction band or to holes in the valence band [82]. In Si, the concentration of the free carrier density is used to specifically modulate the RI of the layer influencing the absorption behavior [35]. Changes in the absorption can be described by the well-known Drude-Lorentz equation [35]. Therefore, Soref et al. [86] showed the dramatic effect of doping a semiconductor, e.g. by an injected hole/electron concentration of 10^{18} cm^{-3} , leading to high absorption losses of 10.86 dB/cm, respectively.

However, radiation losses are caused by the dissipation of the energy of a guided mode into the upper and lower cladding, named leaky modes or cladding modes. This only relates to high-order modes in straight waveguides, in bends or operating at the cut-off [35, 82]. An optimized fabrication process of the photonic structure and a correct curvature radius avoid radiation losses. Miller [87] concluded by theoretical examinations that the radiation loss coefficient depends exponentially on the radius of the bend. Furthermore, Goell [88] has summarized the radiation losses in several typical dielectric waveguide structures due to the minimum bending radius. Anyhow, the thickness of the lower cladding, referred to as box layer thickness, must be significant thick to prevent coupling into the Si substrate [35]. Clearly, the penetration depth and thus the box layer thickness vary for each mode according to the waveguide dimensions and the operating wavelength.

In ideal guiding structures it can be assumed that the modes are orthogonal and thus no energy transfer between them occurs [82]. However, in reality, a low-order confined mode can couple with high-order modes resulting in conversion losses. This is caused by dispersion loss, distinguishing between modal dispersion and polarized modal dispersion (PMD) depending strongly on the quality of the fabricated photonic structure. Especially, modal dispersion is a critical factor in optical telecommunication systems ($\lambda = 1550 \text{ nm}$), thus the duration of an optical pulse increases during propagation and is overlapping with other pulses resulting in transmission errors. The PMD is associated to SM waveguides or fibers, where a signal normally consists of two polarizations, which usually travel with the same speed. Existing imperfections in the bulk material affect the phase velocities leading to a spreading of the signal [89]. For the most applications the loss coefficient of the PMD is usually less than 0.5 ps/nm/km. Anyhow, the major sources of dispersion are material dispersion and waveguide dispersion. Every signal consists of a range of wavelengths, which may be only a fraction of a nanometer wide and the RI of the waveguide material is wavelength dependent (n_{eff}) [89]. Therefore, different wavelength components travel with different speed which is leading to material dispersion, also named chromatic dispersion [89]. Moreover, there is a second component, called waveguide dispersion. The light energy of a mode propagates partly in the core and in the cladding of the waveguide, thus the ERI of the mode lies between the RI of these two limits. If most power propagates in the core, the ERI is closer to the RI of the core (n_1) and vice-versa. In particular, the power distribution of the mode is due to the operation wavelength and will shift into the cladding for longer wavelengths. Therefore, shorter wavelengths tend to travel more slowly than longer ones resulting in a dispersed signal [89]. Especially, in fibers/waveguides with larger cross-sections (modal areas) is waveguide dispersion negligible, but material dispersion dominant.

However, the optical loss measurement methods typically base on the already mentioned coupling methods in chapter 2.3. Mostly, they consist of comparing the power of the light propagating in the waveguide with the launched power of the beam [82]. In practice, the problem of in- and out coupling is difficult to manage and introduces extra losses. Anyhow, the loss measurement method depends upon the information required from the experiment. For

example, it is useful to select the prism or grating coupling technique if the optical loss associates with particular modes of the waveguide. If, however, the total loss of the photonic structure is required, end-fire or butt-coupling is the method of choice according to the simplicity of operating [35]. Additionally, an intensive study of the origin of the loss makes the optical loss determination more complicated, because there is often confusion between insertion and propagation losses. The latter is the loss associated with light propagation the waveguide, excluding coupling losses [35]. In the case of design optimization of a photonic structure it is usually the propagation loss that is of interest, as well as here. Moreover, the propagation loss in a waveguide will be always greater than in the bulk material due to the fabrication processes, e.g. E-beam lithography or RIE. As mentioned above, scattering losses from imperfections, intrinsic defects in the material or poor surface smoothness limit the device applications and lead to significant propagation losses [90]. Anyhow, there are three main experimental techniques to determine optical waveguide losses: the cut-back method, the Fabry-Perot resonance method and scattered light measurement [35]. Especially, the first technique was used in this work, thus the other have been not included.

The simplest technique using end-fire or butt-coupling for the determination of the attenuation coefficient α (63), which is equal the sum of all losses in a photonic structure. Moreover, Figure 16 illustrates a typically attenuation spectra for Silicon-on-insulator (SOI) based optical fibers with a characteristic loss minimum (low-loss “window”) at 1550 nm.

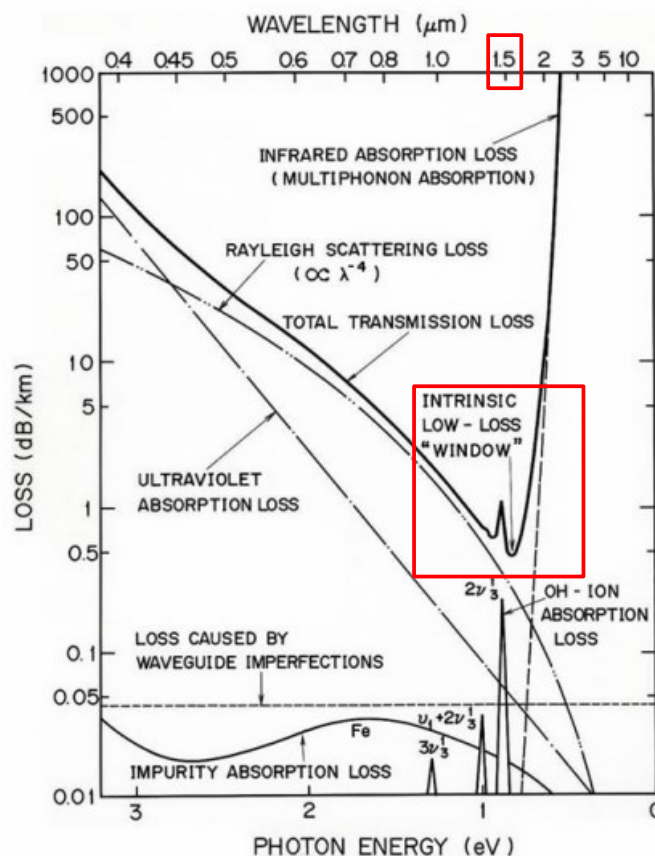


Figure 16 [91]: Schematic diagram of the transmission loss mechanism in SOI-based optical fibers

One of the key challenges for the development of practical optical communication systems is the reduction of transmission loss in optical waveguides and fibers. The shown loss characteristic in Figure 16 recalls the most important loss aspects of this chapter: absorption loss due to the host material, Rayleigh scattering loss due to RI fluctuation of the core,

scattering loss caused by geometrical imperfections of the boundary fluctuation between core and cladding, and optical losses due to bending and splicing [91].

Anyhow, common measurement technique is the cut-back method which is based on coupling the beam into a waveguide of length L_1 , whereby the input power P_0 to the waveguide and the transmitted power P_1 from the waveguide endface are measured. Afterwards, the waveguide will be shortened to the length L_2 and measured again (P_2), while the input power P_0 is kept constant. Thus, the propagation loss (or attenuation coefficient) α of the waveguide length ($L_1 - L_2$) is related to the ratio of the measured output powers, and can be expressed as [35]

$$\frac{P_1}{P_2} = \exp(-\alpha(L_1 - L_2)), \quad (66)$$

i.e.

$$\alpha = \left(\frac{1}{L_1 - L_2} \right) \ln \left(\frac{P_1}{P_2} \right) = [dB \text{ cm}^{-1}]. \quad (67)$$

The determined value in formula (67) has been produced by only two data points and is neglecting the input coupling loss, the condition of the waveguide endfaces and the input power P_0 . The accuracy can be improved by multiple measurements for certain waveguide lengths and by plotting the obtained optical loss against the length [35]. The slope of the best fit straight line of this plot corresponds to the waveguide propagation loss α , and the intercept with the y axis reflects the average of the input/output coupling loss (dB). Moreover, one benefit of this method is the constant launch condition, e.g. the coupling efficiency of the light source remains between the initial and the cutback measurements. Additionally, the experimental conditions, such as the gap between the waveguide endface and the objective lens, easily influence the coupling efficiency. Nevertheless, it is a non-selective method, because all guided modes are simultaneously excited, thus the mode conversion component of the total loss cannot be separated [82]. Furthermore, a precise alignment is required and steep or polished waveguide endface are preferred.

3 SIMULATION TOOLS USED IN DESIGN

Optical devices can be classified based on their geometry, e.g. one-dimensional slab waveguides, two-dimensional channel waveguides, standard or microstructured fibers, bended waveguides, tapers and photonic crystals of certain dimensions. Other distinctions are the guiding mechanism of the light signal in the optical device, like TIR or the photonic band gap, the modal structure (SM/MM) and the material composition (Δn). In order to valid qualitatively the optical properties and losses of different designed photonic structures for the implementation in integrated circuits various simulation methods are necessary. The following chapter discusses numerical and analytical techniques to simulate and optimize the performance of these optical devices and their coupling efficiency to other optical components as the Si-based LED according to the operating wavelength, their geometry and material composition.

3.1 MATLAB

The theoretical analysis of a symmetrical or asymmetrical planar waveguide can be obtained by one-dimensional calculations using a MATLAB code for solving the dispersion relations [35], as defined in formula (17)-(20), due to the geometry, especially to the waveguide core height h , and the operating wavelength λ . These important wave characteristics will be used to express the propagation constant β and the ERI (n_{eff}) with the help of the propagation angle θ_1 for each polarization. This technique is particularly suitable to determine the maximum number m of guided modes in several waveguide geometries due to the excitation wavelength. Thus, this method gives an evidence of the design parameters for e.g. SM propagation at a particular wavelength. In this study, a MATLAB code was developed for design optimization, which is shown in the appendix (chapter 9). Anyhow, in comparison to analytical solutions by plotting the phase constant ϕ vs. the propagation angle θ_1 , more detailed analysis of the guided modes can be performed in two-dimensional structures by various numerical methods such as the ERI method [35, 92, 93] and the FEM [34, 35, 94, 95], which are discussed in the following sections.

3.2 EFFECTIVE REFRACTIVE INDEX METHOD

In the early days of integrated optics, the effective refractive index method (ERIM) [96] was a powerful and often used technique [92, 93, 97, 98] to find an approximate solution for the ERI n_{eff} of the core material in a two-dimensional rectangular waveguide based on a core height h and a core width w [35]. Moreover, since the light is confined in two directions pure TE and TM modes are unable to satisfy all of the necessary boundary conditions. Therefore, a more complex type of solution is required, thus TE-like (E_{mn}^y) and TM-like (E_{mn}^x) modes are used [99, 100]. Anyhow, the analysis of the quasi-TE modes is carried out according to the following sequence (for the quasi-TM case it is reversed) [35, 82, 99]: the rectangular waveguide core is decomposed into two planar waveguides as shown in Figure 17 (b, c), where at first a TE polarized E-field is assumed which is parallel to the y-direction. Therefore, the x dependence of the y component of the $E_{m,y}(x)$ field can be obtained by solving the dispersion relation (19) for the propagation angle θ_1 according to the core height h . Thus, n_{eff} for a vertical planar waveguide of core width w is received. This can be done by an analytical or numerical method, e.g. with a MATLAB code. Now, the y dependence of the y component of the $E_{n,y}(y)$ field by solving the dispersion relation (20) for the TM polarized E-field can be obtained (Figure 17 (c)). Finally, this results in the $n(x,y)$ as well as in the propagation constant β (13) of the rectangular waveguide. Note that $E_{n,y}(y)$ for a quasi-TE mode of the original channel waveguide is obtained from the E_y component of the TM_n field, whereas $H_{n,y}(y)$ for a quasi-TM mode is obtained from the H_y component of the TE_n field of the effective vertical planar waveguide (c). This solving

order need to be fully respected regarding the correctness of the solutions [34]. In practice, this method is a good approximation if the waveguide satisfies the following conditions [46]: (1) the waveguide width is larger than its thickness and (2) waveguiding in the y -direction across its width is not stronger than that in the x -direction across its thickness. However, this technique shows only good results for well confined modes, far away from the cut-off frequency. Generally, the method will overestimate the propagation constants of the waveguide modes. Thus, it is used to simplify a two-dimensional transversal waveguide structure to a one-dimensional structure which can serve as a starting point for further analysis methods like FEM.

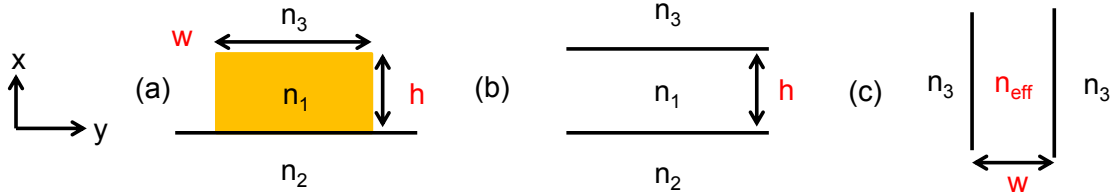


Figure 17 [82]: Generalized rectangular waveguide (a), Decomposition into two imaginary planar waveguides (b, c)

3.3 FINITE ELEMENT METHOD

The finite element method (FEM) has been widely utilized in the analysis of different photonic devices due to their geometry and material properties. Here, interest is focused on the mode profiles, cut-off frequencies and ERIs for optimization of the waveguide geometry due to the integrated photonic system [34, 94, 95, 101, 102, 103, 104, 105, 106, 107]. For example, the waveguide modes for homogeneous structures of arbitrary cross-sections in the x - y plane are simulated using a two-dimensional scalar FEM formulated for certain eigenvalue problems. In this work, wave propagation in z -direction is assumed, where the fields \mathbf{E}_z or \mathbf{H}_z have to satisfy the scalar Helmholtz equation (68) with Dirichlet (69) and Neumann (70) boundary conditions for the TE- and the TM-like modes [94].

$$\frac{\partial^2 \Phi}{\partial x^2} + \frac{\partial^2 \Phi}{\partial y^2} + k^2 \Phi = 0 \quad (68)$$

$$\Phi|_S = 0 \quad (69)$$

$$\frac{\partial \Phi}{\partial n}|_S = 0 \quad (70)$$

Here, Φ is the scalar wave amplitude function which is equal to either \mathbf{E}_z or \mathbf{H}_z . If the waveguide walls are closed and ideally conducting (perfect electric/magnetic conductor – PEC/PMC) the equations in both can be solved independently one from each other, because also the boundary conditions ((69), (70)) split into two independent conditions: one for \mathbf{E}_z (71) and one for \mathbf{H}_z (72). Therefore, with the help of the boundary conditions the eigenwaves in a waveguide can be classified as TE and TM waves.

$$E_z|_S = 0 \quad (71)$$

$$\left. \frac{\partial H_z}{\partial n} \right|_s = 0 \quad (72)$$

However, FEM solves equation (73) by minimization of the corresponding functional given by [94]:

$$F(\Phi) = \frac{1}{2} \iint_s \left[\left(\frac{\partial \Phi}{\partial x} \right)^2 + \left(\frac{\partial \Phi}{\partial y} \right)^2 - k^2 \Phi^2 \right] ds, \quad (73)$$

where \mathbf{s} represents the cross-sectional area of the waveguide [94]. After imposing proper boundary conditions ((71), (72)), the variation problem is discretized into a linear system of equations from which the eigenvalue \mathbf{k} and mode function Φ for quasi-TE and TM modes can be determined. Anyhow, in this work, the simulations were carried out with COMSOL and FlexPDE.

4 SIMULATION AND DESIGN

In this section the theoretical concept of a Si-based integrated microphotonic circuit is presented. Besides the general system structure, the individual components, e.g. the Si-based integrated light emitting device (LED) working as the light source, are introduced. The principal focus is on the design and simulation of Si_3N_4 strip waveguides and tapers as effective optical interconnects for potential butt-coupling to the Si-based light source. In addition, the study also examined the light propagation in various waveguide bends and photonic crystals. Moreover, the coupling efficiency as well as SM operation were studied and optimized due to certain operation wavelengths and structural parameters with the help of above mentioned simulation tools.

4.1 SYSTEM DESIGN AND INTEGRATION SCHEME

Integrated optical sensors cover a wide spectrum of applications, ranging from environmental and biochemical control, medical diagnostics, healthcare to process regulation. Thus, the specified usage of the sensor requires a particular system design and functionalization. Moreover, for biomolecular sensing, chipintegrated waveguide structures are promising detection elements for many lab-on-a-chip applications [11, 12, 13, 14, 15, 16, 17, 18]. There exist a lot of different sensor classes, like grating-coupled, interferometric, resonant microcavity and PhC sensors which still have yet to move beyond the proof-of principle demonstrations [108]. Especially, biochemical sensors incorporate electronic and photonic devices for the detection of harmful substances e.g. oestrogen in drinking water [4, 5, 3], whereby the integrated photonic structure is the essential interconnect. Additionally, the physics of waveguide operation and their utility function as an analytical device are quite simple [108]. Therefore, this work deals with developments in the coupling between a Si-based LED [4, 5] and a Si_3N_4 strip waveguide as well as other optical structures and interconnects, as the basis for the future design of integrated photonic detection systems, as illustrated in Figure 18 (a - c).

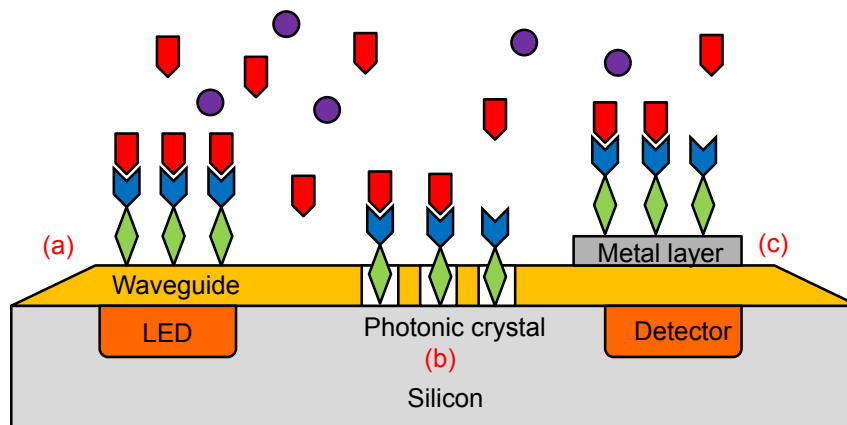


Figure 18: Three different Si-based integrated photonic circuits; Immobilization of the analyt (red) can occur on a modified waveguide surface (a), a PhC (b) or a metal film (c)

The shown sensor concept is based on a LED, working as the light source, a waveguide (or PhC) below a bioactive layer (green/blue) and a receiver for the detection of a certain organic pollutant (red). The structure as well as the fabrication of the LED will be explained in more detail in the following chapters. Furthermore, as Figure 18 implies, there are three possible detection mechanisms of the future biosensor. The analyte of interest (red), e.g. oestrogen in drinking water, can be immobilized on a functionalized waveguide surface (a), or on an implemented PhC (b), or the excitation of surface plasmon polaritons at a metal film (c) can be

used to detect the pollutant. However, due to the RI contrast (Δn) between the core and the cladding of the photonic structure, light is guided through the device by TIR, which generates an evanescent optical field that decays exponentially from the sensor surface. Thus, biomolecular binding events lead to a significant change of Δn and result in a shift of the resonance wavelength at the detector. This means that it is possible to construct sensors responsive to target biomolecular analytes of interest by monitoring the coupling and/or propagation properties of light through a photonic structure [108].

Anyhow, as already mentioned in chapter 2.3, the most difficult task is the efficient coupling between the optical device and the light source/detector. Therefore, this work special focuses on a powerful connection between the Si-based LED, the Si_3N_4 waveguide or other optical interconnects. In contrast, common optical biosensors [21, 22, 23] were realized by coupling light from an external laser diode into the optical device, where the evanescent field of the guided light excites an immobilized dye-labeled analyte. Most biosensing applications [31, 33, 109, 110] require complex coupling techniques of the external light source or highly structured grating couplers [111, 112] as well as the usage of expensive markers. Moreover, there are already examples which deal with the coupling problem between the photonic structure and an integrated photodetector [113, 114, 115, 116, 117, 118, 119, 120]. Nevertheless, relatively few studies exist solving the input coupling problem efficiently and cheaply as possible. Park et. al [121] taking advantage of III-V-based nanowires, while Khasminskaya et. al [122] used electroluminescent integrated carbon nanotubes as potential in-plane light sources. Because of the need of rather complicated fabrication techniques, in contrast to standard CMOS technologies, Shimizu et. al [123] and Yamada [124] utilized the flip-chip bonding technique by mounting a laser diode array on a Si-based optical waveguide platform. Conversely, Xu et. al [125] shows that a developed waveguide-coupled microdisk containing Ge quantum dots is a potential on-chip optical data link with capability of bidirectional transmission in the field of data processing.

In this work, the particular interest is primarily in butt-and taper-coupling of several waveguide structures and other optical interconnects to integrated Si-based LEDs on a Si platform. Here, the choice of suitable design parameters and useful material consumptions of all devices lead to high CMOS compatible systems, which can be fabricated by existing low cost Si technologies. For example, the confinement factor (43) of the light in the waveguide, the geometrical arrangement of the waveguide core and the luminescence layer of the LED (50), and the operation regime (SM/MM) determine the total power throughput of the integrated structure. An efficient coupling depends on these and many more parameters as well upon the operation wavelength and the geometry of the photonic structures, which have been investigated with several simulation tools from chapter 3 and are described in the following sections. Additionally, the subsequent chapters explain the structure and functionality of the Si-based LED and its functionality as a possible integrated light source. Afterwards, the fabrication of the optical and optoelectrical devices will be discussed in more detail in chapter 5.

4.1.1 Si-based LED as Light Source

An alternative promising version for simplifying the light injection process into a photonic system is the Si-based LED [4, 5, 126, 127], which consists of a metal-oxide-semiconductor (MOS) structure depicted in Figure 19. The LED is integrated in a Si-substrate (1) and composed of a SiO_2 layer system (2), which either includes a thin SiO_2 - (a) or a SiN_x -based (b) active luminescence layer (3) implanted with RE ions (e.g. Gd^{3+} , Tb^+ , Er^+) of a certain dose and energy. In contrast to the " SiO_2 "-LED (a), the SiON protection layer (4) for longer operation time [24], is in the latter structure replaced by the RE-implanted SiN_x layer resulting in a lower carrier injection barrier at the Si/ Si_3N_4 interface and a better electrical stability [126, 127]. Moreover, the choice of a specified front contact (5), e.g. indium tin oxide (ITO) or aluminium (Al), defines the

light radiation in vertical or lateral direction [4, 5]. For the latter case, the dielectric layer system can be assumed as a thin waveguide in which the light propagates sideways according to the Δn of the layers, their thickness, and the implantation profile of the RE element. Finally, a back contact (6) completes the LED structure. However, the precise fabrication details and structural parameters, e.g. layer thickness and implantation dose/depth, of both LEDs are given in chapter 5.

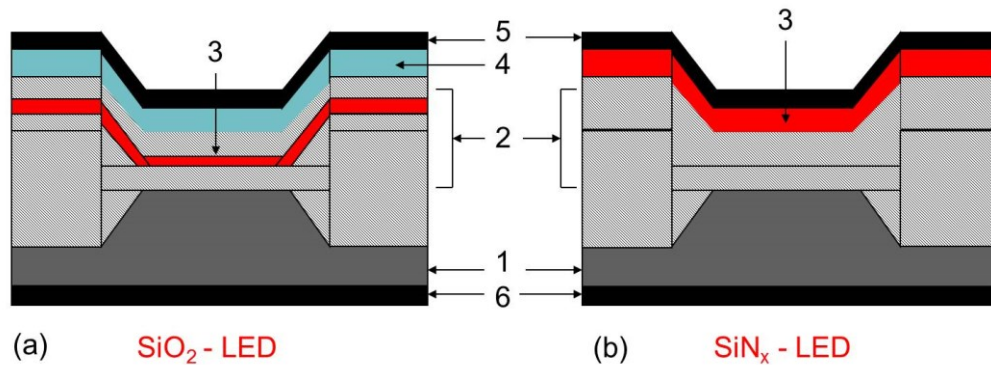


Figure 19 [4, 127]: Schematic cross-section of Si-based LEDs consisting of a Si substrate (1), a SiO_2 layer system (2) with embedded RE ions as the luminescence layer (3) [a], a SiON protection layer (4) and front/back contacts (5,6); or a RE-implanted SiN_x layer (3) [b]; not in scale

Furthermore, the electroluminescent (EL) excitation mechanism of the general Si-based LED is achieved by hot electron impact. The carrier injection occurs from the conduction band of the Si into the conduction band of the SiO_2 via Fowler–Nordheim or trap assisted tunnelling [126]. There, the electrons will be accelerated by the applied electric field and will gain kinetic energy. By impact excitation the hot electrons can transfer their energy to the implanted RE ion leading to the excitation of these luminescent centres. Their radiative relaxation back to the ground state will cause the observed EL. Further details of optical and electrical properties can be found in [126]. Moreover, a normalized EL spectrum of several RE-implanted LEDs is shown in Figure 20.

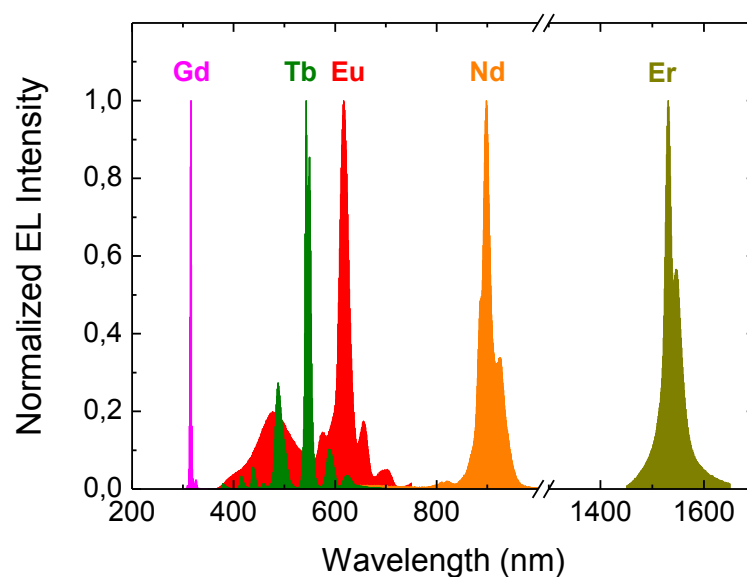


Figure 20 [126]: Normalized EL spectra of Gd^{3+} , Tb^{3+} , Eu^{3+} , Nd^{3+} and Er^{3+} -implanted Si-based LEDs

The relatively sharp main emission lines of the RE-implanted devices lie at 316 nm (Gd^{3+}), 541 nm (Tb^{3+}), 618 nm (Eu^{3+}), 850 nm (Nd^{3+}) and 1550 nm (Er^{3+}) and originate from electronic transitions within the 4f shell of the corresponding trivalent RE ion [126]. As these transitions are well screened from the chemical environment the peak positions and the intensity are quite sensitive to the chemical environment of the RE ion, e.g. the host matrix, and the excitation conditions. Anyhow, a critical point for many potential light source applications is the power efficiency. As in the previous year's shown, $\text{Tb}:\text{SiO}_2$ and $\text{Er}:\text{SiO}_2$ LEDs achieve an external quantum efficiencies (EQE) in order of 16 % [128] and 14 % [129]. Currently, Yerci et. al [130] fabricated $\text{Er}:\text{SiN}_x$ LED structures with an enhanced EQE by improved transport properties. In contrast, Berencen et. al [127] developed LEDs based on a $\text{Tb}:\text{SiN}_x$ matrix with a EQE of 0.1 %. Moreover, Cherkouk et. al [3] investigated a first biosensing application using Si-based LEDs as integrated light sources in a microfluidic cell plate for endocrine disrupting chemical (EDC) detection, like estrogenic activity, in waterish solution. These studies show the potential of the Si-based LED as integrated light source regarding to the high EQE of Tb^{3+} (541 nm) and Er^{3+} (1550 nm) ions, especially for biosensing or telecommunication applications. Thus, this work focuses on integrated photonic circuits based on Tb- or Er-implanted LED structures depending on SiO_2 or SiN_x matrices.

4.1.2 Waveguide Design and Coupling Techniques

In this section the structures under study are designed and simulated. Here, the main focus is on Si_3N_4 -based strip waveguides and waveguide bends of certain geometry due to the excitation wavelength of 541 nm (Tb^{3+}) and 1550 nm (Er^{3+}) for MM and SM operation. Especially, the design optimization for high modal confinement and SM guidance is particularly important for an efficient coupling between the Si-based LED and the waveguide, in which both the $\text{Er}/\text{Tb}:\text{SiO}_2$ and the $\text{Er}/\text{Tb}:\text{SiN}_x$ LEDs are under consideration. The main geometry parameters of the waveguide, like the critical height h_{max} for SM operation, the penetration depth of the evanescent field, scattering losses, the mode field distribution profiles and the coupling efficiency, are being investigated with the help of several analytical and numerical simulation tools. Thus, a direct coupling and a tapered coupling method are developed for connecting the Si-based LED and an integrated SM/MM waveguide, as shown in Figure 21. Furthermore, the light propagation in several PhC structures and waveguide bends was also investigated. Finally, the characterizations of the fabricated photonic structures are performed by structural and optical measurements discussed in detail in chapter 6 and 7.

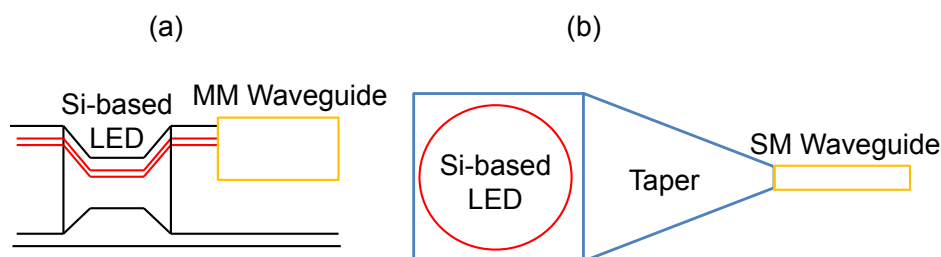


Figure 21: Two different butt-coupling methods between the Si-based LED and an integrated MM or SM waveguide; (a) cross-section of the direct butt-coupling method, (b) top view of the tapered butt-coupling method

4.1.2.1 SM/MM Waveguides and Bends

Here, the structure and the optical parameters of Si_3N_4 -based waveguides and bends are investigated. First, considerations are given about the light propagation due to the operation wavelength in one-dimensional (planar) symmetrical and asymmetrical waveguides. The

asymmetrical waveguide structures consist of a $1 \mu\text{m}$ (or $0.5 \mu\text{m}$) thick Si_3N_4 core with a lower SiO_2 cladding and an upper Air cladding on a Si substrate. In contrast, the symmetrical waveguide has SiO_2 as upper cladding. The used RIs of the layers at 541 nm and 1550 nm were obtained by ellipsometry and can be found in chapter 7. In particular, the solutions of the TE/TM dispersion relations ((17)-(20)) lead to the propagation angles θ_1 and respective ERIs (n_{eff}) of the guided modes due to the height h of the waveguide core and the excitation wavelength λ . Here, these values were calculated by an analytical method for the fundamental mode ($m = 0$) in planar waveguides and are shown in the graphical plots in Figure 22 (a - d).

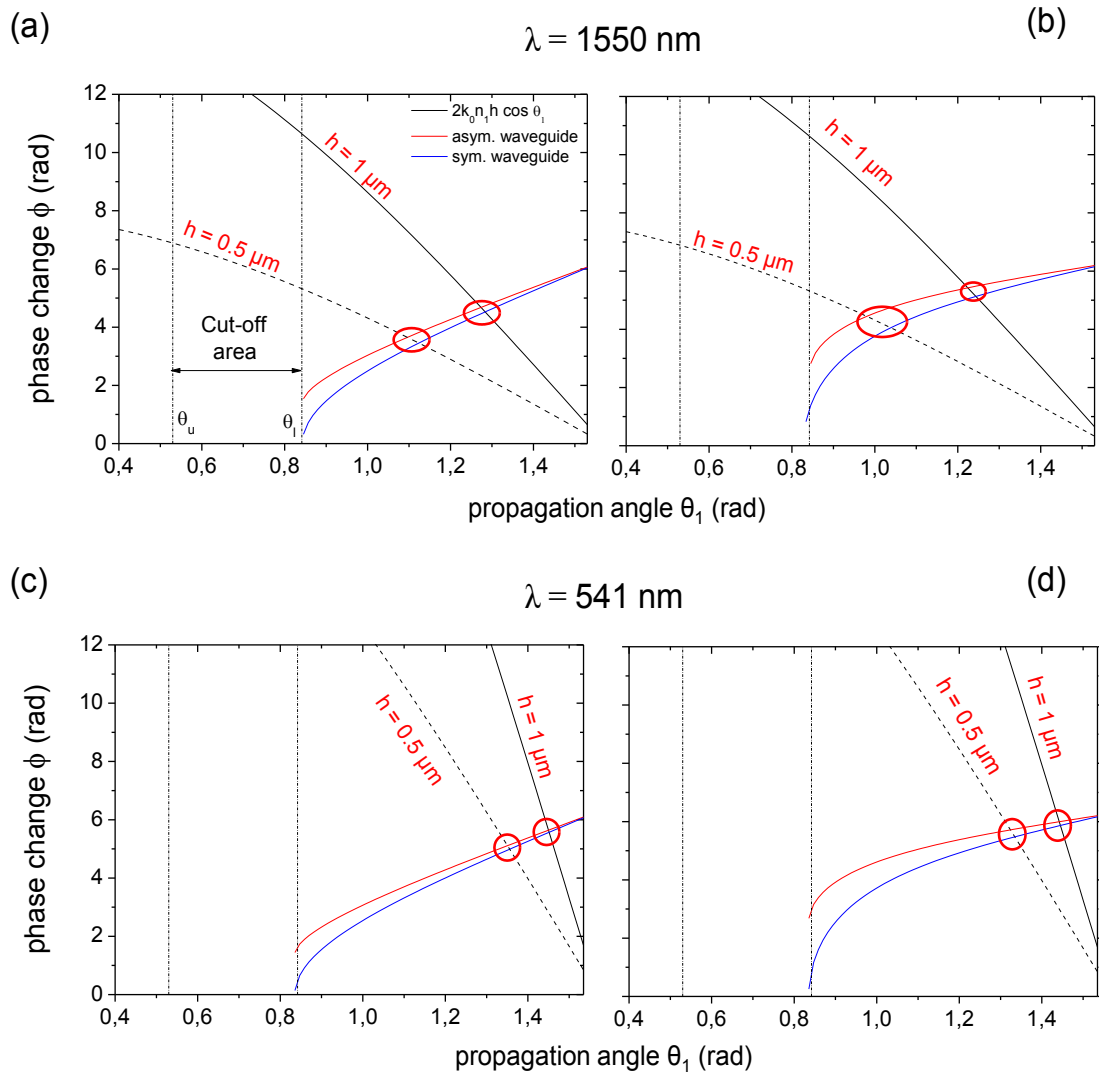


Figure 22: Propagation angles for fundamental TE/TM ($m = 0$) in asymmetrical (red) and symmetrical (blue) planar waveguides with two different core heights h due to λ ; TE (a) and TM (b) angles for $h = 1, 0.5 \mu\text{m}$ at $\lambda = 1550 \text{ nm}$; TE (c) and TM (d) angles for $h = 1, 0.5 \mu\text{m}$ at $\lambda = 541 \text{ nm}$

The plotted graphical solutions of the TE (a, c) and TM (b, d) eigenvalue equations show intersection points of the right-hand and left-hand side of formula (17) - (19) corresponding to the propagation angles θ_1 of the fundamental mode ($m = 0$). The critical angles for the upper (θ_u) and lower (θ_l) interface are added (vertical lines) and highlight the cut-off area in which the conditions for TIR are not met and the asymmetrical waveguide will be cut-off [35]. Anyhow, this analytical method lead to the following propagation angles θ_1 for two different waveguide core heights h and layer systems due to the two operation wavelengths summarized in Table 1 - Table 4. Furthermore, the calculations of the ERIs n_{eff} (16), the penetration depths σ^1 into the

lower cladding n_2 (31) and the MFDs $2\omega_0$ (32) were performed and the values have been added to tabled data.

Table 1: Summary of the obtained values from Figure 22 (a, b) for $m = 0$ and $h = 1 \mu\text{m}$ at 1550 nm

$h = 1 \mu\text{m}$ $\lambda = 1550 \text{ nm}$	Asym. waveguide		Sym. waveguide	
polarization	TE	TM	TE	TM
θ_1 (rad)	1.274	1.224	1.284	1.224
n_{eff}	1.883	1.853	1.89	1.853
σ^1 (nm) into n_2	209.38	218.76	130.56	218.76
$2\omega_0$ (μm)	1.36	1.36	1.26	1.44

Table 2: Summary of the obtained values from Figure 22 (a, b) for $m = 0$ and $h = 0.5 \mu\text{m}$ at 1550 nm

$h = 0.5 \mu\text{m}$ $\lambda = 1550 \text{ nm}$	Asym. waveguide		Sym. waveguide	
polarization	TE	TM	TE	TM
θ_1 (rad)	1.1	0.981	1.13	1.038
n_{eff}	1.756	1.637	1.782	1.697
σ^1 (nm) into n_2	256.98	342.3	245.04	290.99
$2\omega_0$ (μm)	0.93	1.03	0.99	1.08

Table 1 and Table 2 summarize the obtained values for an operation wavelength of 1550 nm. It is easy to recognize that in both waveguide structures a thinner core layer leads to smaller ERIs of the fundamental mode. Thus, less power propagates in the core, if the ERI is further away from the RI of the core ($n_1 = 1.97$) [35]. Moreover, the electric and magnetic fields are less concentrated near the core resulting in higher penetration depths into the lower cladding in a thinner waveguide core. However, both waveguide structures show only small difference between the ERIs of their TE and TM modes, whereby the asymmetrical waveguides show larger variations for both heights h . This means that the polarization dependence becomes less prominent in thicker waveguide cores, thus degenerated modes are found and the propagation loss is decreased [34, 35]. Additionally, it can be concluded that the usage of a SiO_2 upper cladding does not have a significant effect on the optical parameters of the waveguide. The high Δn in both structures leads to a centred guided fundamental mode, whereby the MFD is smaller in an asymmetrical design caused by a lower penetration depth into the Air cladding.

Furthermore, Table 3 and Table 4 summarize the obtained optical values for both waveguide structures with respect to an operation wavelength of 541 nm for the fundamental mode ($m = 0$).

Table 3: Summary of the obtained values from Figure 22 (c, d) for $m = 0$ and $h = 1 \mu\text{m}$ at 541 nm

$h = 1 \mu\text{m}$ $\lambda = 540 \text{ nm}$	Asym. waveguide		Sym. waveguide	
polarization	TE	TM	TE	TM
θ_1 (rad)	1.450	1.442	1.451	1.445
n_{eff}	1.995	1.993	1.996	1.994
σ^1 (nm) into n_2	64.76	64.91	80.76	80.54
$2\omega_0$ (μm)	1.11	1.11	1.16	1.16

Table 4: Summary of the obtained values from Figure 22 (c, d) for $m = 0$ and $h = 0.5 \mu\text{m}$ at 541 nm

$h = 0.5 \mu\text{m}$ $\lambda = 540 \text{ nm}$	Asym. waveguide		Sym. waveguide	
	TE	TM	TE	TM
polarization	TE	TM	TE	TM
θ_1 (rad)	1.350	1.324	1.356	1.334
n_{eff}	1.961	1.949	1.964	1.954
σ^1 (nm) into n_2	67.39	68.4	67.18	67.99
$2\omega_0$ (μm)	0.62	0.62	0.63	0.64

According to the tables above, the usage of a shorter wavelength results mainly in smaller penetration depths σ^1 into the lower cladding for both core heights h . Moreover, the ERIs of the two waveguide structures show again only minor differences, thus a SiO_2 upper cladding not derive any benefits. Once again, the polarization dependence is reduced in thicker waveguide cores. Anyhow, these results clearly demonstrate the influence of the core height and the operation wavelength on the optical parameters and the light guiding behavior of a photonic structure. Additionally, the obtained values show that a symmetrical structure does not greatly improve the light propagation in the waveguide core. Moreover, we may conclude from these findings, in particular by using an asymmetrical waveguide, a sufficiently thick lower cladding (box layer) prevents light coupling into the Si substrate [35]. In this context, it is clear that for longer wavelengths thicker SiO_2 layers are an advantage.

In this study, however, the number of guided modes with respect to the design and excitation conditions is much more important. Therefore, both, the normalized dispersion relations in equation (27) and (28) and the definitions of the critical height h_{max} ((21), (22)) are used to design a SM waveguide. Figure 23 (a, b) shows the V-b-plots of an asymmetrical waveguide with two different core heights h (1 or $0.5 \mu\text{m}$) due to the operation wavelengths of 1550 nm (a) and 541 nm (b).

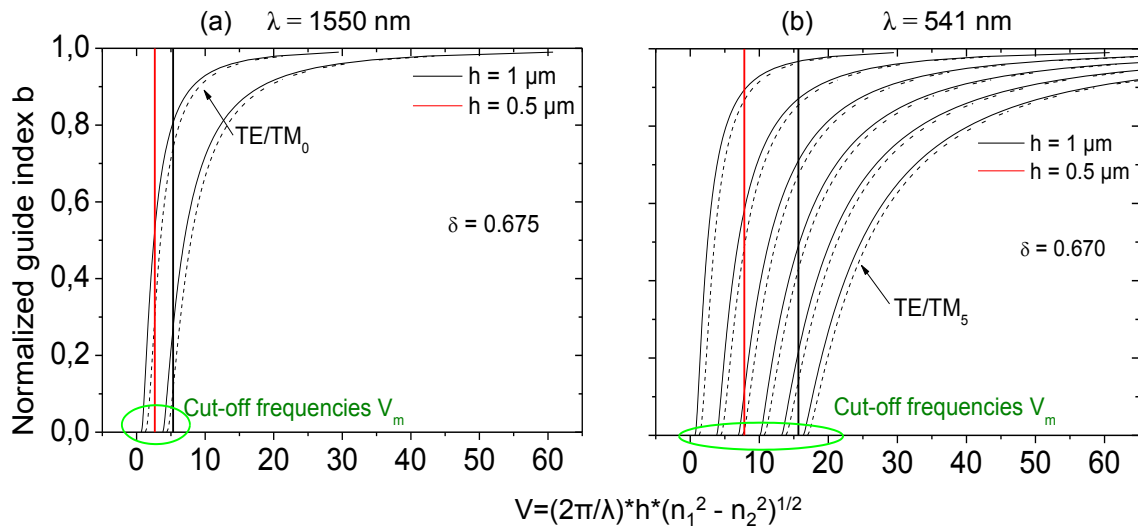


Figure 23: Normalized dispersion V-b plots showing the maximum number of guided modes in an asymmetrical waveguide due to the core heights $h = 1, 0.5 \mu\text{m}$ due to 1550 nm (a) and 541 nm (b)

A similar mode characterization method can be applied to the TE/TM dispersion relations by using the normalized guide index b and frequency V . Here, the ERI n_{eff} was substituted into the values of b which lie between zero and one, and can be obtained from equation (25). The V

numbers (23) provide information about the waveguide structure, e.g. the core height h as well as λ , and are added as black/red vertical bars in both plots of Figure 23. The value δ describes the degree of asymmetry of the waveguide structure and ranges from zero ($n_2 = n_3$) towards very strong asymmetry ($n_2 \gg n_3$). Moreover, the intersection points between the TE_m/TM_m dispersion lines (black solid/dashed lines) and a certain V number represent b values at the vertical axis. Here, a stronger modal guidance is demonstrated by higher b values, e.g. for TE_0/TM_0 in comparison to TE_1/TM_1 . In general, TE modes are better guided than TM modes due to the E/H field distribution in the core as already demonstrated in Table 1. Once again, very different numbers lead to higher polarization dependence. Anyhow, the TE/TM dispersion curves in both diagrams follow the same run, because of slightly different δ parameters due to the Δn . In addition, the b values and the normalized cut-off frequencies V_m^c (within the green circle) are in good agreement with the calculated values in formula (29)/(30) and are summarized in Table 5.

Table 5: V numbers, b values and critical heights h_{\max} for the two lowest-order modes in an asymmetrical waveguide at 1550 nm due to the core height h

$\lambda = 1550 \text{ nm}$	Asym. waveguide							
$h \text{ (}\mu\text{m)}$	1				0.5			
polarization	TE_0	TM_0	TE_1	TM_1	TE_0	TM_0	TE_1	TM_1
b	0.807	0.739	0.264	0.104	0.536	0.302	"c-o"	"c-o"
V_m	0.684	1.267	3.841	4.431	0.684	1.267	3.841	4.431
$h_{\max} \text{ (nm)}$ for $\lambda = 1550 \text{ nm}$	TE: 720.3 TM: 829.2							
$h_{\max} \text{ (nm)}$ for $\lambda = 541 \text{ nm}$	TE: 244.3 TM: 282.0							

The most important information which appears from the table and the diagrams above is the maximum number of guided modes according to a certain V number. In the case of 1550 nm and a core height of 1 μm , the waveguide supports 4 modes, this means two TE and two TM modes. However, in a 0.5 μm thin core layer only two modes can be found (TE_0/TM_0), thus higher ones are cut-off ("c-o"). That matches the calculated values for the critical height h_{\max} at 1550 nm, whereby h should be less or equal than 720.3 nm to enable SM (TE_0) propagation. In contrast, Figure 23 (b) illustrates, the shorter the wavelength (541 nm), the thinner the core height. Even if the core layer is reduced to 0.5 μm , the waveguide still supports 3 TE and 3 TM modes. As indicated in Table 5, the height has to be less than 244.3 nm for SM (TE_0) operation at 541 nm. However, in short, SM operation requires for both excitation wavelengths core heights thinner than 1 μm . A potential SM waveguide at 1550 nm becomes possible by focusing on a waveguide core of 0.5 μm . Moreover, Si-based photonic structures show typically low attenuation losses (low-loss "window") at 1550 nm, thus the focus of interest is on this specific operation wavelength [91].

A less complex but more accurate alternative for figuring out the number of propagating modes and their optical values was done with the help of a modified MATLAB code (chapter 9, [131]) by solving the TE/TM dispersion relations due to the Δn , polarization, core height h and wavelength. Figure 24 (a – d) shows plots of n_{eff} versus λ for both polarizations according to the core layer thickness of $h = 1, 0.5 \mu\text{m}$. The used RIs of the layers were measured by ellipsometry and are summarized in chapter 7.

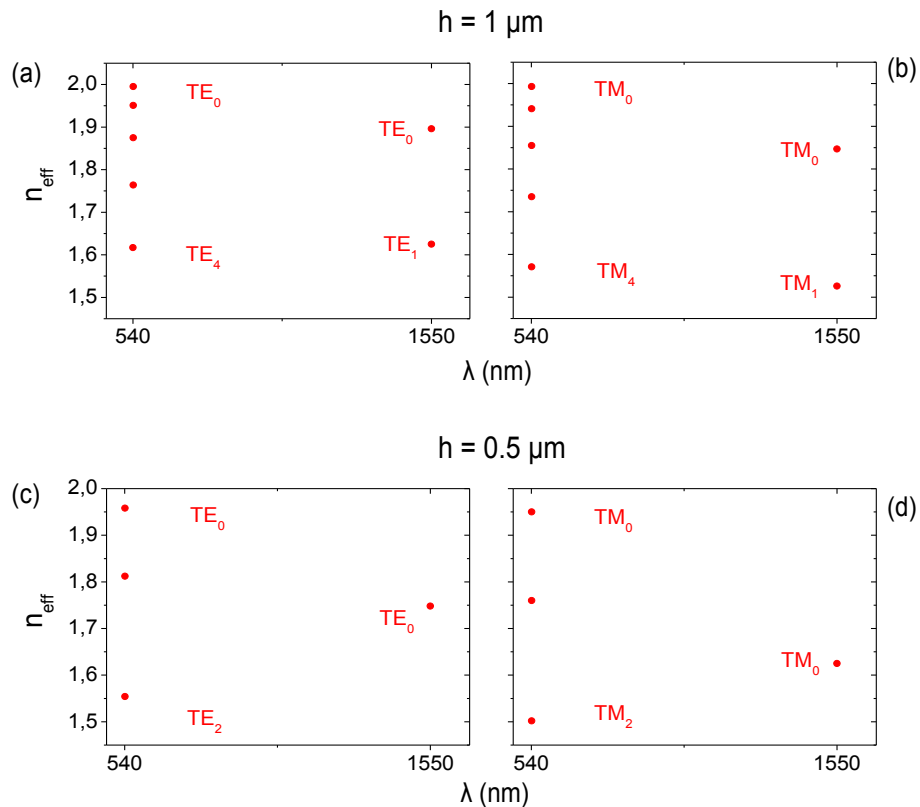


Figure 24: Calculated n_{eff} values of the TE (a, c) and TM (b, d) modes for 1550 nm and 541 nm due to the core heights of $h = 1, 0.5 \mu\text{m}$

These graphs clearly illustrate the maximum number of guided modes in an asymmetrical planar waveguide. At 1550 nm a $1 \mu\text{m}$ thick core layer supports two TE (a) and two TM (b) modes, while a $0.5 \mu\text{m}$ thin waveguide (c, d) only supports the fundamental TE_0/TM_0 modes which agrees with the results in Figure 23 and Table 5. The number of modes in a $1 \mu\text{m}$ or $0.5 \mu\text{m}$ waveguide operating at 541 nm also fits very well, because a thinner waveguide core reduces the number of modes from 10 (a, b) to 6 (c, d). Furthermore, the obtained values of n_{eff} for 1550 nm from Figure 24, Table 1 and Table 2 are comparatively summarized in Table 6.

Table 6: ERIs of the first low-order modes in an asymmetrical waveguide at 1550nm due to the core layer thickness h (1, $0.5 \mu\text{m}$)

$\lambda = 1550 \text{ nm}$	Asym. waveguide							
h (μm)	1				0.5			
polarization	TE_0	TM_0	TE_1	TM_1	TE_0	TM_0	TE_1	TM_1
n_{eff} (Figure 24)	1.896	1.847	1.625	1.526	1.748	1.625	"c-o"	"c-o"
n_{eff} (Table 1/2)	1.883	1.853	1.618	1.535	1.756	1.637	"c-o"	"c-o"

Both methods based on different techniques, graphical or analytical, and displayed good agreement for all the above shown values. Anyhow, the graphical method is more complex, time-consuming and is less significant in comparison to the analytical calculated solutions by

using a simple MATLAB code. Thus, the latter method allows quite fast and precise analysis of the important optical parameters of different one-dimensional waveguide structures.

Chapter 2.4 has already described what a role losses play for integrated photonic devices. Therefore, the scattering losses α_s (65) for the lowest-order TE/TM modes in planar asymmetrical waveguides based on Si_3N_4 cores with air as upper-cladding (n_3) at $\lambda = 1550$ nm due to the core height h were calculated basing on Tien's model [83] and are shown in Figure 25 (a, b).

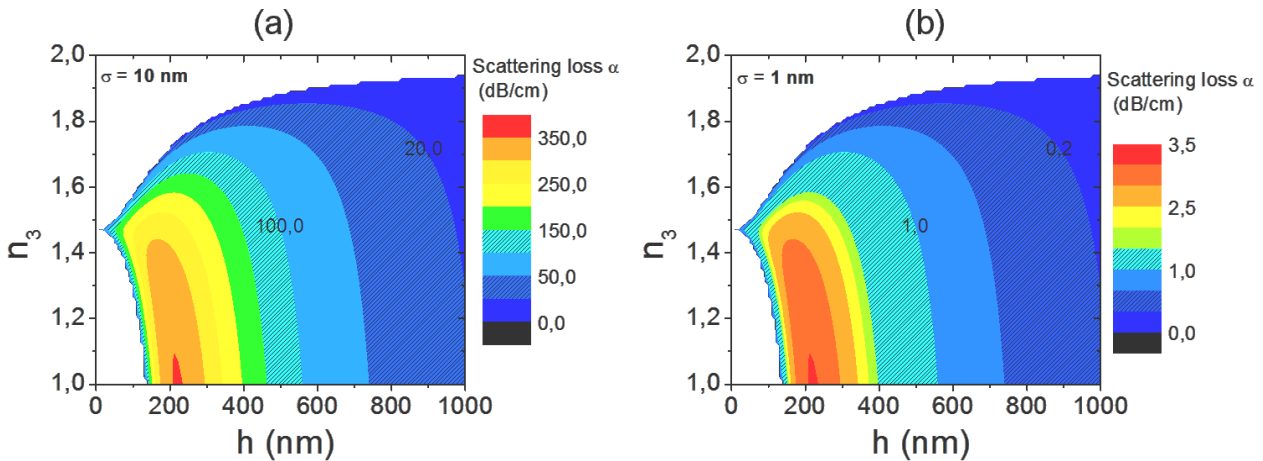


Figure 25: Variations of the scattering losses α_s for lowest-order TE modes at $\lambda = 1550$ nm due to the core height h and the rms values $\sigma_{wl} = 10$ nm (a), 1 nm (b)

For both plots represented above rms values of $\sigma_{wl} = 10$ nm (a) and 1 nm (b) were assumed. The shown variations of α_s correspond to the fundamental TE mode of a Si_3N_4 core with a thickness up to 1 μm . The shown theoretically results can be applied to the TM modes as well regarding similar propagation angles. Anyhow, for both roughness values the losses decrease with increasing RI of the upper-cladding (n_3) resulting in smaller refractive index differences. Unfortunately, it is quite difficult to achieve low propagation losses for high index core waveguides, because the scattering losses increase as $(\Delta n)^2$ [132]. The core heights of interest are $h = 1, 0.5$ μm (hatched areas) showing α_s values of 26.8 dB/cm and 126.1 dB/cm, respectively. It follows, that thicker core layers prevent greater losses due the reciprocal of equation (65). In comparison, waveguides with 10 times less rms values ($\sigma_{wl} = 1$ nm) lead to losses for the fundamental modes of $\alpha_s = 0.26$ dB/cm and 1.26 dB/cm. Thus, interface roughness σ_{wl} decreased by 10 lead to 100 times lower loss parameters. In summary, thinner core layers have 4.8 times higher scattering losses which can be reduced by the usage of an additional upper-cladding, e.g. SiO_2 ($n_3 = 1.47$). Therefore, of central importance in this regard is the used fabrication technology. Melchiorri et. al [133] detected propagation losses of SiO_2 embedded 250 nm thin Si_3N_4 waveguides at 1544 nm of about 4.5 dB/cm, showing that the use of LPCVD reduces the roughness and consequently the related scattering losses. Also, Mao et. al [134] studied the impact of SiH_4/N_2 gas flow ratio and radio frequency power on the hydrogen content in the SiN films. They investigated for a waveguide core of 400 nm losses of 2.1 dB/cm. Kageyama et. al [135] improved their vapor deposition by reducing the concentration of carbon impurities in the Si_3N_4 films and developed the lowest transmission loss of 0.1 dB/cm at 1550 nm in wavelength. Thus, it can be concluded that an optimized fabrication process decisively decreases the interface roughness and influences the propagation characteristic of photonic structures.

However, two-dimensional theoretical investigations like mode profile simulations by FEM or approximated calculations for the n_{eff} by ERIM of different photonic structures are far more important, but considerably more complex. At first we are concentrating on the latter method. Here, we need to remember that the light is confined in two directions. The E-field of the quasi-TE modes is mainly in the x-direction (parallel to the surface) and y-direction (vertical) for that of the quasi-TM modes. However, Figure 26 shows via MATLAB (chapter 9) calculated n_{eff} values of the lowest-order TE- and TM-like modes for $h = 0.5 \mu\text{m}$ at $\lambda = 1550 \text{ nm}$ due to the core width w . The wavelength dependence of the used RI of the Si_3N_4 (n_1) and SiO_2 (n_2) layer was measured by ellipsometry and can be found in chapter 7.

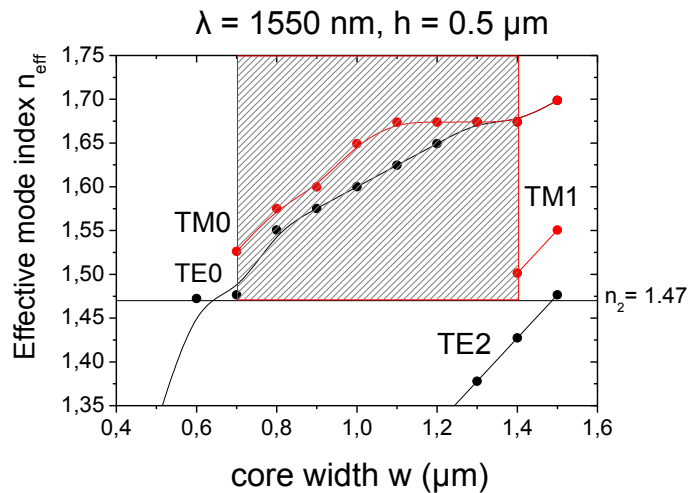


Figure 26: ERIs of the quasi-TE and TM modes for Si_3N_4 waveguides with air cladding, a SiO_2 substrate and a core height of $h = 0.5 \mu\text{m}$ for 1550 nm as function of the core width w from $0.5 \mu\text{m}$ to $1.5 \mu\text{m}$

The obtained calculated results for an operation wavelength of 1550 nm in Figure 26 indicate that (1) increasing the core width w leads to higher n_{eff} values and thus better confined modes, (2) a SM regime of the waveguide for core widths of $0.7 \mu\text{m} < w_{\text{SM}} < 1.4 \mu\text{m}$ (shaded area) can be identified. Here, the first-order quasi-TM mode (TM1) is cut off and only the fundamental TE (TE0) and TM (TM0) modes are guided [34, 35]. Propagation with effective indices smaller than the lowest refractive index of the structure ($n_{\text{SiO}_2} = 1.47$) results in leaky modes, e.g. TE1 and TE2 propagate in the substrate. Additionally, at an extremely low width ($w < 700 \text{ nm}$) both zero-order modes disappear and the waveguide is cut off. Moreover, at $w > 1.3 \mu\text{m}$ almost equal optical values (“anticrossings” of the dispersion lines) for the TE0 and TM0 modes arise leading to mode hybridization and mode conversion due to the increasing asymmetry of the cross-section, which is typical for small-sized high- Δn optical waveguides [78]. Mostly, such a mode conversion is not desired, because it eliminates the polarization dependence resulting in less propagation losses [34, 35, 82], but also introduces excess loss as well as crosstalk (mode dispersion) [78]. In contrast, polarization dependence results in a polarization beating effect between TE and TM modes, thus confusing the polarization which should be controlled externally in order to assure the propagation of one of the modes [136]. In addition, the plot indicates that (3) the n_{eff} values of the quasi-TM modes are larger than these of the same-order quasi-TE modes. This fact is originated by a higher Δn and thus waveguiding in the y-direction across the width (Figure 17 (c), $n_3 = 1$). Furthermore, the estimated SM operation regime is quiet inaccurate due to the obtained ERIs of not-well confined modes near their cutoffs. In conclusion, the errors of the ERIM are basically connected with equations (19) and (20) as well as the waveguide structure and Δn . Nevertheless, the method serve as a starting point for further analysis methods like FEM which are used to make more accurate statements about n_{eff}

values and an optimized SM design. The method can be also applied for $\lambda = 541$ nm, but as already illustrated in Figure 24 (c, d) SM guidance is excluded for the selected core height.

However, for first statements about possible designs of the photonic structures and the optical values the used methods are simple and fast techniques. Unfortunately, they are inaccurate concerning detailed analysis of the mode confinement and the mode profiles according to two-dimensional waveguide cores. The finite element method (FEM) is based on an eigenmode solver which calculates the spatial profile and frequency dependence of modes by solving Maxwell's equations on a cross-sectional mesh of the waveguide. COMSOL and FlexPDE have been used in this work, because they are perfect FEM tools to obtain the ERI values and mode profiles of the waveguide modes and lead to optimized designed photonic devices due to the operation frequency. The error sources are the lack of inadequate knowledge of correct boundary conditions, material properties and geometry. It is important to know, which problem will be explored and what kind of boundary conditions are limiting the solution.

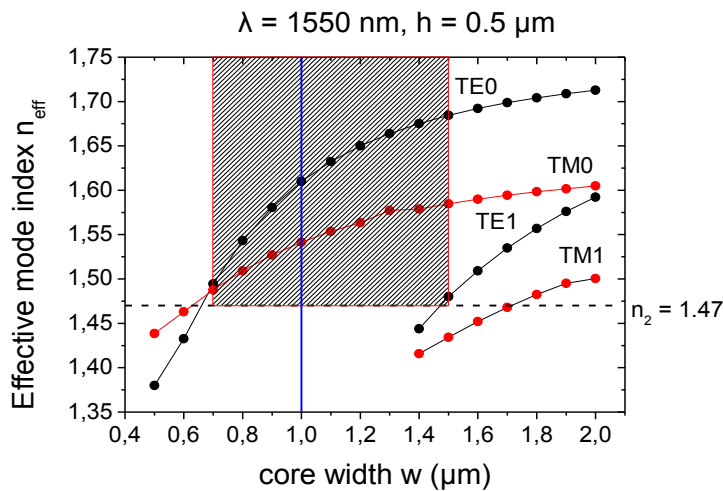


Figure 27: Calculated ERIs of the quasi-TE and TM modes for Si_3N_4 waveguides with air cladding, a SiO_2 substrate and a core height of $h = 0.5 \mu\text{m}$ at 1550 nm as function of the core width $0.5 \mu\text{m} \leq w \leq 2 \mu\text{m}$

The following facts can be seen from the picture above, (1) increasing the core width w results in higher n_{eff} values and thus better confined modes, (2) a SM regime of the waveguide for core widths of $0.7 \mu\text{m} \leq w_{\text{SM}} \leq 1.5 \mu\text{m}$ (shaded area) can be identified. In comparison to Figure 26, the obtained SM regimes match well with the exception of the n_{eff} values near the cut-off frequencies. In addition, the plot indicates that (3) ERIs all quasi-TE modes are larger than these of the same-order quasi-TM modes. This fact is in contradiction with the results of the above used method. As already mentioned, the ERIM produces only correct values if the specified conditions have been met. Thus, the values calculated by FEM can be designated as trusted so that they can be seen as a good approximation. Moreover, a SM waveguide based on a cross-section of $h = 0.5 \mu\text{m}$ and $w = 1 \mu\text{m}$ (blue line) has been chosen for further observations in respect of an optimized SM design. The obtained optical parameters from the study above can be used to have a closer look at the propagation constants β (16) and the modal confinement factors Γ^{mode} (43) which are summarized in Table 7.

Table 7: Optical parameters n_{eff} , β and Γ_{mode} for a cross-section of $0.5 \times 1 \mu\text{m}^2$ at 1550 nm

Mode	n_{eff}	β (rad/ μm)	Γ^{mode} (%)
TE ₀	1.61	6.53	87.2
TM ₀	1.54	6.24	86.3

The fundamental TE-like mode shows a slightly better confinement in the waveguide core in comparison to the same-order TM mode which is originated by a higher n_{eff} (or β) value. In conclusion, the designed SM waveguide and the associated optical values will be used in the following chapters for the development of high-aspect-ratio photonic structures as bends [137], tapers and finally optimized butt-coupled LEDs.

Beside calculations of geometry-dependent ERIs the FEM can be used to visualize mode profiles. Fixed boundary conditions as PEC (perfect electric conductor) or the direction of propagation for the traveling wave determine the numerical solutions of the Helmholtz equations ((36), (37)). As illustrated in Figure 28 (a, b), the cross-section of the waveguide is $0.5 \times 1 \mu\text{m}^2$ and the light is traveling with a frequency of $f = 1.935\text{E}14$ Hz ($\lambda = 1550$ nm) perpendicular to the plane.

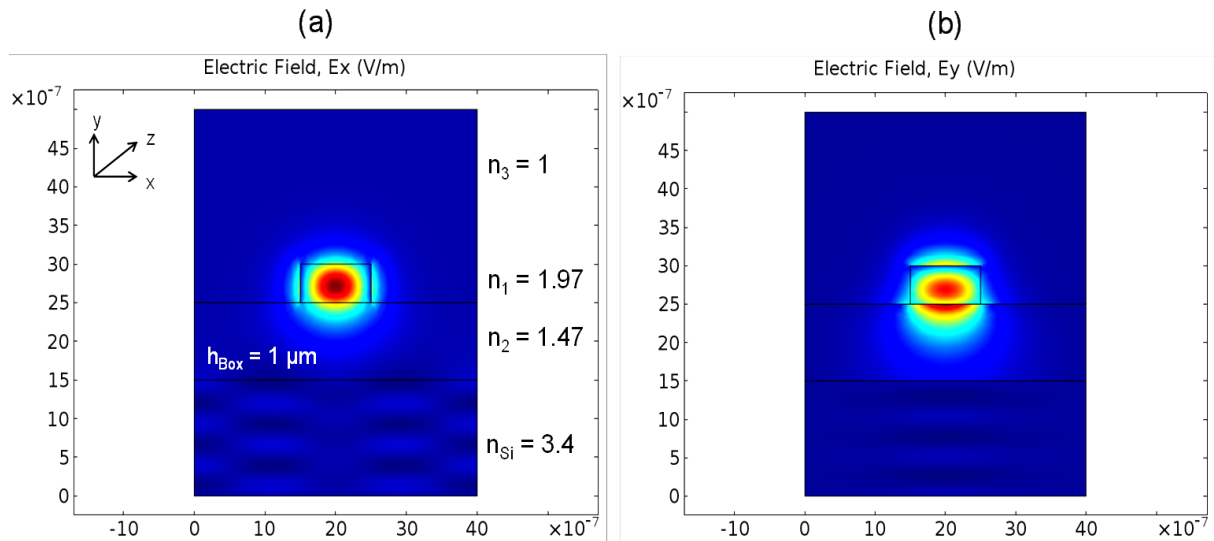


Figure 28: Obtained mode profiles for $0.5 \times 1 \mu\text{m}^2$ Si_3N_4 -waveguides at 1550 nm by COMSOL, (a) E_x component of the TE₀ mode, (b) E_y component of the TM₀ mode

The chosen waveguide geometry in Figure 28 (a, b) is based on an asymmetric waveguide with a significant $1 \mu\text{m}$ thick box layer made of SiO_2 (h_{Box}). All used wavelength depended RI of the layers are measured and summarized in chapter 7. The obtained field profiles of the TE₀ (a) and TM₀ (b) mode clearly show that the fundamental TE mode is characterized by much higher field intensity at the side walls, whilst the TM mode has much higher amplitude at the top and bottom interface [34]. Therefore, TM₀-based waveguides are particularly more suited for field interactions with deposited and bonded materials at the surface for biosensing applications [16, 21, 138, 139].

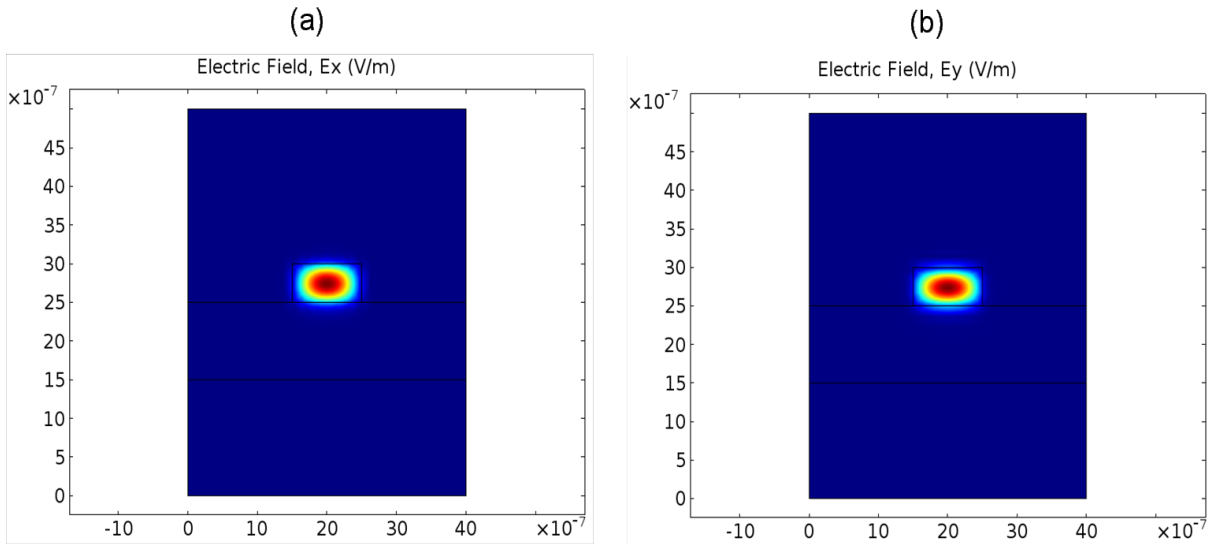


Figure 29: Obtained mode profiles $0.5 \times 1 \mu\text{m}^2$ Si_3N_4 -waveguides at 541 nm by COMSOL, (a) TE0 and (b) TM0 mode

For the sake of completeness, it is pointed out that, Figure 29 (a, b) presents the mode profiles of the fundamental TE and TM modes at $f = 5.54\text{E}14$ Hz ($\lambda = 541$ nm). In comparison to Figure 28 (a, b), the fields are essentially concentrated in the core and characterized by higher n_{eff} values ($n_{\text{eff}}(\text{TE0}) = 1.94$, $n_{\text{eff}}(\text{TM0}) = 1.93$).

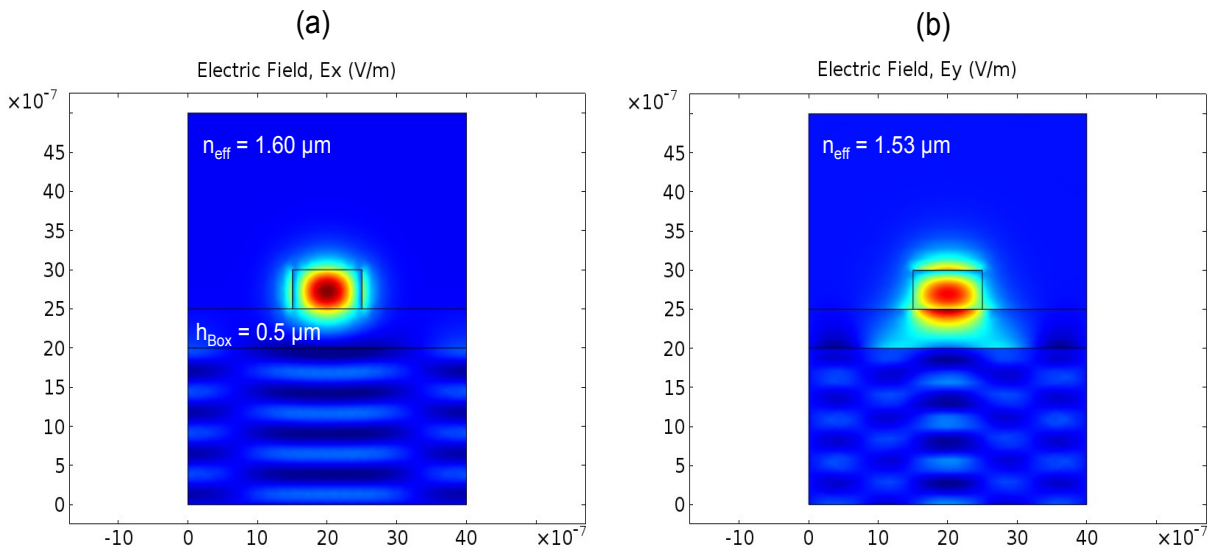


Figure 30: Influence of the box layer thickness on the mode profiles of the TE0 (a) and TM0 (b) mode for a $0.5 \mu\text{m}$ thick box layer at 1550 nm

Moreover and as already mentioned in chapter 2.4, the thickness of the lower SiO_2 cladding (h_{Box}) determines the amount of leakage power into the Si substrate [35]. Figure 30 (a, b) shows the mode profiles of the TE0 and TM0 modes for a waveguide core with a $0.5 \mu\text{m}$ thin SiO_2 box layer at $\lambda = 1550$ nm. In contrast to Figure 28 (a, b), both pictures underline, a box layer thinner than $1 \mu\text{m}$ causes in greater field concentrations, less n_{eff} values resulting in higher power leakage into the Si substrate. In short, the thickness of the SiO_2 lower cladding should be at least $1 \mu\text{m}$ to avoid significant substrate radiation. Additionally, this fact is important regarding

the coupling between the Si-based LED and the waveguide and will be further analyzed in a later paragraph of this section (4.1.2.3).

Also note that the substrate leakage loss is decreased rapidly in high-aspect-ratio waveguides [35, 140]. Thus, Figure 31 illustrates enhanced modal confinement of the TE₀ mode in a waveguide with increased core width ($w = 10 \mu\text{m}$). As an undesirable result, greater waveguide cores support higher-order modes, because of lower cut-off frequencies V_m^c . Moreover, the polarization dependence is increased leading to modal dispersion and higher propagation losses of the TE₀ mode [141]. Nevertheless, this geometry factor especially implies photonic device butt-coupled Si-based LEDs. The knowledge regarding the geometry influenced field distribution plays an important role for the connection between different sized optical, e.g. MM and SM waveguides, and electrical devices as the light emitters.

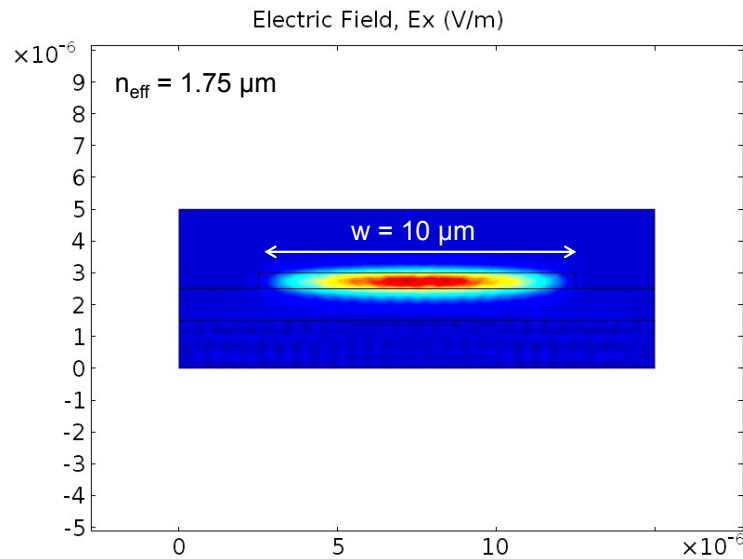


Figure 31: Mode profile of the TE₀ mode ($n_{\text{eff}} = 1.75$) for a core of $0.5 \times 10 \mu\text{m}^2$ at $\lambda = 1550 \text{ nm}$

However, the most frequently encountered deviations from the rectangular geometry are cross-sections with shapes that can be approximated by trapezoidal profiles with reasonable accuracy [51, 52]. Such deviations occur mainly due to the various types of processes involved in the fabrication of the photonic structures (e.g. lithography and RIE) as happened in our case and illustrated in chapter 7. Therefore, we used a simple geometrical method which was first developed by Clark and Dunlop [52] for the construction of the equivalent rectangular waveguides corresponding to a given trapezoidal geometry. They showed numerically that it is possible to construct for any given trapezoidal waveguide, an equivalent rectangular waveguide that has to the first order of perturbation the same propagation constant as the original trapezoidal waveguide. The equivalent rectangular waveguide has the same thickness as the trapezoidal structure, and its width can be determined from the condition that the first-order correction to the propagation constant vanishes [51, 52]. The width w_{ER} of the equivalent rectangular waveguide corresponding to a trapezoidal waveguide with the small base w_{TR} and the large base L_{TR} will be given by the expression [51]

$$w_{\text{ER}} = \frac{w_{\text{TR}} + L_{\text{TR}}}{2}. \quad (74)$$

In our case, based on the structural investigations by AFM and REM in chapter 6 and 7, the original (w_0), measured (w_{TR} , L_{TR}) and estimated (w_{ER}) core widths as well as the side wall slope angle α and the obtained n_{eff} values for a $0.5 \mu\text{m}$ thick waveguide are summarized in Table 8.

Table 8: Overview of the original rectangular waveguide width w_0 , the measured trapezoidal small base width (w_{TR}), the large base (L_{TR}), the estimated width w_{ER} for a $0.5 \mu\text{m}$ thick waveguide core, the side wall slope angle α and the n_{eff} values of the zero-order modes in the trapezoidal and equivalent rectangular waveguide

w_0 (μm)	w_{TR} (μm)	L_{TR} (μm)	w_{ER} (μm)	α ($^\circ$)	Trapeze $n_{\text{eff}}^{\text{TE0}}$	Trapeze $n_{\text{eff}}^{\text{TM0}}$	Eq. Rec. $n_{\text{eff}}^{\text{TE0}}$	Eq. Rec. $n_{\text{eff}}^{\text{TM0}}$
1	1.2	1.4	1.3	78.6	1.66	1.57	1.66	1.57

As can be seen from the listed core widths w_x in Table 8, the fabricated and estimated waveguides differ from the original rectangular shaped geometry. However, Figure 32 (a, b) shows, that the obtained mode profiles and n_{eff} values for $\lambda = 1550 \text{ nm}$ of the TE0 and TM0 modes in a trapezoidal geometry only slightly vary from the planned structure in Figure 28 ($n_{\text{eff}}^{\text{TE0}} = 1.61$, $n_{\text{eff}}^{\text{TM0}} = 1.54$).

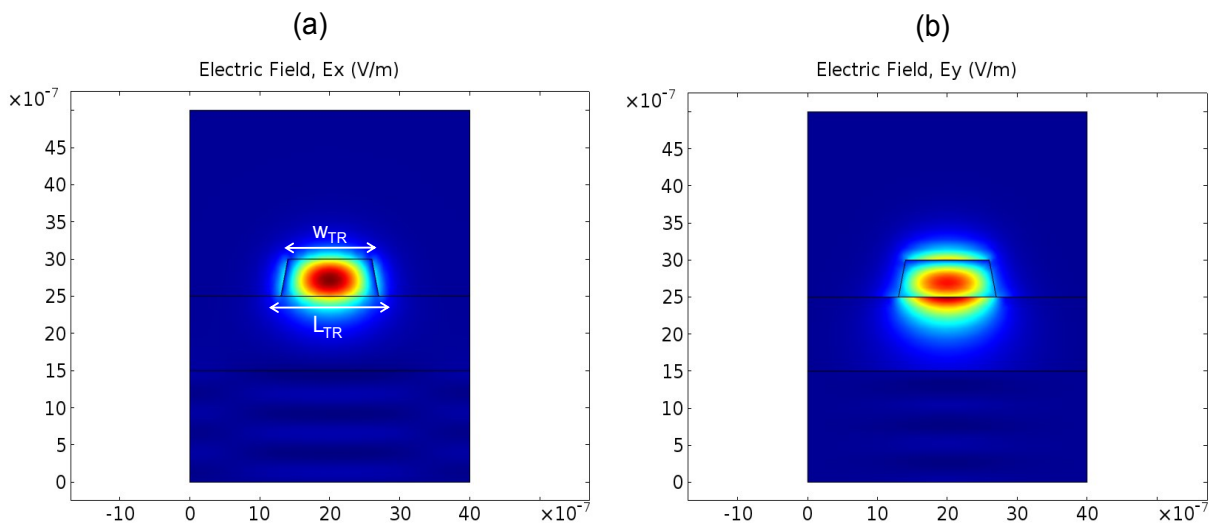


Figure 32: Obtained mode profiles for trapezoidal waveguides ($w_{TR} = 1.2 \mu\text{m}$, $L_{TR} = 1.4 \mu\text{m}$, $h = 0.5 \mu\text{m}$), (a) TE0 ($n_{\text{eff}} = 1.66$) and (b) TM0 mode ($n_{\text{eff}} = 1.57$)

Moreover, Figure 33 (a, b) and Table 8 clearly illustrate, that the obtained ERIs of the estimated rectangular structures are practically identical with those of the trapezoidal waveguides. Thus, using the approach in formula (74), it is possible to achieve a good approximation for the theoretical rectangular waveguide. In addition, the geometry of the estimated waveguide still guarantees SM operation, because $w_{ER} \leq 1.5 \mu\text{m}$ (Figure 27).

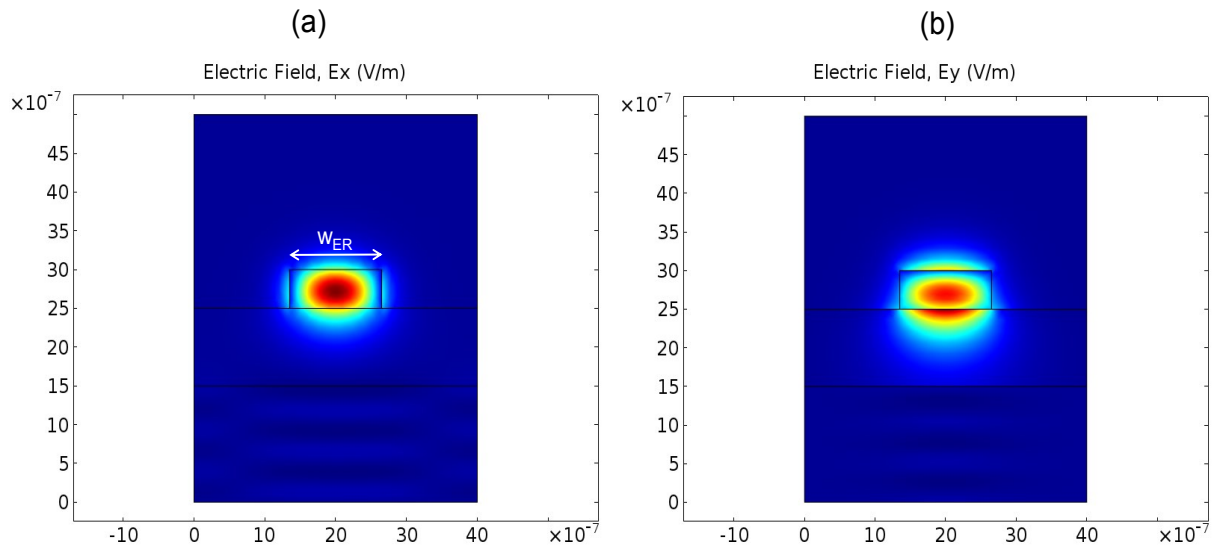


Figure 33: Obtained mode profiles of the estimated rectangular waveguides ($w_{ER} = 1.3 \mu\text{m}$, $h = 0.5 \mu\text{m}$), (a) TE₀ ($n_{\text{eff}} = 1.66$) and (b) TM₀ mode ($n_{\text{eff}} = 1.57$)

In conclusion, fabrication steps as lithography or RIE often lead to slanted side walls of the waveguide core [51, 52, 104]. Unfortunately, the cross-section of the fabricated structures shows clear differences, however, well-tested theoretical methods [51, 52] enable a good approximation of the planned geometry. Therefore, statements about design characteristics, like field distributions or power leakage, are possible. Finally, we can assume that the optical properties of our fabricated SM waveguides (with slanted side walls) correspond with those of the approximated rectangular shaped structures.

In order to build a complete integrated photonic circuit the connection between different arranged optical and electrical devices is made possible through bended waveguides [35]. One important design aspect is how to shape a waveguide to go around a corner without incurring unnecessary losses in signal power and perfect transmission. Especially, high NA materials and strip waveguides with a high-aspect ratio achieve high light confinement and tight bending radii [35, 38, 63]. The disadvantage of these structures is the typical high scattering losses described by a nonlinear function of the bend radii [54]. Nevertheless, FEM simulations allow statements about bending loss interpretations by field distributions and scattering parameters (S-parameter) near the curvature. Investigations of the transmission and reflection behavior in the range of $1.87\text{E}14 \text{ Hz} \leq f \leq 2.01\text{E}14 \text{ Hz}$ ($1490 \text{ nm} \leq \lambda \leq 1550 \text{ nm}$) of the fundamental TE mode for different bending radii were carried out. Again, specified boundary conditions, the mesh size as well as the geometric structure determine the correctness of the solution.

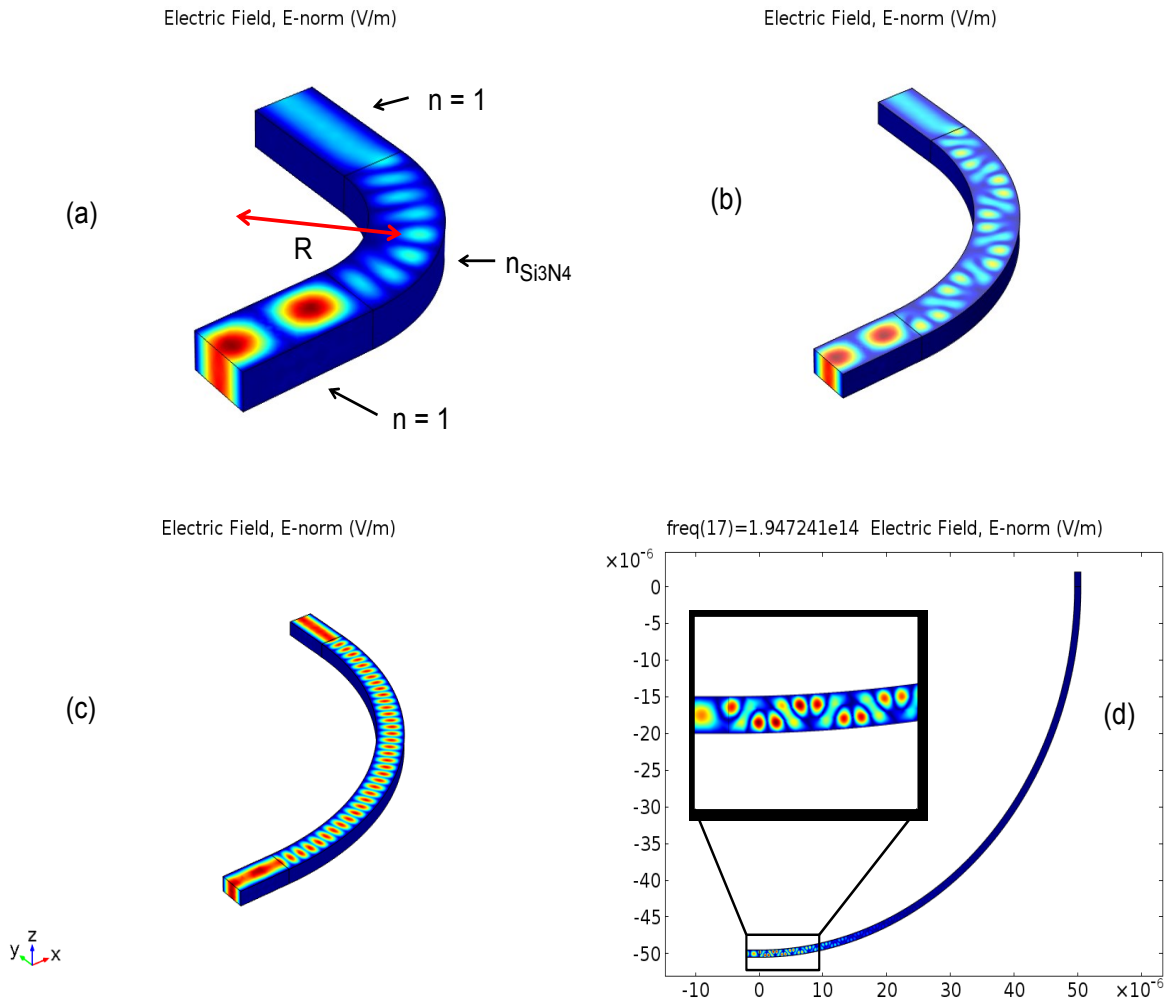


Figure 34: Fundamental mode profiles of curved waveguides with different bend radii at $f = 1.947E14$ Hz, (a) $R = 2 \mu\text{m}$, (b) $R = 5 \mu\text{m}$, (c) $R = 10 \mu\text{m}$, (d) $R = 50 \mu\text{m}$

As depicted above, a 90° bend waveguide is based on a cross-section of $h = 0.5 \mu\text{m}$ and $w = 1 \mu\text{m}$ and is investigated in dependence of the curvature radius R . In this model, to make the impact of the bend radius more clear, the waveguide geometry consists of two air filled straight waveguides working as the in- and out output ports and a Si_3N_4 filled bend. The waveguide walls are considered to be made of a perfect conductor (PEC), which means that the tangential component of the electric field is zero on the boundaries (69) except the two ports at the left and upper right end of the waveguide. Here, an important design aspect is to guide the light “around the corner” without incurring unnecessary losses in signal power. Besides the E-field distribution, S-parameters are used to give a quantitative measure of how much of the wave is transmitted and reflected at different frequencies. Figure 34 (a –d) illustrates the mode profile of the fundamental TE mode for waveguide bends with $R = 2, 5, 10, 50 \mu\text{m}$. The scattering in the bend can be minimize by keeping the bend smooth with a radius larger than $5 \mu\text{m}$, but less than $50 \mu\text{m}$ for the chosen frequency range. Figure 34 (c) shows for $R = 10 \mu\text{m}$, that in the range of operation the transmission characteristics is reasonably uniform and signal distortions can be avoided. The calculated results are in good agreement with the theoretical values, whereby high optical devices may have bending radii on the order of $10 \mu\text{m}$ [35]. Moreover, note the field distribution in the bend and the rectangular input and output sections. The latter indicate that the absence of a wave pattern results in a nearly perfect transmission, in comparison to Figure 34 (a, b, d). Here, standing waves in the input section caused by

reflections in the bend lead to scattering losses. Additionally, the light wave propagates in the direction of the bend with a different electromagnetic field distribution in comparison to that in the straight part. It is well established that the mode of the straight waveguide is not exactly matched to the mode of the bent waveguide and that this mismatch introduces additional loss [101], which is not taken into account here.

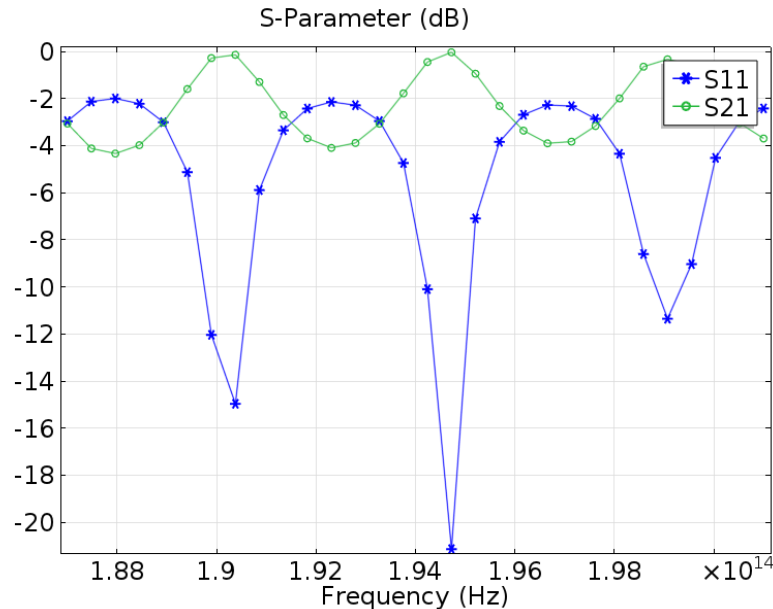


Figure 35: S-parameters plot (dB) as functions of the frequency for $R = 10 \mu\text{m}$; transmitted (S_{21}) and reflected (S_{11}) power

Anyhow, the obtained S-parameters (S_{11} , S_{21}) for $R = 10 \mu\text{m}$ due to the frequency are plotted in Figure 35. The S-parameters are complex (magnitude and angle) and refer to the scattering matrix which is a mathematical construct that quantifies how energy is transmitted (S_{21}) and reflected (S_{11}) during light propagation through an optical system. In general, the main focus is only on the magnitude for a given frequency to define the gain or loss of the device. The dips in S_{11} (blue) closely correspond to the reflectance (cavity resonances) of the dielectric region in the bend. The S_{21} parameter corresponding to the transmittance is given by the green curve. In conclusion, a reflection minimum ($S_{11} = -22 \text{ dB}$) at $f = 1.947\text{E}14 \text{ Hz}$ of the bend was obtained resulting in almost perfect transmission of the signal. In reality, bend-loss measurements are required to identify optimized light guiding due to input signal and the waveguide curvature.

4.1.2.2 Tapered Waveguides and Photonic Crystals

An optical interconnect access for transferring light between two different sized optical devices is realized through tapered waveguides allowing maximum energy transfer [73, 74, 75, 76, 77, 142]. In contrast to the generation of mode conversion in SOI nanowires [73, 76], light coupling to a SM strip waveguide requires an adiabatic tapered section which filters out higher-order modes. One design rule is usually to make the tapered section (L_T) long enough [73, 78], especially if the width ratio between the optical devices is large as in the case of a SM waveguide ($w = 1 \mu\text{m}$) and the Si-based LED ($w = 300 \mu\text{m}$). Additionally, the taper angle (θ_T) should not be too small in the smaller-area waveguide, thus scattering and insertion losses don't get too large.

With regard to the described conditions, Figure 36 (a, b) illustrates firstly linear tapers for the coupling between two waveguides with varying widths ($w_1 = 2 \mu\text{m}$, $w_2 = 1 \mu\text{m}$).

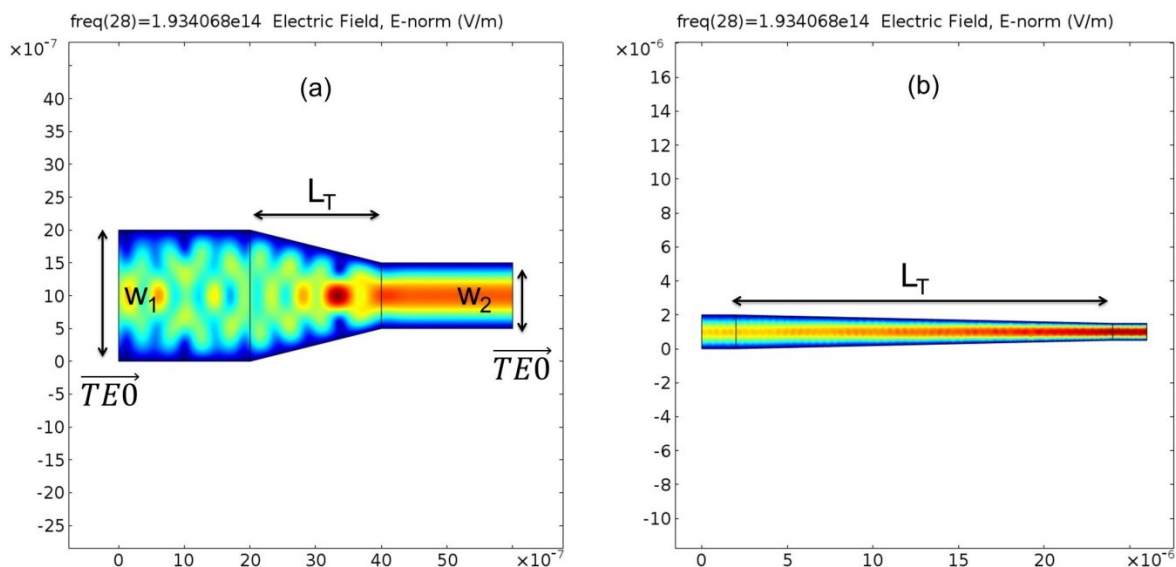


Figure 36: Light propagation in short (non-adiabatic) and long (adiabatic) Si_3N_4 tapers for coupling of the fundamental TE mode between waveguides with $w_1 = 2 \mu\text{m}$ and $w_2 = 1 \mu\text{m}$, (a) short taper $L = 2 \mu\text{m}$, (b) long taper $L_T = 20 \mu\text{m}$ at 1.934×10^{14} Hz

Figure 36 (a, b) depicts the norm of the E-field (amplitude) along a designed non-adiabatic (a) and an adiabatic taper (b). The launched field is chosen as the TE₀ mode at an operation frequency equal to the frequency of an Er:LED ($f = 1.935 \times 10^{14}$ Hz, $\lambda = 1550$ nm) and a waveguide width ratio of 2:1. As a result, ripples (a) appear in the input waveguide and the tapered section indicating multimode-interference effect caused by the excitation of higher modes in the wider waveguide [78]. Also scattering and insertion losses generate a wave pattern in the launched waveguide, when the taper length is too short. Nevertheless, only the fundamental TE mode is transmitted to the smaller-sized waveguide confirmed by the absence of a wave pattern in the output section. In particular, the taper should be long enough in order to radiate higher-order modes away [73, 78]. In contrast, Figure 36 (b) illustrates the transmission characteristic by using a 10-times longer taper. Here, the complete field pattern shows nothing conspicuous confirming that the taper does a good job of transmitting a single mode to the output waveguide.

Moreover, the use of low-loss tapers is not only necessary for the light propagation between different sized waveguides, also the coupling of high-aspect-ratio waveguides with optical fibers, semiconductor lasers, and photodetectors at high frequencies show large input misalignments, because of the large mode mismatch of mode profiles and the effective index differences. Thus, μm -sized waveguides connected to ultranarrow tips in the submicrometer range are required for direct coupling to external or integrated devices as the Si-based LED.

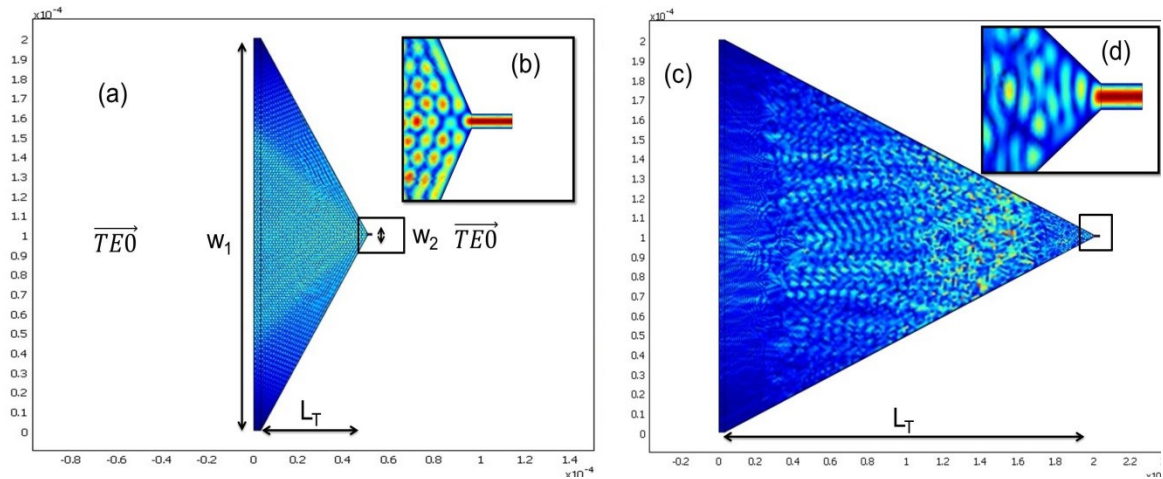


Figure 37: Propagation of the TE₀-like mode at $f = 7.61 \times 10^{13}$ Hz between two waveguides with $w_1 = 200 \mu\text{m}$ and $w_2 = 1 \mu\text{m}$ through a (a, b) short taper ($L_T = 50 \mu\text{m}$) and a long taper ($L_T = 200 \mu\text{m}$ (c, d))

Figure 37 (a - d) illustrates the coupling between two waveguides with a width ratio of 200:1 by tapers with different lengths ($L_T = 50 \mu\text{m}$ (a, b), $200 \mu\text{m}$ (c, d)). Here, the following limitation must be noted: the input frequency equals the cut-off frequency ($f_c^{\text{TE}_0} = 7.61 \times 10^{13}$, $\lambda = 3.94 \mu\text{m}$) of the fundamental TE mode in the small-sized waveguide (w_2). This is necessary, because a lot of higher-order modes are already excited at this operation frequency leading to a mixed up wave pattern due to the wide width of the launched waveguide ($w_1 = 200 \mu\text{m}$). Figure 37 (a, b) shows, that a short tapered section ($L_T = 50 \mu\text{m}$) creates more reflections in the launched waveguide and at the end of the taper, just as in the case of Figure 36 (a). In comparison, an adiabatic taper decreases the proportion of propagating higher-order modes indicated by a more uniform field distribution next to output port. Moreover, the accuracy of the FEM is affected by the design and size of the FE model. The computing time is determined by the finite element size (mesh density) and the usage of proper boundary conditions [94]. According to the FE theory, a FE model with a fine mesh leads to highly accurate results, but takes longer computing time and requires adequate memory [143]. In particular, extended taper structures with a high width ratio strongly increase the FE model complexity. In addition, the model parameters, e.g. scalar variables like the operation frequency, are also relevant for the number of possible solutions. However, in summary, this work focuses on the connection of optical devices with large width ratios for SM operation and is based on the shown theoretical findings. The coupling between Si-based LEDs and SM waveguides (more than 300-times smaller) for operation frequencies in the visible or IR range requires even longer tapers to ensure complete elimination of higher-order modes.

Another important optical device group which affects the propagation of electromagnetic (EM) waves are PhCs. These structures are composed of regularly repeating regions of high and low dielectric constant. Here, the lattice constant \mathbf{a} determines the optical band gap in which the light cannot propagate through the crystal leading to back reflection coupled with attenuation of the total standing wave [57]. The calculation of the complete band gap is significantly difficult considering all crystal directions and polarizations [34]. Moreover, much more interesting are applications based on specific disturbances of the lattice periodicity, e.g. PhC waveguides (line defects). Figure 38 (a, b) shows the calculated light motion influenced by a line defect in 2D PhCs for an operation frequency of a Tb:LED ($f = 5.55 \times 10^{14}$ Hz, $\lambda = 541 \text{ nm}$) (a) and an Er:LED ($f = 1.935 \times 10^{14}$ Hz, $\lambda = 1550 \text{ nm}$) (b).

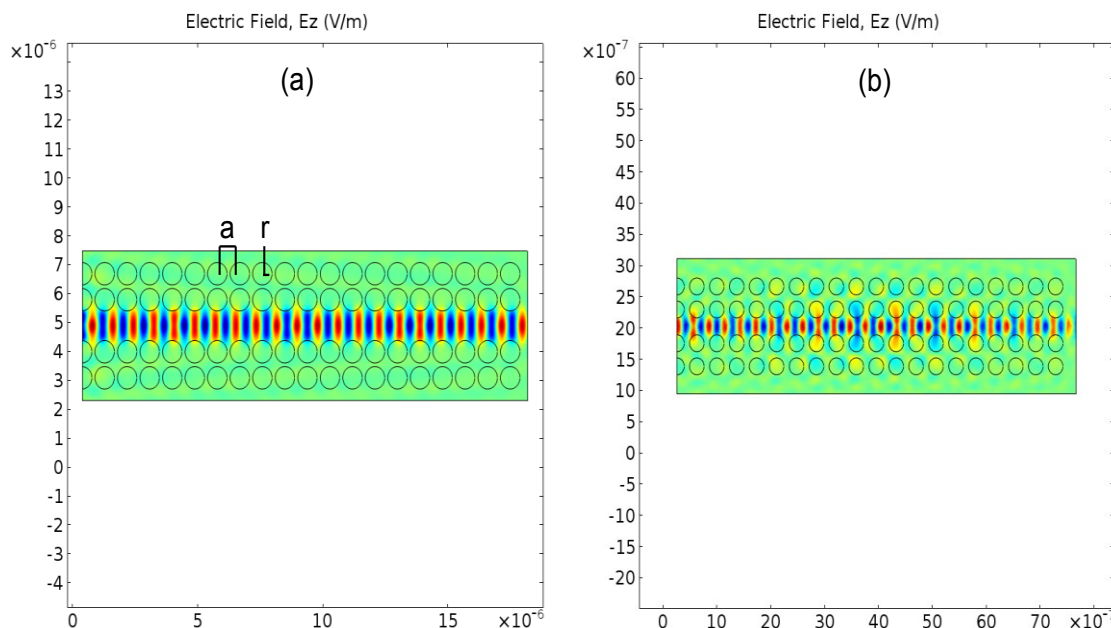


Figure 38: In-plane TE wave propagation in 2D PhC waveguides, (a) $r/a = 0.43$, $f \triangleq \text{Er:LED}$; (b) $r = 0.135 \mu\text{m}$ and $a = 0.370 \mu\text{m}$ at $f \triangleq \text{Tb:LED}$

The PhC waveguides shown above are composed of low RI holes (Air) etched in a high RI material (Si_3N_4) with a line defect. The line defect breaks down the crystal symmetry and creates a defect band with frequencies in the photonic band gap ($\lambda \sim 2a$). Figure 38 (a) illustrates the in-plane TE wave propagation for an operation frequency of an Er:LED ($f = 1.935\text{E}14 \text{ Hz}$) in PhC with $a = 0.9 \mu\text{m}$ and $r = 0.3875 \mu\text{m}$. It can be seen that the TE wave is perfectly transmitted along the defect, and the E-field decays exponentially into the rest of the crystal. The simulated wave propagation for a higher frequency (visible range) in Figure 38 (b) also confirms the theory [65]. The results obtained can be used for further implementations of PhC devices and their integration in compact photonic circuits for high efficient photonic devices [61, 62, 63, 64]. Unfortunately, the fabrication requires more advanced processing due to the low r/a ratio, for which reason these structures were not further considered in the context of this work.

4.1.2.3 Butt-Coupled Si-based Light Emitters

The results from the theoretical investigations from chapter 4 enable further considerations for an efficient coupling between the Si-based light emitter and an integrated waveguide. The coupling method by “butting” the LED and the (tapered) waveguide close together was already mentioned in Figure 21 (a, b). Moreover, in this study, two different MOS structures were fabricated: (a) a “ SiO_2 ”-LEDs and a (b) “ SiN_x ”-LEDs. Figure 39 (a, b) clarifies again the main difference between both optoelectrical devices and illustrates the butt-coupling directly to an integrated waveguide.

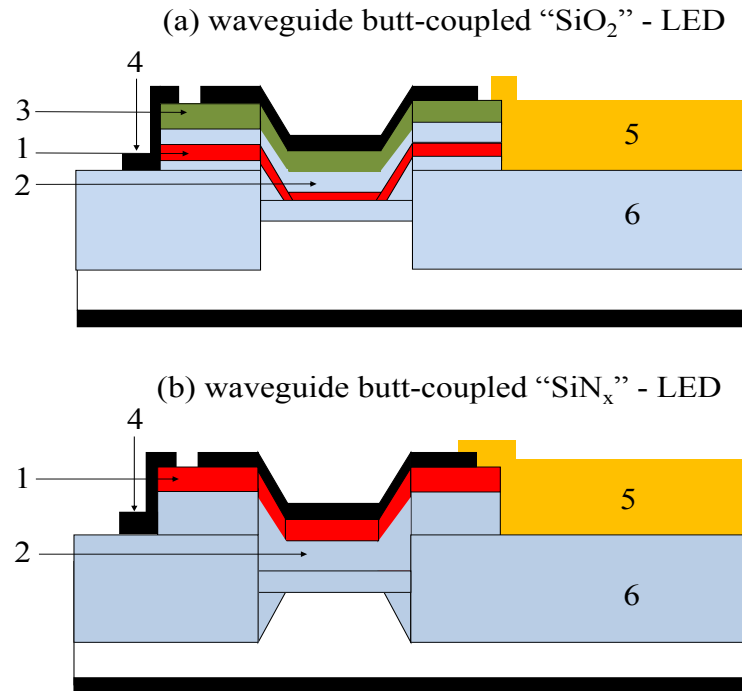


Figure 39 (submitted [144]) : (a, b) Structure of the two LEDs butt-coupled to an integrated waveguide; (1) luminescence layer with the implanted RE atoms, (2) SiO_2 layer system, (3) SiON protection layer, (4) Al-mirror, (5) integrated Si_3N_4 waveguide, (6) SiO_2 box layer; not in scale

From the schematic structures above it can be seen, that in the case of the “ SiO_2 ”-LED (a) the RE atoms are implanted 20 – 50 nm deep into the SiO_2 gate oxide (2) forming a luminescence layer (1). Moreover, a SiON protection layer (3) is used, whereby the “ SiN_x ”-LED (b) is composed only of a SiN_x -based active layer (40 nm) (1) containing the RE atoms directly below the front contact of the LED. However, both structures have an additional Al-mirror (4) limiting the path of light propagation by reflection [144]. Detailed fabrication recipes of the LED and the complete integrated photonic circuit can be found in chapter 5. It should be noted, that the already predefined LED design parameters, i.e. the implantation depth/dose and the layer structure, determined the values for the coupled photonic structures, like the dimensions/position of the guiding layer. Therefore, an optimized system design requires theoretical investigations which were carried out in the former sections of this chapter. Here, the main aspects were high modal confinement, high butt-coupling efficiency and SM/MM operation. Retrospectively, it can be said that SM operation requires an adiabatic tapered waveguide as well as a thinner core thickness (h_{max} , Table 5) and a lower operation frequency (Figure 24, Figure 37). Furthermore, it could be shown that the SiO_2 box layer varies for each mode according to the waveguide dimensions and the frequency, but should be in minimum 1 μm thick avoiding light radiation into the Si substrate (Figure 30). Moreover, a modal confinement factor of the fundamental modes of approximately 87 % can be assumed for Si_3N_4 based waveguides with $0.5 \times 1 \mu\text{m}^2$ cross-sections (Table 7).

However, this part of the chapter focuses on the design parameters of both devices to achieve a high butt-coupling efficiency. Especially, the usage of an efficient integrated light source is important [14, 17]. Here, the Si-based LED serves as the starting application with light emission based on an incoherent process of spontaneous emission [4, 126]. Anyhow, the use of an integrated LED as the light source in a photonic circuit has several advantages. First of all, the fabrication is simple; the costs are affordable and as well as its linearity of the output signal [5]. Furthermore, the device has a high reliability; shows lower driver currents and a reduced temperature dependence [4, 24, 129]. Besides the fabrication of high Δn devices, e.g.

GaAs/AlGaAs LEDs, for applications at shorter wavelengths, the benefit in the telecommunication industry requires low dispersion components for lower signal attenuation and optimized transmission rates [34, 91].

Anyhow, as illustrated in Figure 39 (a, b), the “edge emitter” [71] is either composed of a SiO_2 (a, 1) or SiN_x (b, 1) active layer (n_1), which is sandwiched between two layers of lower RI (n_2). The doping with Er^{3+} or Tb^{3+} ions leads to an increased RI of the embedded layer forming a second guiding dielectric slab waveguide (RI can be found in chapter 7) [34, 71]. Some of the light generated inside the active layer is trapped by the waveguide, while the rest is emitted from the edge of the device [71]. Due to the low RI difference Δn (2), especially in the case of Tb/Er:SiO₂ LEDs, a fairly small fraction of light will be trapped by the generated waveguide resulting in a low output power [35, 71]. Despite this drawback, the angular distribution of the emitted light is narrow ($\cos \theta$ dependence), thus the coupling into an integrated photonic structure will be efficient [71]. Moreover, Quimby [71] interpreted the LED as a Lambertian source with an external power efficiency η_{ext} proportional to the ratio of the total power emitted from the Lambertian source P_0 and the total power emitted inside the active material P_s , as defined in formula (75).

$$\eta_{\text{ext}} = \frac{P_0}{P_s} = \frac{1}{n_1(n_1 + 1)^2} \quad (75)$$

For “SiO₂”- and “SiN_x”-LEDs due to the implanted RE atoms the above equation provides a theoretical external power efficiency between 10 % and 5 %. Additionally, equation (53) describes the coupling efficiency η_c between the waveguide and the LED with respect to the ratio of their areas. Here, we assume that the whole gate oxide in which the active layer is embedded radiates light. The index-contrast of the planar waveguide determines the portion of the guided light. Furthermore, it has to be noted that the integrated waveguide is composed of an asymmetrical layer structure (SiO₂/Si₃N₄/Air) resulting in a numerical aperture (NA, (24)) larger than 1. This fact generates a large acceptance cone for the input light ($\sim 70^\circ$, as well as the output light (90°)) within allowed angles θ_a (45) for guiding the light inside the waveguide core. Therefore, the theoretical coupling efficiency η_c is about 40 %, whereby equal areas of the devices further increase the coupling. The total efficiency η_{tot} is than given by equation (76) [71].

$$\eta_{\text{tot}} = \frac{P_{\text{in}}}{P_s} = \eta_{\text{ext}}\eta_c \quad (76)$$

Thus, in our case the total coupling efficiency between the Si-based LED and a photonic structure is considerable increases by the large index-contrast of the waveguide and the surface ratio. In addition, the reflectivity R (49) at the interface (SiO₂/Si₃N₄) is less than 2 %. Moreover, another evaluation can be done following the equation (50) introduced by Hunsperger [69] in the case of a laser diode. Here, factors like interface reflections, modal overlap and area mismatch in the field distributions of both devices are taken into account. Additionally, it can be assumed that there is only coupling between the fundamental laser mode and an even-order waveguide mode ($m = 0, 2, 4, \dots$). The drawback here is that in common optical circuits for biosensor or telecommunication applications the light coupling is realized from an external laser diode or by optical pumped waveguide lasers [21, 22, 23, 31, 33, 109, 110]. There are exceptions [17] but they need more difficult fabrication processes for an monolithic integration of all devices.

However, a more realist value for the estimation of the coupling efficiency for the system (Figure 39 (a, b)) is the usage of the measured external quantum efficiency (EQE) of the LEDs. As in the previous section (4.1.1) mentioned, the Tb:SiO₂ and Er:SiO₂ devices achieve an EQE in order of

16 % [128] and 14 % [129] while the Tb: and Er:SiN_x LEDs only reach 0.1 % [127]. These results clearly show that the obtained power efficiencies are notably lower than the theoretical estimated values (75). In conclusion, despite the disadvantages of the Si-based LED in comparison with a laser diode, like lower power efficiency and the uncollimated light as well as the low modulation bandwidth, a sufficiently high total coupling efficiency can be achieved due to a well-chosen design and material choice of the launched photonic structure. Especially, the high index-contrast waveguides with a high modal confinement may cause an efficient light transmission and the simple fabrication process leads to an integrated photonic circuit on a single chip.

5 FABRICATION METHODS

This chapter focuses on the used fabrication methods for the photonic structures, e.g. optical or E-beam lithography as well as reactive ion etching (RIE), and the previously known LOCOS process (Local Oxidation Of Silicon) for the light emitter preparation based on standard complementary metal-oxide-semiconductor (CMOS) technology [4, 24, 129]. Especially, an optimized processing of the photonic structures is necessary for efficient butt-coupled Si-based LEDs and low-loss light transmission of the integrated photonic circuit. Here, an overview is given about all investigated manufacturing routes and selecting the most suitable method.

5.1 SI-BASED LIGHT EMITTERS

The common fabrication process for Si-based light emitters was developed using CMOS technology [4, 24, 129, 145] on 4-inch, {100}-oriented, n-type silicon wafers with resistivity of 2 – 5 Ω cm. A summary of the established processes adapted to the use with integrated waveguides is shown in Figure 40.

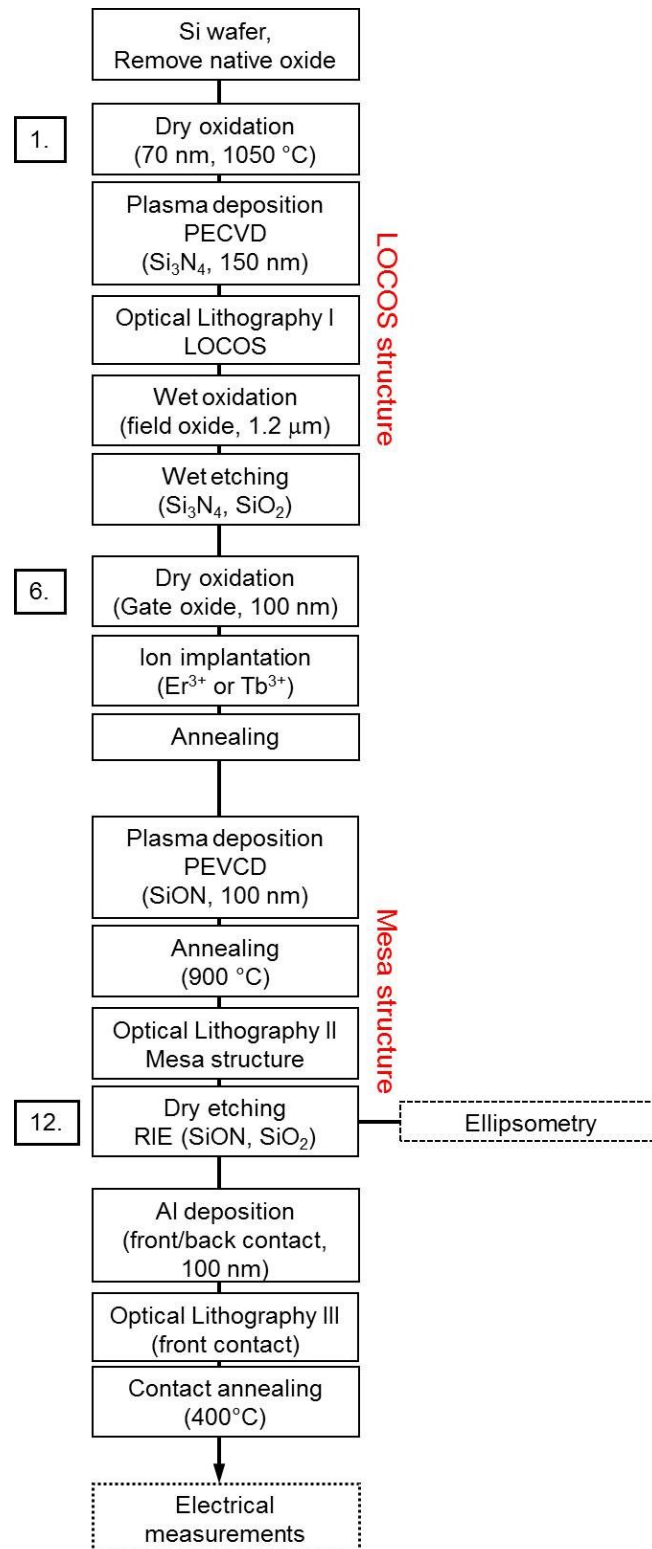


Figure 40: Processing scheme for the fabrication of Si-based LEDs [4, 24, 129, 145]

Both mentioned Si-based LED device structures (“SiO₂” and “SiN_x”) were prepared in standard silicon CMOS technology, which began with the removal of the native oxide from the Si substrate and is followed by the design of the LOCOS structure by photolithography. For the “SiO₂” devices the fabrication line in Figure 40 is used, while for the “SiN_x” LEDs step 6 contains instead the plasma deposition of 30 nm SiO₂ and 40 nm SiN_x (12 % Si excess) by plasma enhanced chemical vapor deposition (PECVD). The following steps were the ion implantation at room temperature (Research Center Freiburg) and furnace annealing (800 °C – 1100 °C), whereby the implantation doses were adjusted to generate a nearly constant RE concentration in a depth from 27 nm to 55 nm below the surface of the active layer. The profile of as implanted RE atoms with doses of 2E15 cm⁻² at 75 keV and 3E15 cm⁻² at 100 keV calculated by TRIM 98 shows a RE concentration of 1.5 %, as confirmed by Rutherford backscattering spectrometry (RBS) [145]. Additionally, detailed dopant profiles and the influence of the annealing temperature and technique can be found in [4, 24, 129, 145]. Thereafter, in the case of “SiO₂”-LEDs a 100 nm thick SiON protection layer is deposited by Plasma Enhanced Chemical Vapor Depositions (PECVD) with an Oxygen/Nitrogen ratio of 0.5 followed by a second annealing step. Afterwards, in both devices the Mesa preparation is done by photolithography and reactive ion etching (RIE). These steps (11, 12) are the critical ones for the system, because the etching depth must be precisely controlled regarding the SiO₂ box layer thickness for the integrated photonic device. Therefore, ellipsometry is used to check the remaining layer thickness. 100 nm of Aluminum was deposited on the back/front and lithographically patterned, after the residual oxide from the previous steps had been removed from the back. Then contact annealing for 30 min at 400 °C in Nitrogen ambient have been used in order to form a good quality of the Si/Al interface [145]. Moreover, and as already investigated [4, 24, 129, 145], various shapes of MOSLEDs with different feature sizes (round, square, oval dots) in the range from 300 to 750 μm and with transparent indium-tin-oxide (ITO, 150 nm) front electrodes were fabricated for testing the function of the devices in dependence on the geometry by electrical measurements (step 16, current-voltage (I(V)) and electroluminescence characteristics).

5.2 SI-BASED PHOTONIC STRUCTURES

The optimization of the fabrication of photonic structures provides the basis for developing efficient low-loss integrated photonic circuits for telecommunication and biosensing devices. Therefore, high quality parameters like low side wall roughness, steep slope angles and plane or polished waveguide endface [48, 49, 50, 53, 137, 146, 147], have to be met regarding easily integrated process steps. What makes this a challenge is that, the Si-based light source determines the course of fabrication processes and the degrees of freedom, e.g. layer structure, material consumption and geometry. As a consequence, the development of a joint fabrication line for single waveguides, tapers and photonic crystals was a prime objective before concentrating on butt-coupled Si-based light emitters. A summary and a concluding evaluation of the used technologies are given in the following section.

5.2.1 Waveguides, Tapers and Photonic Crystals

Si-Photonic devices, like high-index strip waveguides, are based on low RI material layers of the upper and lower cladding (e.g. $n_{\text{SiO}_2} \approx 1.5$) and high index core layers (e.g. $n_{\text{Si}_3\text{N}_4} \approx 2$) on a Si-substrate. Here, the most frequently used manufacturing techniques for the deposition of thin films of dielectric materials are PECVD, CVD as well as ion sputtering, which are CMOS compatible fabrication processes [34, 35]. The advantages of these planar technologies in comparison to the more expensive and inefficient fiber optic technology are the simple dimension control of even complex devices and the one-process fabrication of many structures on a single substrate as well as the easy past-cutting. Here, the minimum structure size depends strongly on the wavelength of the exposure source (e.g. 0.07 nm), thus E-beam

lithography achieves 10 nm scaled features with a focused beam diameter down to 5 nm and a minimum line width of 20 nm [69], which is why it is the most widely used method for patterning of submicrometer scale photonic devices in comparison to optical lithography. Typically, the layer is coated with a resist (e. g. Polymethylmethacrylate (PMMA)) which is sensitive to either photons of light or electrons such that the resist becomes either removable (positive resist) or non-removable (negative resist) by exposure [69]. Additionally, a mask is required, which serves as the structural pattern. Afterwards, a solution (e.g. acetone) is used which “develops” the resist and dissolves the removable areas. Furthermore, etching processes by dry or wet etching techniques, like reactive ion etching (RIE) or potassium hydroxide etching (KOH), are followed, whereas the resist is masking selected structures. In particular, the (an)isotropy, how the material is removed, limits the transmission and scattering losses determined by the quality of the side walls and front faces of the photonic devices. In summary, the right choice, based on past experience, of the lithographic method and the resist/mask as well as the most suitable etching technique and parameters due to the material composition and system design are crucial factors to obtain perfectly fabricated photonic structures with excellent transmission characteristics.

Early in this work, the research focus was on optical lithography for first waveguide fabrication in the micrometer range. The most important finding during this study are the choice of the correct etching technique, the usage of an additional Al layer working as an etching mask as well as the optimal plasma power. Thus, a detailed processing scheme for an optimized waveguide fabrication by photolithography is illustrated in Figure 41 (a – d).

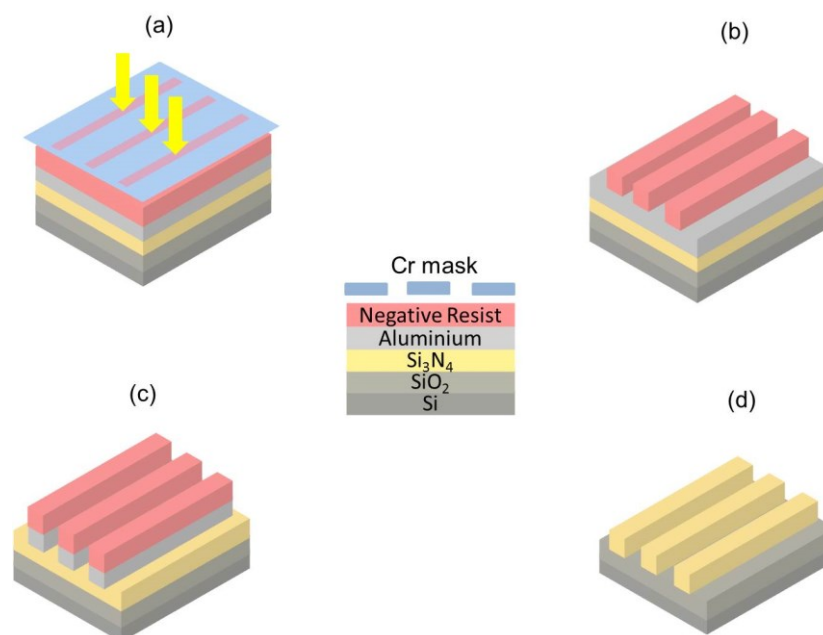


Figure 41: Schematics showing the fabrication steps of the photolithography

As can be seen from the picture above, after the deposition (PECVD) of a SiO₂ and Si₃N₄ layer with a certain thickness (1 μm) as well as an additional Al layer (100 nm) on the Si substrate the photoresist is applied by spin coating. Here, the coating type (PMMA) and thickness (0.5 – 0.25 μm) are important for an effective patterning. Then, a prebaking step is followed to drive off the photoresist on the wafer. Afterwards, a Cr mask containing the waveguide layout is used during exposing the wafer to intensive light (Figure 41 (a)). The unexposed regions get soluble in the developer due to properties of the negative resist (b). Figure 41 (c) shows, how the Al layer underneath is wet etched forming an additional mask in the last step for the waveguide structuring. From this point, the photoresist is no longer needed and removed by a “resist

stripper". Anyhow, in Figure 41 (d), reactive ion etching (RIE) or wet etching (KOH) is used for patterning the core layer of the waveguides. In practice, these methods exhibit high isotropy leading to under-etchings and deformed structures [53]. Nevertheless, the anisotropy factor of the RIE is larger and was increased by the usage of an additional Al mask. Moreover, an optimum plasma power for the RIE (150 W) as well as other adapted process parameters (e.g. etching time, gas flow) were found. Finally, the Al is removed and the optical devices are prepared for structural investigations, like scanning electron microscopy (SEM) and atomic force microscopy (AFM), whereas the results are discussed in chapter 7. In summary, an optimized fabrication process for micrometer ranged simple designed optical structures was developed.

Besides and in addition to the shown fabrication line of standard photolithography we developed an alternative manufacturing pathway of CMOS compatible silicon etched V-grooves. Generally, the V-grooves fabrication process is used for the integration of V-groove structures in the silicon substrate for aligning the fiber passively and [148, 149]. The fabrication line depicted in Figure 42 (a – f) demonstrates wholly innovatively designed free edge-overlapping waveguides, on the one hand, which otherwise improve the butt-coupling with external optical fibers via their free standing endfaces.

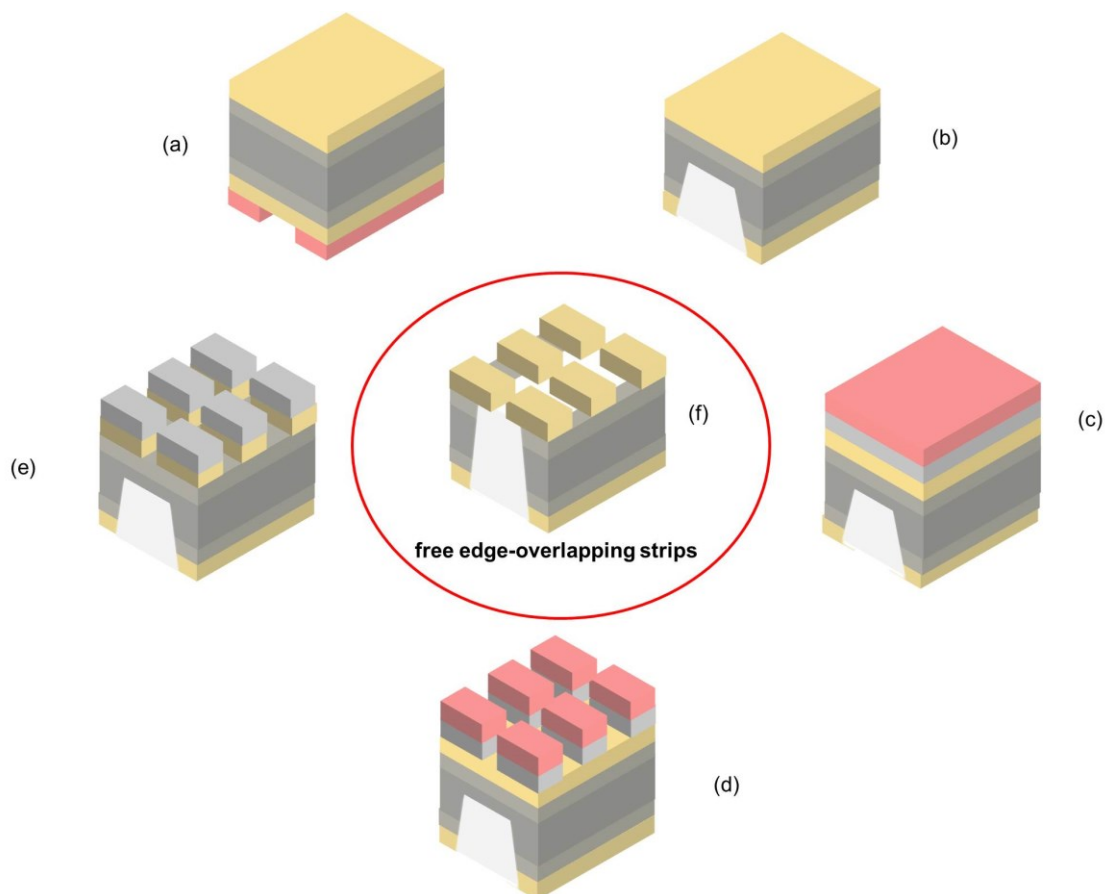


Figure 42: Schematics showing the fabrication steps of free edge-overlapping strip waveguides based on standard CMOS fabrication techniques

As illustrated above, the first sketch (a) summarizes the deposition (PECVD) of SiO_2 ($1.5 \mu\text{m}$) and Si_3N_4 ($1 \mu\text{m}$) layers on the front and back side of the Si substrate. The subsequent photolithography step is followed after applying the photoresist on the flipside. A Cr mask containing the V-groove layout is used during exposing the wafer to intensive light. Then in (b), RIE (150 W) and wet-etching by KOH created the V-grooves in the Si-substrate with a residual Si-layer of $40 \mu\text{m}$. The Si_3N_4 front layer perfectly offers protection of the front side during the etching process. Afterwards and as shown in sketch (c, d, e), the patterning of the front side occurred corresponding to the described steps in Figure 41 (a - d) ensuring strip waveguide formation. Finally (f), dry-etching leads to the removal of the residual Si-layer, whereby the SiO_2 serves as the etch stop layer. Thereafter, the front SiO_2 is removed by RIE from the back side to open the V-grooves and generating free edge-overlapping strips. To conclude, an alternative fabrication process based on the well-known V-grooves technique results in micrometer ranged newly designed two-dimensional photonic structures with free standing endfaces. The fabricated optical devices were characterized by SEM and AFM as well as studied by transmission measurements detailed shown in chapter 6 and 7.

However, if the structure size is further decreased the resolution limit of the method is reached and the roughness-induced losses significantly increase, thus an alternative fabrication method is necessary.

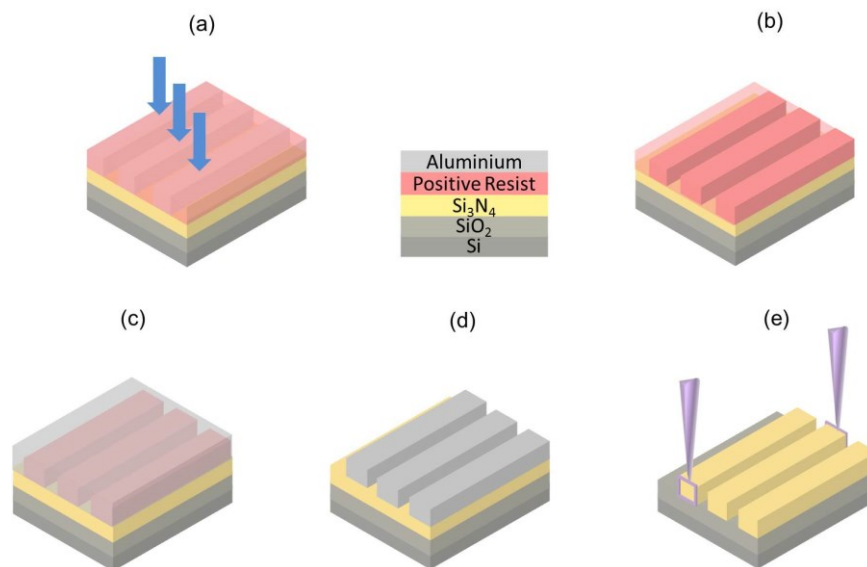


Figure 43: Fabrication line of the optical devices fabricated by E-beam lithography

Typically, the E-beam lithography is mainly utilized for semiconductor applications and advanced silicon photonics based on standard CMOS technologies. In comparison to the optical lithography, the electron beam width can go down to a few nm mainly limited by aberrations and space charges of the system. Anyhow, in the second part of this work, the shown fabrication recipe in Figure 43 (a – e) was developed for an optimized manufacturing of different optical devices in the submicrometer regime as waveguides, bends, tapers or photonic crystals. The first step of the process (a) requires the deposition of a SiO_2 and a Si_3N_4 layer by PECVD as well as the applying of the electron sensitive resist. Then, during exposing the resist solubility is changed enabling removal of the exposed regions (positive resist) by immersing it in a solvent (b). Here, the primary advantage is that the designed pattern is written directly without a mask. Anyhow, thereafter, as illustrated in Figure 43 (c), the created small structures in the resist are coated with an additional Al layer (100 nm). Afterwards, the lift-off or wet etching process (d) removes the undesirable material and simultaneously generates the Al etching mask. As shown in Figure 43 (e), the designed structures were finally transferred from

the resist to the core material of the photonic devices by RIE. Then, the residual Al is removed and an additional polishing step (e) of the structure front faces is realized by focused ion beam (FIB) milling. Anyhow, to conclude, the process parameters like the beam dose, width and mode as well as the resist thickness determine the quality of the fabricated structures. The side wall and front face roughness is primarily defined by the lithography (E-beam roughness ~ 10 nm - 20 nm) and etching method as well as their conditions. It has been found that the fixed beam moving stage (FBMS) mode and a double resist system provide best performance. Moreover, once again an Al mask for RIE etching of the Si_3N_4 core material as well as a lift-off process instead of wet etching leads to higher quality structures. In addition, FIB was used to decrease the roughness parameter.

5.2.2 Butt-Coupled Si-based Light Emitters

The previously acquired knowledge from the sections above serves as an orientation for the fabrication of coupled optoelectrical devices based on simple and cheap CMOS manufacturing standards. Figure 44 (a – g) shows in an evident manner the fabrication line of monolithically integrated (tapered) waveguide butt-coupled Si-based light emitters. The necessary process steps include already used and optimized techniques creating high performance integrated photonic circuits.

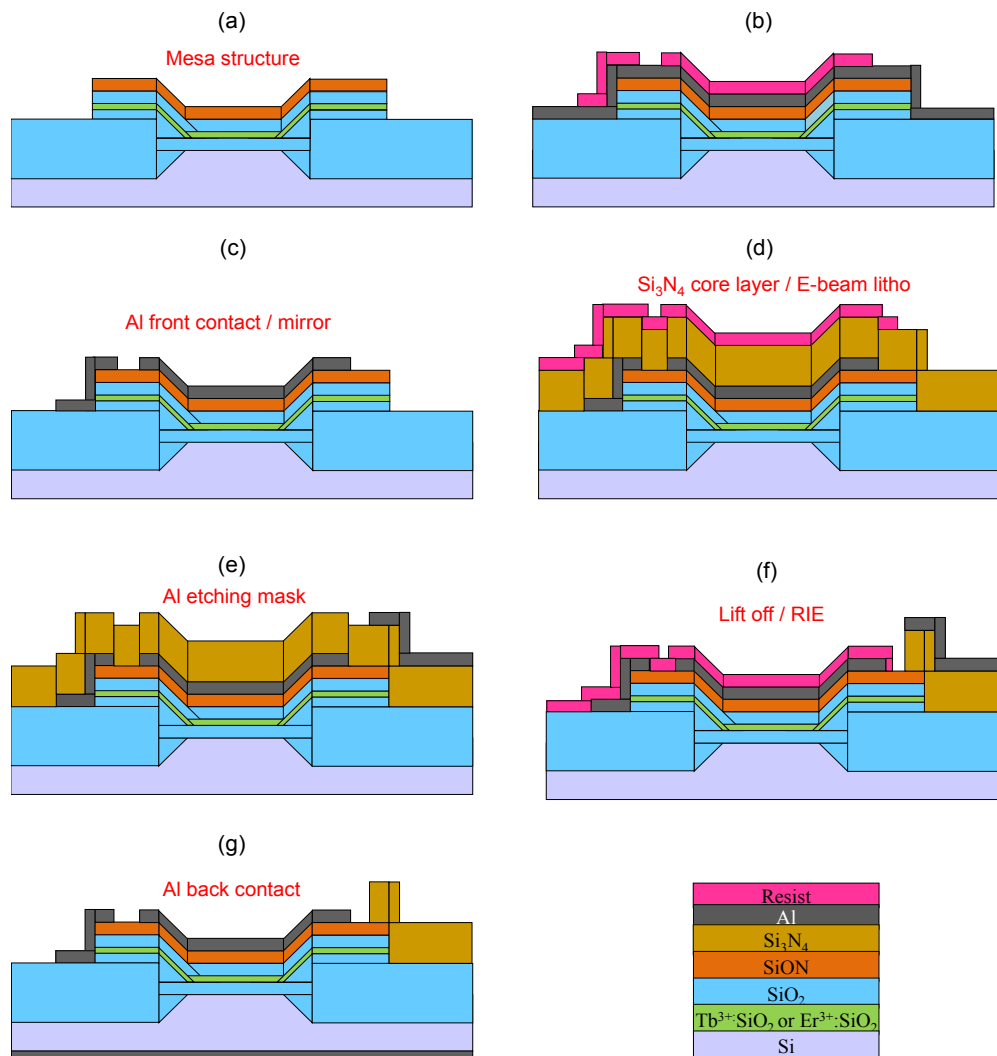


Figure 44: Fabrication scheme for waveguide butt-coupled Si-based light emitters exemplified by SiO_2 :LEDs (Er^{3+} or Tb^{3+})

It is important to keep in mind that the fabrication of waveguide butt-coupled LEDs is based on the previously mentioned process steps for single SiO_2 : and SiN_x :LEDs as illustrated in Figure 40. The lithographically generated mesa structure serves as starting point for the fabrication line of coupled optoelectrical devices (Figure 44 (a)). Additionally, it should be noted that precise etching into the SiO_2 is required for a maximum mode field overlapping and a critical box layer thickness concerning less radiation losses. Moreover, the scheme in Figure 44 (a – g) highlights just the processing of SiO_2 :LEDs, while in the case of SiN_x :LEDs another layer system must be taken into account. Anyhow, the first steps in Figure 44 (b, c) show the formation of the Al front contact and an additional Al mirror by Al sputtering (100 nm) and photolithography III. Here, the lateral patterned Al mirror may manipulate the path of light by reflection ($R = 85\%$) and increases the amount of coupled light into the connected optical device. Afterwards, the Al is etched and the resist is removed, which is followed by the deposition of the Si_3N_4 based photonic core layer ($0.5\ \mu\text{m}$) by PECVD and another resist coating for the subsequent E-beam lithography (d). In step (e), the resist is already removed and an Al layer (100 nm) is deposited working as an etching mask. Thereafter, in (f), the photonic core is designed by Al lift-off and RIE techniques. Finally, and as shown in Figure 44 (g), the residual Al and the resist are removed as well as the back contact is fabricated by oxide etching and Al deposition. Last of all, the (tapered) waveguides are polished by the introduced FIB technique.

In summary, the investigation of coupled SiO_2 : and SiN_x :LEDs is enabled through the experience from the individual processes of the manufactured photonic devices and the light emitter fabrication presents a framework for future integrated circuits (see section 5.2.1 and 5.1). Thus, the usage of E-beam lithography, RIE and Lift-off techniques and controlled process parameters primarily define the design of optimized optical devices. The application of an Al based etching mask and the integration of an Al mirror may enhance the structural and device performance. Chapter 7 is devoted to the optical analysis, like transmission measurements, of fabricated waveguide-coupled Si-based LEDs due to their device parameters.

6 CHARACTERIZATION METHODS

This chapter deals with the experimental methods validating the manufacturing processes of single photonic devices, e.g. waveguides, bends, tapers and PhCs, as well as Si-based light emitters and their coupling with the photonic structures. Firstly, we consider electrical measurements ($I(V)$ and electroluminescence characteristics) of the LEDs followed by the structural investigations as SEM and AFM, of the fabricated photonic devices. Additionally, waveguide butt-coupled LEDs were also analyzed using an experimental setup for transmission loss measurements.

6.1 SI-BASED LIGHT EMITTERS

As already been published in recent works [4, 24, 129, 145, 150] there are two different experimental setups to perform electrical or spectral resolved measurements of fabricated Si-based LEDs. A short overview of the respective methods is given in this section.

6.1.1 $I(V)$ and Electroluminescence Measurements

Figure 45 illustrates the current-voltage ($I(V)$) setup for electrical investigations of different Si-based light emitters with a transparent front contact (ITO).

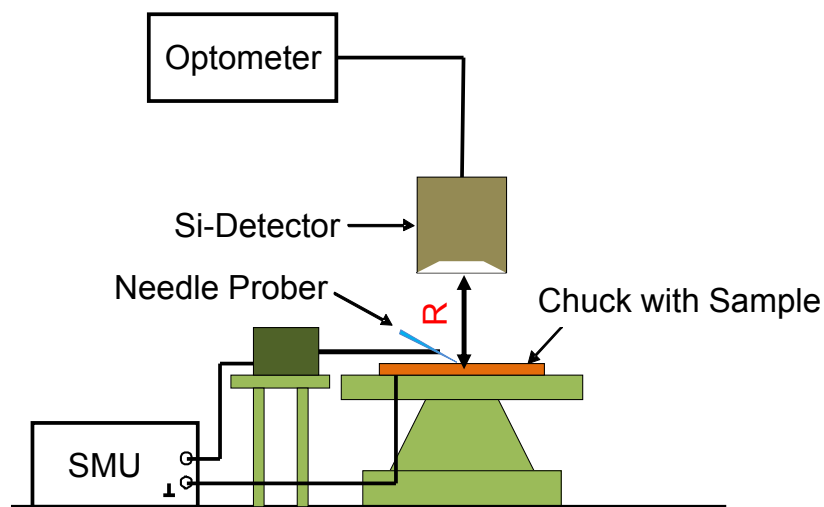


Figure 45 [150]: $I(V)$ measurement setup with an optometer at the darkbox

The shown setup is also equipped for measurements of the emitted light power which is detected by a Si or Ge detector head due to the emission wavelength of the active layer. The detector is connected to an optometer (Gigahertz Optik, P 9710), while the electrical supplies as well as the electrical measurements are performed by a source meter unit (SMU) from Keithley with a current range from 10 fA to 10 mA and voltages up to 1.1 kV (Keithley 237) [150]. Moreover, the samples were placed on a chuck in which a needle prober touched the ITO electrode of a single dot and the detector head with an active area of $A = 1 \text{ cm}^2$ was being placed above the sample in a distance of R . Thus, the emitted light power P_{out} can be recalculated according to

$$P_{\text{out}} = \frac{1}{2} P_{\text{det}} \frac{2\pi r^2}{A} \quad (77)$$

with P_{det} as the power measured with the optometer and a correction factor of $1/2$, which is related to the lambertian emission characteristic of the used LEDs. Therefore, P_{det} is automatically monitored by the controlling LabView program. Additionally, a constant current can be applied for voltage and optical performance measurements (V_{cc}).

In addition to electrical characteristics spectrally resolved electroluminescence (EL) measurements were performed in the setup shown Figure 46.

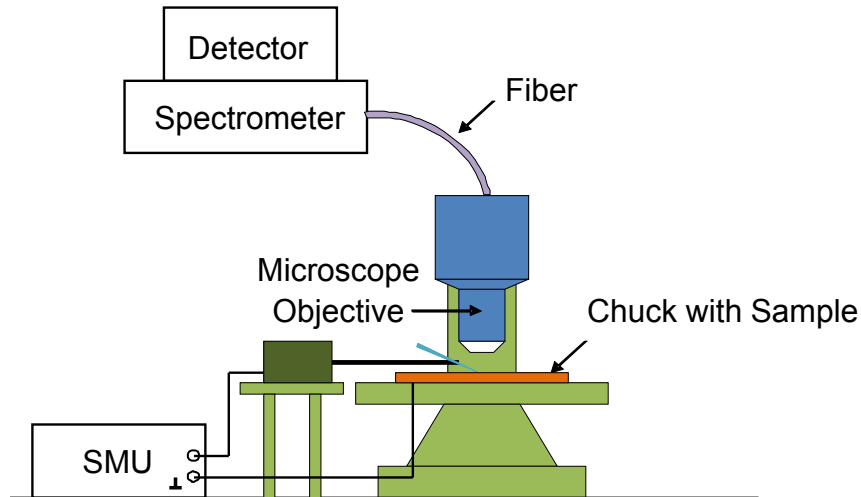


Figure 46 [150]: Spectrally resolved EL measurements with a microscope

In this setup the emitted light from the LED (with an IOT front contact) is collected by a microscope objective, which is connected to the spectrometer by a glass fiber. The used spectrometer was from Andor (SR-303i) with a blazed grating (150 lines/mm, center wavelength 500 nm) and a CCD detector (Andor iDus, DU401A-BR-DD) [150]. Again, a high voltage SMU (Keithley 2410) is used for the electrical supply and the electrical measurements, whose negative port is connected to the sample via the chuck and the Al back contact, while the front contact is connected to the positive port by a needle probe [150]. Thus, such a polarity leads to an electron injection from the Si into the SiO_2 which are flowing thereafter to the top electrode. Anyhow, the electroluminescence (EL) spectra under certain voltage conditions of the LEDs due to certain device parameters as doping material or size were observed.

6.2 SI-BASED PHOTONIC STRUCTURES

During this study different structural characterization methods are used to evaluate the manufacturing processes of certain optoelectrical devices. The focus is set on scanning spectral ellipsometry, electron microscope (SEM) and atomic force microscopy (AFM). Moreover, a special transmission measurement setup was built to determine optical loss analysis of different photonic structures as well as butt-coupled Si-based LEDs. The mentioned techniques are shown briefly in the following sections.

6.2.1 Structural Characteristics

This section describes three methods used for structural studies of manufactured photonic devices regarding their material parameters due to the fabrication processes. The first technique, spectral ellipsometry, allows the characterization of the material composition, roughness and thickness as well as other material properties. Figure 47 illustrates the simple measurement setup, whereby the detected signal is changed in polarization as the incident

radiation interacts with the material structure of interest. This contact free characterization tool quantifies the change of polarization due to several material parameters and optical constants, e.g. thickness and refractive index, of films of all kind.

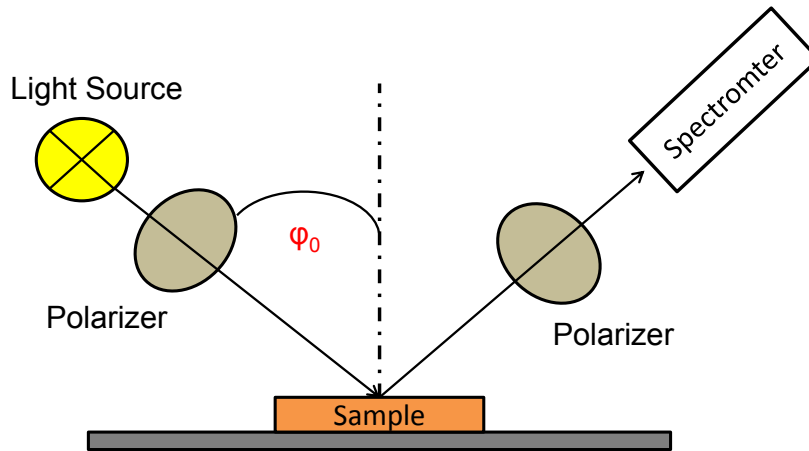


Figure 47: Ellipsometry setup

An incident wave of a certain angle (ϕ_0) and polarization shows a difference of the amplitude (Ψ) and polarization (Δ) after reflection at the sample. Thus, the reflectance ratio p of the parallel (E_p^0) and perpendicular (E_s^0) components of the field results from the Fresnel coefficients r_s and r_p and can be described as

$$p = \frac{r_p}{r_s} = \tan \Psi * \exp(i\Delta). \quad (78)$$

Anyhow, the shown measurement setup is based on an ellipsometer from J.A. Woollam Co., a broad band light source (FLS-300 75 W Xe Arc) and a spectrometer (M-2000FI). The computer software WVASE32 was used for data input and controlling. Moreover, the material database of the software enables the analysis of the deposited material layers. The simulation of the dispersion curves for the determination of the refractive index n is done with the Cauchy model of the fitting parameters in A, B and C [151]

$$n(\lambda) = A + \frac{B}{\lambda^2} + \frac{C}{\lambda^4}. \quad (79)$$

However, further important informations for the evaluation and optimization of process steps for the fabrication of different optical structures can be obtained by the use of a scanning electron microscope (SEM) creating high-resolution images better than 1 nm. A simple schema is given in Figure 48. Especially, for the characterization of lithographically fabricated structures according to the process parameters, e.g. photoresist thickness and exposure time or etching technique and mask, the SEM allows a qualitative evaluation.

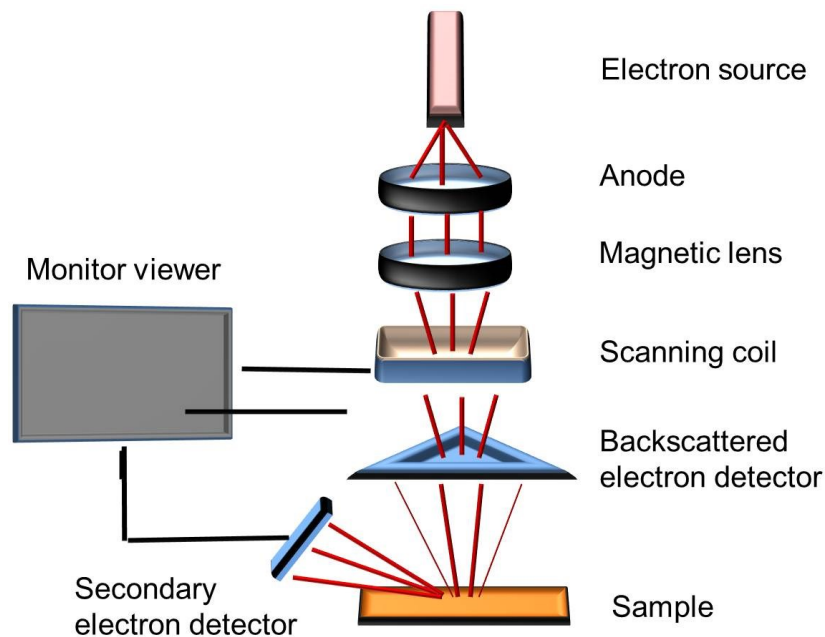


Figure 48: Schema of a scanning electron microscope (SEM)

Anyhow, as shown in the schema above, the electrons are produced by an electron source, which are accelerated through an anode plate and focused with a magnetic lens. The scanning coils force the electron beam to rapidly scan over a certain area of the sample. Finally, the backscattered/secondary electrons are captured by the detectors and the surface topography is reconstructed at the monitor. In addition, the image quality is affected by the beams diameter, accelerating voltage and working distance as well as disruptive artifacts like discharges. However, in this work, this method is used for the optimization of the fabrication process due to the revealed possible defects and the evaluated waveguide side walls and fronts.

Atomic force microscope (AFM) is a very high-resolution type of scanning probe microscope, with a resolution in the order of nm that enables the visualization of the surface structure of almost all materials [152]. Figure 49 demonstrates the setup and working principle of an AFM.

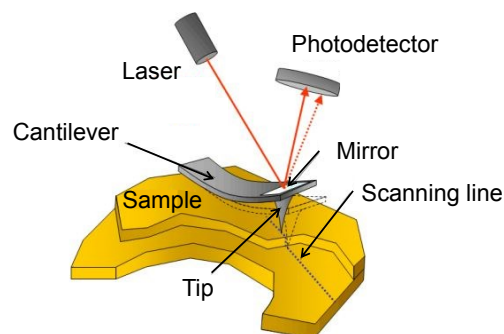


Figure 49: Schema and functioning of an atomic force microscope (AFM)

Usually, the AFM operation is described as one of three modes due to the nature of the tip motion. A distinction is made between the contact mode, the tapping mode and the non-contact mode. Generally, the first two modes are used for structural investigations, e.g.

roughness values of deposited layers. The cantilever with a tungsten tip is driven over the sample, whereby it oscillates up and down near its resonance frequency by a small piezoelectric element mounted next to the AFM tip holder (tapping mode) [152]. The amplitude of the oscillations is in the range of 100 to 200 nm. Due to electrostatic forces the amplitude is decreased and the tip gets closer to the sample. As the cantilever is displaced via its interaction with the surface (deflection measurements), the reflection of the laser beam will be displaced on the surface of the photo detector.

6.2.2 Transmission Measurements

The last objective of this work is the development of a transmission measurement setup for fabricated single photonic structures and butt-coupled Si-based LEDs for SM/MM operation. Firstly, the transmission loss of the single optical structures, e.g. straight and bended waveguides as well as tapers should be characterized in order to have an idea about the propagation loss and device performance according to the fabrication process. As mentioned in chapter 2.3 several techniques are available for optical loss measurements, whereby the information required from the experiment must be clear to define the method. In this work, the total loss of the waveguide will be investigated excluding insertion losses. Therefore, end-fire coupling is used and the focus is on the measurement of the transmitted power to determine the attenuation coefficient α (61). The results will be transferred into improved design and fabrication parameters for the manufacturing of optimized integrated coupled Si-based LEDs with a high performance. Anyhow, a schematic diagram of the transmission measurement setup is shown in Figure 50.

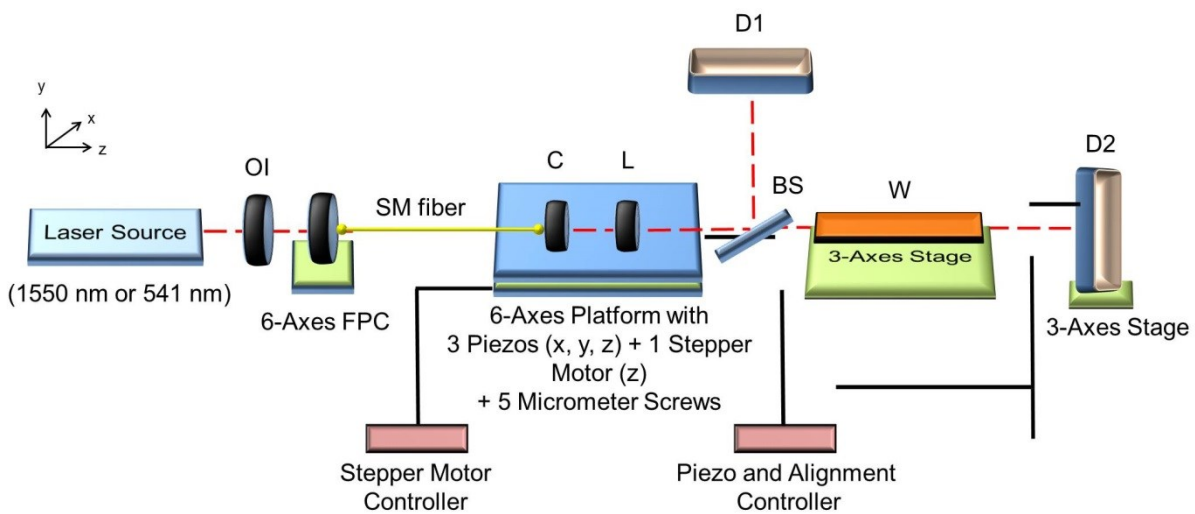


Figure 50: Transmission measurement setup: Optical Isolator (OI), Fiber Port Coupler (FPC), Collimator (C), Lens (L), Beam Splitter (BS), D1/2 (Detector), Sample (W)

A laser source (1550 nm or 541 nm) is end-fire coupled into a SM fiber ($\text{NA} = 0.14$) through an optical isolator (OI) and a FiberPort Coupler (FPC, Thorlabs PAF-X-7-C) including an aspheric lens ($\text{NA} = 0.29$). The OI is minimizing the back reflection into the laser and the FPC enhances the laser-to-fiber coupling as well as the beam collimation by six axis alignment. Afterwards, a beam splitter (BS) can be used to adjust the beam onto a first detector (D1) determining the input energy for followed sample coupling. Anyhow, a collimator (C, $\text{NA} = 0.49$) and a lens (L, $\text{NA} = 0.5$) are fixed on the six axis platform (Thorlabs NanoMax600) with closed-loop internal piezoelectric actuators (x, y, z) and five high precision differential micrometer screws ($x, y, \alpha, \beta, \gamma$) allow to launch the laser beam directly into the sample (W, $\text{NA} > 1$). These actuators provide a 20 μm travel range with a positional resolution of 20 nm. Moreover, a modular stepper motor

actuator is installed at the optical axis (z) ideal for short travel steps of 60 nm, respectively. The motorized stage and the high NA of the fabricated optical device may achieve maximum coupling efficiency. Finally, the output of the waveguide can be collected and focused with a collimator lens into the seconded detector (D2, Si or InGaAs). Thus, the transmitted power of the sample (W) can be measured and analyzed. Nevertheless, the cut-back method is a simple technique to determine the loss coefficient α of an optical device (see chapter 2.4). Also, the setup shown above can be used to detect the optical output of shortened waveguides as well as it is suitable for the optical characterization of fabricated butt-coupled Si-based LEDs, while the input part is not required.

In the case of high-aspect-ratio waveguides the transmission measurement setup of the department of Strained Nanoarchitectures at the Leibniz Institute for Solid State and Materials Research (IFW, Dr. A. Madani) enabled clear statements about attenuation coefficients of the fabricated structures.

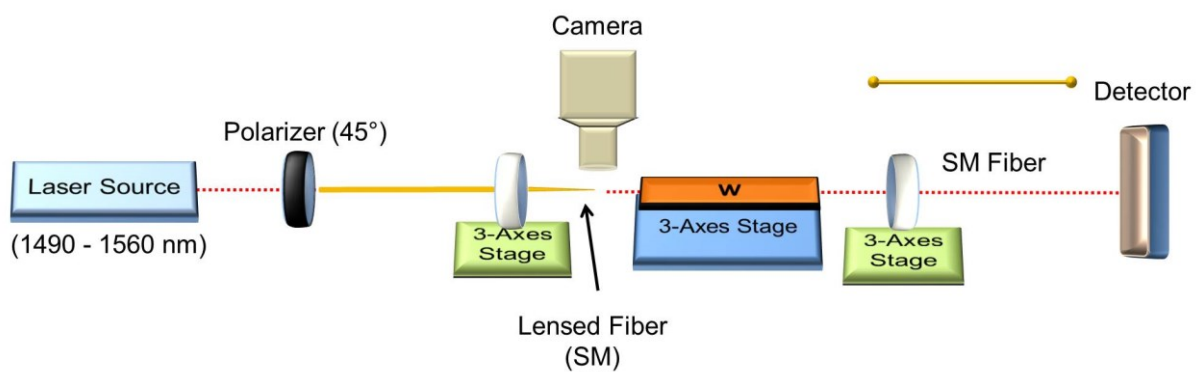


Figure 51: Transmission measurement setup with special Lensed Fiber (SM)

As depicted above, the setup contains a tunable laser source (1490 nm – 1560 nm) connected to a polarizer for TE or TM polarized light and a SM lensed fiber with a focal length of $1.7 \mu\text{m}$. The in- and output coupling is enabled through a camera watching the endface of the waveguide sample adjustable on a 3-axis table. The output power is collected by a standard $9 \mu\text{m}$ SM fiber connected to an IR-detector.

7 RESULTS

This work is focusing on the development of a Si-based photonic circuit based on two important components - the Si-based LED and a monolithically integrated strip waveguide for MM or SM operation. Here, the estimation of the coupling efficiency between the optoelectrical and optical devices as well as the transmission characteristics of the complete system depends on the design parameters and the optical (electrical) performance of each component. Therefore, this chapter gives an overview of the main measurement results of the individual system elements and an analyses as well as an evaluation of the fabricated and examined Si-based photonic circuit.

7.1 SI-BASED LIGHT EMITTERS

As already described in chapter 6.1 different experimental setups for optical and electrical measurements of fabricated Si-based LEDs have been used in this study. The influence of design parameters, e.g. dot size or active layer thickness, on the device performance were investigated with $I(V)$, V_{cc} and electroluminescence (EL) measurements (Figure 45, Figure 46).

It is important to mention, that the SiO_2 and Si_3N_4 layers were deposited by PECVD with Standard-Oxford recipes [85] and the Si-rich SiN_x layers (12 % Si excess) [127] of the LEDs were manufactured by the research group in Freiburg.

As can be seen from below, the current-voltage characteristics of $\text{Er}:\text{SiO}_2$ LEDs due to the dot size diameter (d) was determined by $I(V)$ -measurements. Here, the examined LEDs are based on 100 nm thick Al front contacts with three different dot diameters ($d = 300, 500$ and $750 \mu\text{m}$).

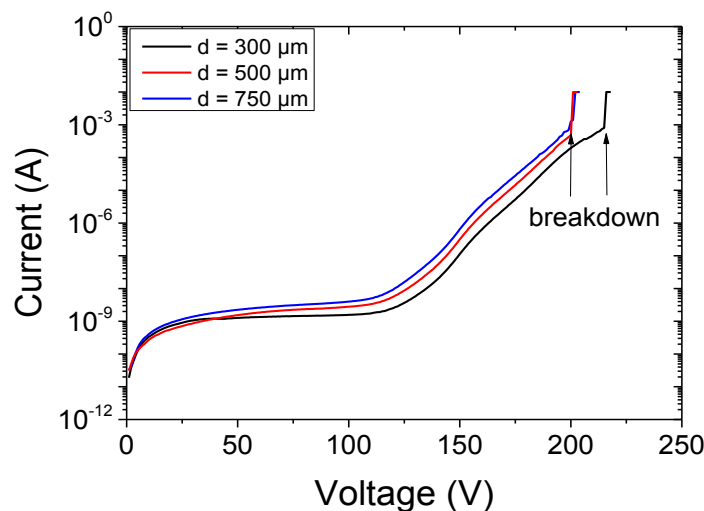


Figure 52: $I(V)$ curves of $\text{Er}:\text{SiO}_2$ LEDs with Al top electrode due to the dot diameter $d = 300, 500, 750 \mu\text{m}$ (logarithmic scale)

Generally, Aluminum is a better choice for the front electrode than ITO in order of electrical performance and in the case of charge injection from the substrate into the oxide [126]. Anyhow, the results shown here are in good agreement with the measured electrical properties of previous fabricated single Si-based LEDs [126, 145, 150]. Moreover, this study clearly illustrates that the dot size does not affect the charge injection or defect accumulation in the guiding layer. As usual, the breakdown voltage is around 200 V due to the thickness of the dielectric (SiO_2 , 100 nm) whereas the smallest dot resists higher voltages. That is caused by the

fact, that during injection electrons produce defects in the oxide (as well as intrinsic defects like hydrogen and carbon) causing into a breakdown voltage. However, in statistics, greater dot diameters result in higher probability of defect paths.

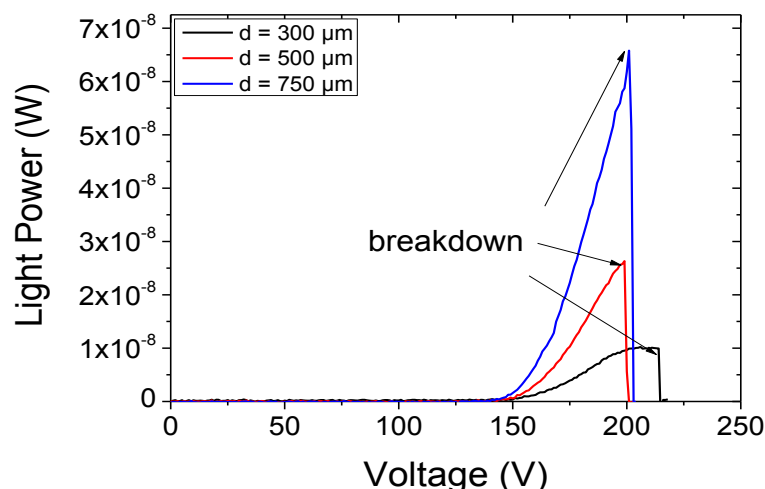


Figure 53: I(V) curves of Er:SiO₂ LEDs with transparent ITO front contact due to the dot diameter $d = 300, 500, 750 \mu\text{m}$

Additionally, Er:SiO₂ LEDs with transparent ITO top electrodes with different dot diameters d were investigated due to their optical performance (V_{cc}). As illustrated in Figure 53, the light emission for all devices only starts from 150 V and the breakdown voltage is reached round 200 V [126, 145, 150]. Especially, the smallest dot (black line) shows the characteristic emission saturation as well as, already indicated above, the longest lifetime [126, 145, 150].

Furthermore, EL measurements were performed with the setup described in section 6.1.1. A constant current of $5 \mu\text{A}$ was applied to a Tb:SiO₂ (RE 1.5 %, 100 nm SiO₂) sample based on a ITO electrode with a dot diameter of $d = 500 \mu\text{m}$.

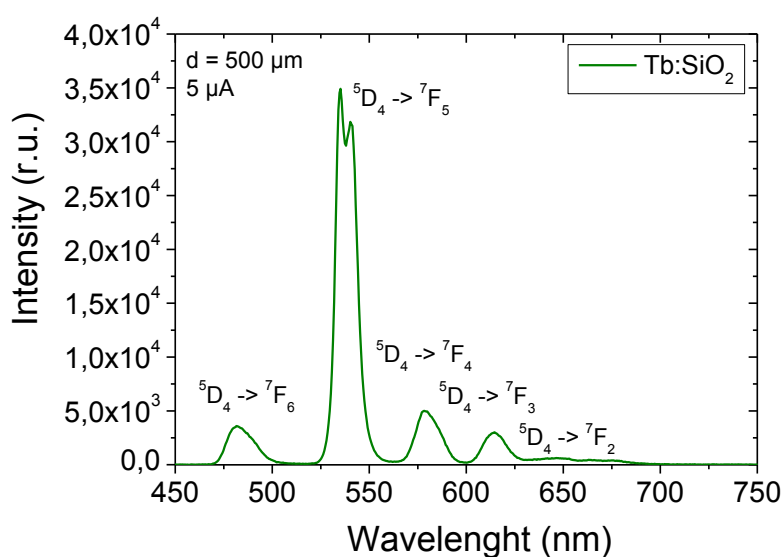


Figure 54: EL spectrum of Tb:SiO₂ LEDs with ITO front electrodes ($d = 500 \mu\text{m}$); common optical transitions [129, 145]

The EL spectrum above shows the characteristic well-known optical transitions of the Tb^{3+} ion. The main emission peak is observed at 535 nm generated by $^5D_4 - ^7F_5$ transition [145]. Beside this green emission, the measured data of the LED shows additional radiations in the blue (480 nm), yellow (578 nm) and red (614, 650 nm) region of the spectrum. The observed EL intensity values and peak positions are in good agreement with the optical characteristics of $Tb:SiO_2$ LEDs published by Sun et al. [128, 129] and Skorupa et al. [145]. In addition, the $Tb:SiN_x$ devices show an equal but intensity less EL characteristic [127].

Moreover, Figure 55 (a, b) illustrates the measured EL intensity of $Er:SiO_2$ LEDs (RE 1.5 %, 100 nm SiO_2) in the visible and infrared range due different dot diameters d .

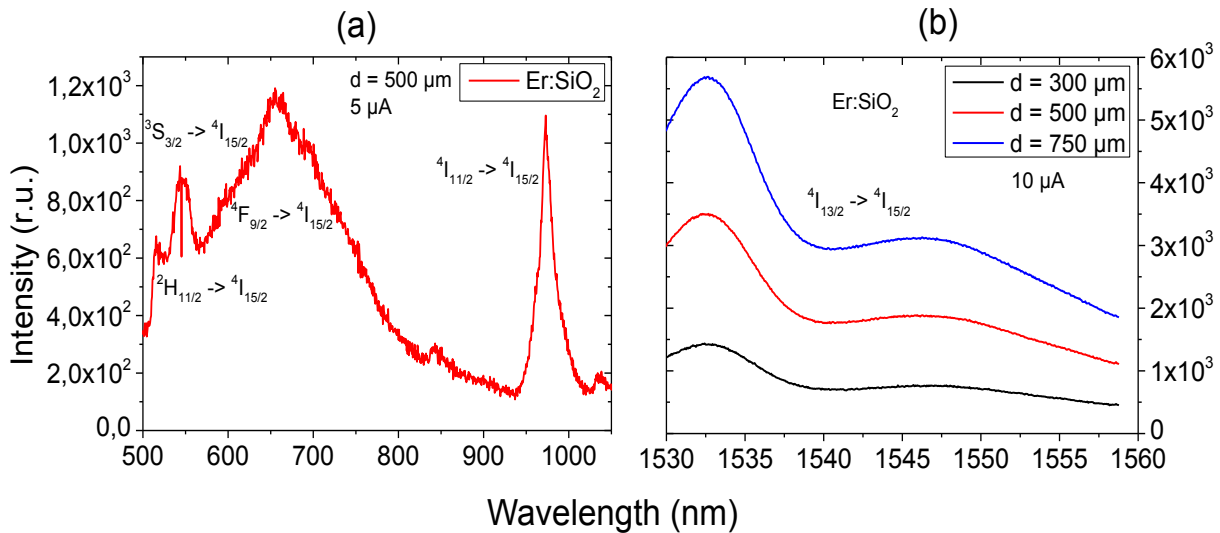


Figure 55: EL spectrum with the most common transition states [129] of (a) $Er:SiO_2$ LEDs with ITO front electrodes ($d = 500 \mu m$); (b) $Er:SiO_2$ LEDs due to the dot diameter d

Depending on the matrix composition the Er^{3+} -ion is formed by the loss of one 4f electron and both of the 6s [153]. The 5s and 5p shells shield the incomplete 4f shell leading to weak luminescence from this ion in comparison to terbium. Moreover, the intra-4f transitions are still not fully allowed, resulting in excited state lifetimes in the order of ms making Er^{3+} interesting for laser applications. As can be seen from the figures above, the strongest optical transition of the Er^{3+} -ion due to the host material is that from $^4I_{13/2} - ^4I_{15/2}$ (~ 14 ms) [153] between 1530 nm and 1560 nm. Additionally, stark splitting due to the crystal field of the host (Figure 55 (b)) lifts the degeneracy of the erbium 4f energy levels producing a doublet peak at 1532 nm and 1548 nm [85, 153]. Furthermore, erbium has found its application as a component in phosphors regarding its other radiative transitions that yield luminescence in the visible region (Figure 55 (a)) [153]. Unfortunately, these are mostly suppressed in silicon and are of little importance for common telecommunications applications [153]. Generally, the EL intensity can be scaled with the dot diameter of the device. In conclusion, all discussed results are consistent with the literature [129, 145].

Figure 56 (a) shows the EL spectra of $Er:SiN_x$ LEDs (RE 1.5 %, 40 nm Si-rich SiN_x [127]) with different dot diameters d . Moreover, the common Er^{3+} optical transitions in the free ion and in a solid as well as the corresponding wavelengths are clarified by the schematic energy level diagram in Figure 56 (b) [85, 154].

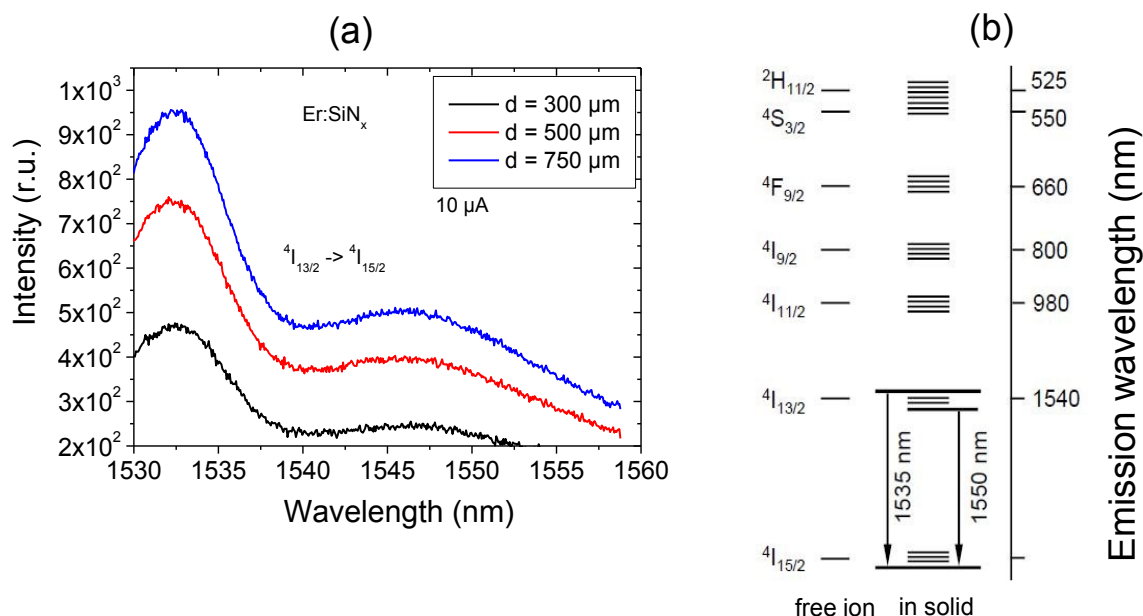


Figure 56: (a) EL spectrum of Er:SiN_x LEDs due to the dot diameter d , (b) Schematic energy level diagram of Er³⁺ with the common transitions in the free ion and in a solid

The figure above underlines, that under electrical pumping Er³⁺-doped LEDs with Si-rich SiN_x as host material exhibit EL bands at 1532 nm and 1545 nm. Then again, the largest dot diameter equals the strongest measured EL intensity. In addition and as published in [130, 145], the devices show an equally EL spectrum in the visible range such as the Er:SiO₂ LEDs (Figure 55 (a)).

In summary, the obtained results of the examined Er³⁺ and Tb³⁺ implanted Si-based LEDs with a SiO₂ and/or SiN_x active layer confirm the findings in previous studies [127, 128, 129, 130, 145]. It is also clear that the given values for the EQE of 16 % for Tb:SiO₂ [128], 14 % for Er:SiO₂ [129] and of 0.1 % for Tb/Er:SiN_x [127] LEDs are directly linked with the measured EL intensities.

7.2 SI-BASED PHOTONIC STRUCTURES

This chapter will focus first on used structural characterization methods in order to make detailed statements about the impact of the fabrication processes, like PECVD, lithography and RIE, on the material parameters, e.g. refractive index n (RI) or surface roughness, of the manufactured Si-based LEDs and photonic devices. Afterwards, results from the performed transmission loss measurements are presented.

Spectral ellipsometry was used to obtain and analyze optical parameters of the deposited layers with the help of the material database of the software. Figure 57 illustrates the simulated dispersion curves done with the Cauchy model (79) of the fitting parameters (A, B, C) in the wavelength range between 400 – 1600 nm.

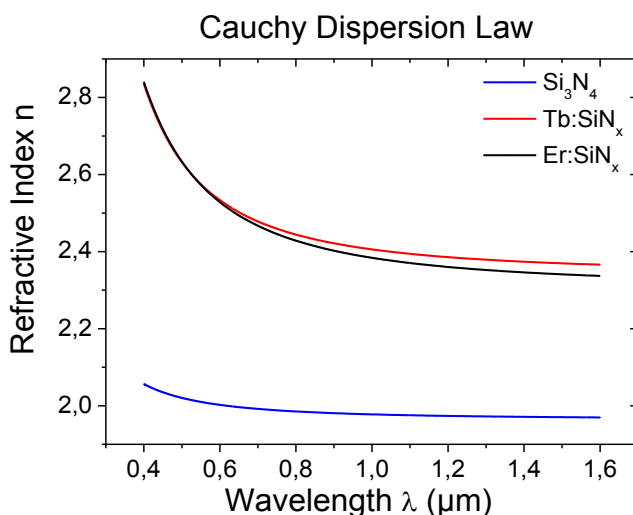


Figure 57: Dispersion curves of the deposited SiO_2 , Si_3N_4 and implanted SiN_x layers

The used fitting parameters for each layer as well as the parameter variance (dX) and the resulting RIs according to 541 nm and 1550 nm are summarized in Table 9.

Table 9: Ellipsometry data of the deposited layers due to the important wavelengths

layer	A	dA	B	dB	C	dC	n (1550 nm)	n (541 nm)
SiO_2	1.4706	2.02E-4	0.00591	1.26E-4	-2.4E-4	2.12E-5	1.4709	1.4880
Si_3N_4	1.9648	0.00104	0.01264	0.00156	3.20E-4	6.08E-4	1.9702	2.0119
Tb:SiN_x	2.342	0.251	0.06095	0.0312	0.00287	0.00519	2.3704	2.5839
Er:SiN_x	2.3076	0.261	0.07496	0.016	0.00169	0.00251	2.3399	2.5824

It can be seen from above, that the related values for Tb: and Er: SiN_x layers (1.5% RE concentration) of the LEDs show increased RIs which differ only slightly from each other. Thus, the Δn of the dielectric layer system of the device may lead to a very narrow waveguiding layer resulting in light confinement and sideways propagation. In addition, the obtained results can be used for statements about the Tb: and Er: SiO_2 layer too, which should lead to a similar light confinement. In summary, the implantation generates the active layer, but also may enhance the coupling situation by the creation of a second guiding layer between the Si-based LED and the optical device.

Moreover, another important investigative method of choice is AFM. Here, Figure 58 shows a $3 \times 3 \mu\text{m}$ scan of a fabricated strip waveguide produced by E-beam lithography based on a core cross-section of $0.5 \times 1 \mu\text{m}^2$, respectively.

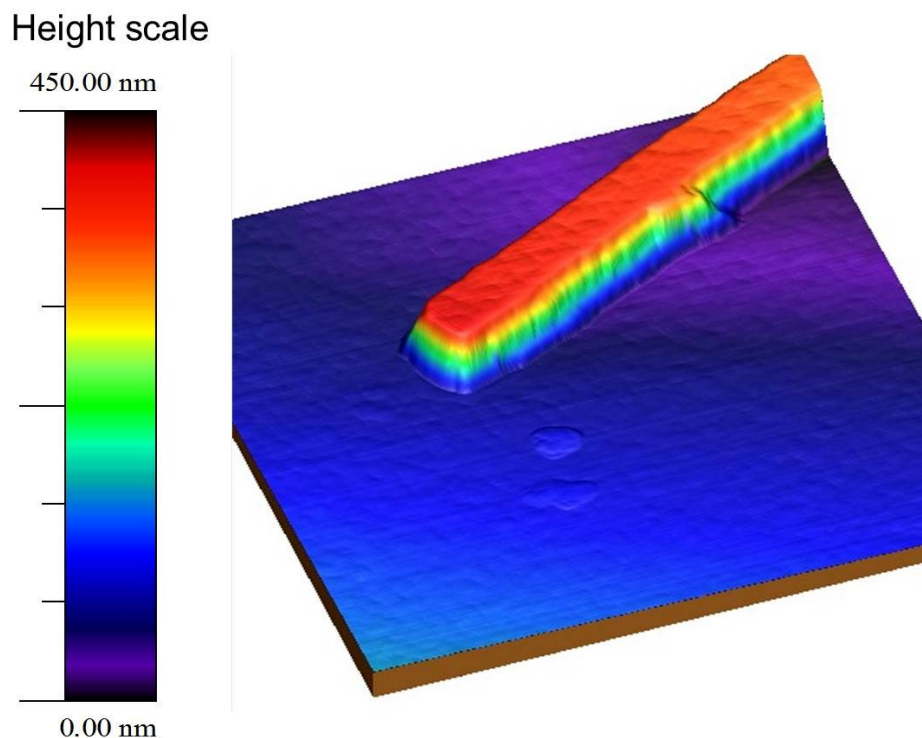


Figure 58: $3 \times 3 \mu\text{m}$ scan of a Si_3N_4 -based fabricated waveguide with a cross-section of $0.5 \times 1 \mu\text{m}^2$

The primary focus of this study was, beside the side and front wall roughness inspection, on the verification of the accurate core height after RIE. As one can see, the process steps carried out lead to well manufactured structures with mostly correct core heights but with trapezoidal cross-sections (see chapter 4.1.2.1 Table 8 for tilt angle), which need to be improved in the future. E-beam or optical lithography and RIE strongly effect on the quality of the optical devices. As has been pointed out by Poulton et al. [50], the side wall roughness usually arises due to imperfections in the etching mask as well as to anisotropies in the etching processes itself and can result in an additional propagation loss due to radiative scattering into the surrounding material and into backward-propagating modes. Unfortunately, Daldosso et al. [132] also found out, that it is quite difficult to achieve low propagation losses for high index-contrast waveguides, whereas waveguides with Si_3N_4 cores and SiO_2 cladding layers represent one of the best solutions to have large refractive index differences, low scattering losses, negligible absorption losses and high compatibility with Si technology. Furthermore, Melchiorri et al. [133] investigated very thin Si_3N_4 waveguides ($h = 0.25 \mu\text{m}$) showing high significant propagation losses at 1544 nm of about 4.5 dB/cm because of the poor optical mode confinement factor, but also structures with reduced interface roughness and minimized scattering losses (1.5 dB/cm) due to the LPCVD technique. The research results of Ye [53] confirm, that the cross-sectional profiles (rectangular or trapezoidal) of the waveguides are crucially determined by the choice of the etching technology as well as the etching mask. Dry-etch processing, like RIE, are used when deep vertical sidewall etchings are required, but it is more complicated in comparison to wet-etching. On important advantage for wet-etching is that it tends to produce smoother sidewalls as compared to RIE and thus scattering losses are significantly reduced. Nevertheless, our structure show slanted profiles and rough side walls, because of still not non-optimum etching parameters on which should be explicitly focused in future projects.

This issue becomes even more clear and urgent by a closer look using SEM. As illustrated in Figure 59 (a – d), the structural analysis of fabricated waveguides by photolithography show the impact of the selected etch process (RIE or wet-etching).

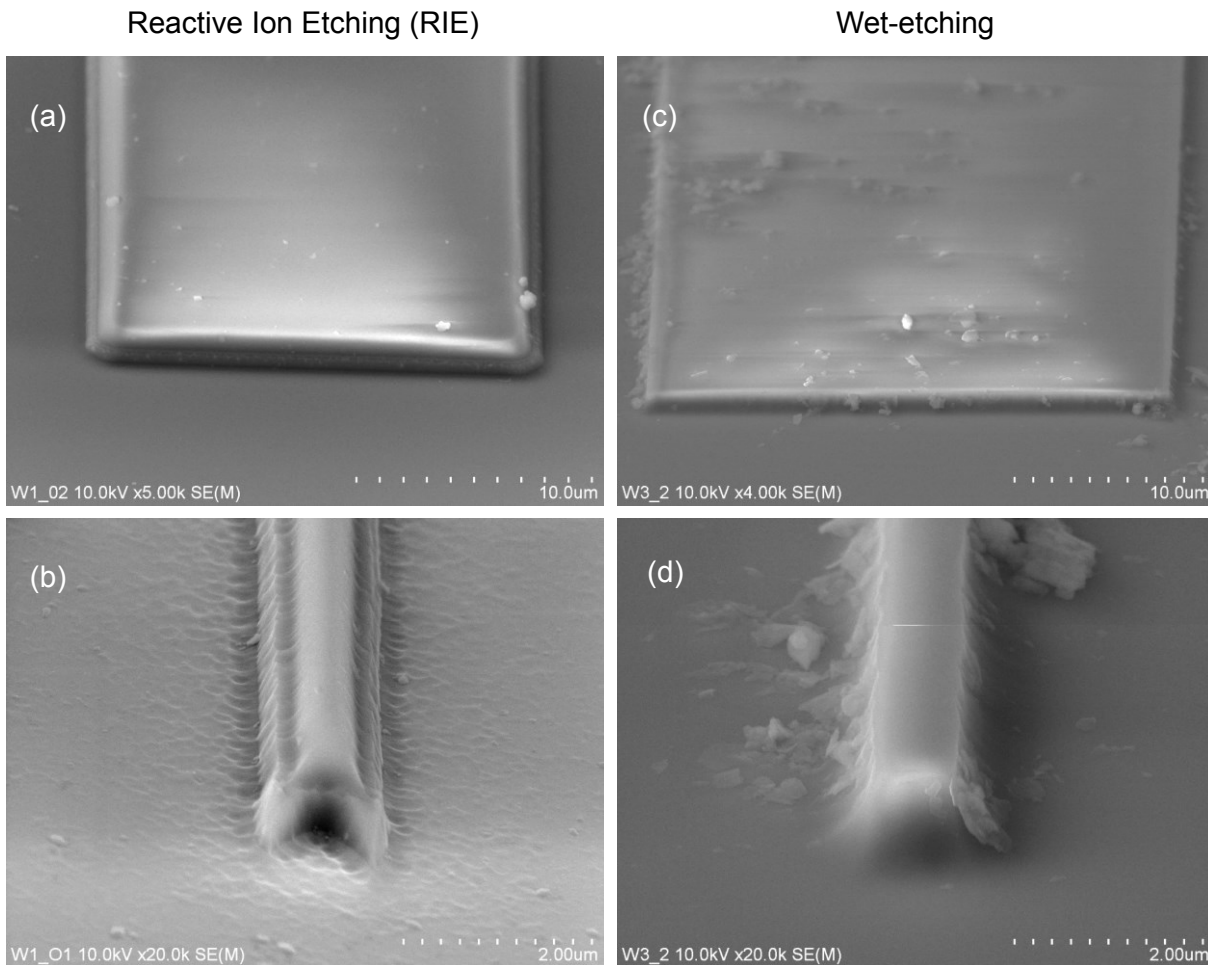


Figure 59: SM/MM waveguides based on a Si_3N_4 core and a $1 \mu\text{m}$ thick lower cladding fabricated by optical lithography and RIE (a, b) or wet-etching (c, d); cross-sections: (a, c) $1 \times 20 \mu\text{m}^2$, (b, d) $1 \times 1 \mu\text{m}^2$

As already mentioned in chapter 5, the investigated process recipe (Figure 41) includes photolithography for the fabrication of first waveguide structures in the micrometer regime. Here, RIE and wet-etching (KOH) were analyzed. It should be remembered, that the optical light path is influenced by the propagation characteristics of TE and TM modes. This implies that the side wall and top surface roughness determines the propagation loss of the optical devices. Figure 59 (a – d) quite clearly shows the advantages and disadvantages of both methods. As Ye [53] already indicated, RIE leads to steeper side walls, but also exhibits high isotropy resulting in undercutting one can easily see in Figure 59 (a, b). Here, the photoresist (PMMA) has not been yet removed demonstrating the undercutting of the resist film. Another difficulty which was described by Daldosso et al. [132] is the low selectivity between $\text{SiO}_2/\text{Si}_3\text{N}_4$ during RIE. Moreover, with regard to the waveguide geometry (strip or buried channel structures) the obtained propagation losses are one order of magnitude larger for wet etched strip waveguides (about 2 dB/cm at 780 nm), because the guiding layer is directly exposed to the ambient material leading to enhanced scattering losses due to irregularities and/or defects on the top surface [132]. In the case of narrow waveguides (Figure 59 b, d) controlled etch parameters as plasma power or time and resists system are required. Vlasov and McNab [155] achieved small side wall surface roughness and minimal propagation and bending losses (3.6 ± 0.1 dB/cm) for SM SOI strip waveguides and bends with core cross-section of $445 \times 220 \text{ nm}^2$ at the telecommunications wavelength of $1.5 \mu\text{m}$ by RIE processing. Finally, it can be seen that RIE is a useful tool for waveguide structuring but must be improved due to the material system and geometry.

Therefore, the usage of specific plasma power for the RIE and an additional etching mask (Al) were added in further processing lines. Figure 60 (a, b) illustrates REM analysis of fabricated waveguides with core cross-sections of $1 \times 1 \mu\text{m}^2$ by photolithography and RIE with and without Al mask and different RIE parameters (E_{Plasma}).

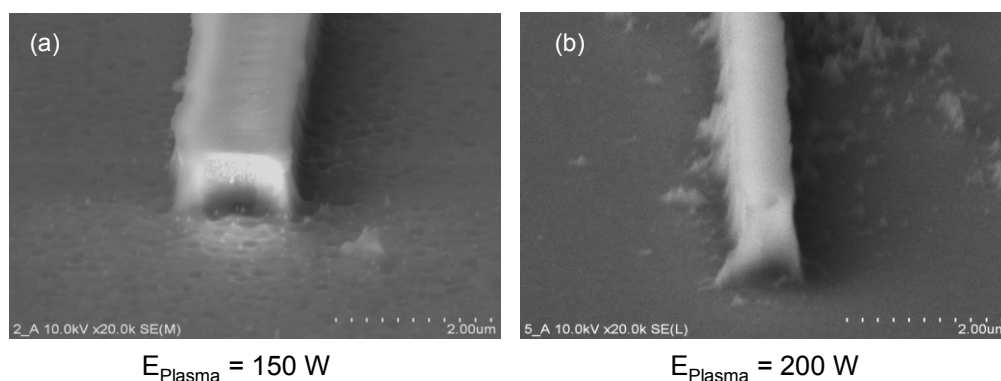


Figure 60: SM waveguides ($1 \times 1 \mu\text{m}^2$) based on a Si_3N_4 core and a $1 \mu\text{m}$ thick lower cladding fabricated by optical lithography and RIE; different plasma powers and with (a) / without (b) an Al etching masks

As is clearly apparent from the pictures above, an additional Al mask (Figure 60 (a)) enhances the quality of the fabricated waveguides by increasing the anisotropy of the RIE process. Moreover, an optimum plasma power (150 W, Figure 60 (a)) during dry etching leads to improved side and front walls of small structures. In comparison, Figure 60 (b) shows an evident undercutting and material loss due to higher plasma power.

In addition, Figure 61 (a – c) shows SEM pictures of free edge-overlapping strip waveguides fabricated by an alternative fabrication line based on photolithography and RIE (Figure 42 (a – f)).

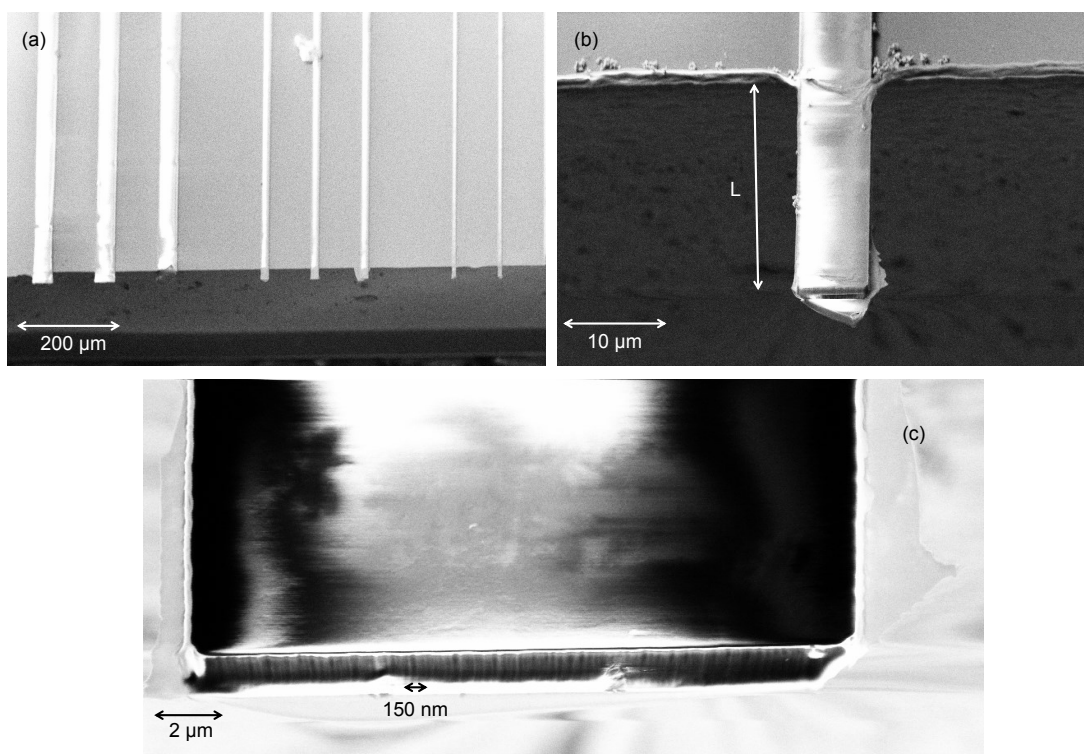


Figure 61: SEM picture of free edge-overlapping strip waveguides with an overlap of $25 \mu\text{m}$, (a) core dimensions of the trios: $w = 50, 20, 10 \mu\text{m}$, $h = 1 \mu\text{m}$ and $L = 25 \mu\text{m}$, (b) and (c) $1 \times 10 \mu\text{m}^2$

The observed structural results clearly demonstrate that the developed process pathway lead to waveguide structures with free standing front faces. The endface roughness is still too large ((c), ~ 150 nm) as well as some structures (b) show material residues from the etching process or incomplete endings (a, third waveguide). Nevertheless, the used fabrication line offers a strong potential for the manufacturing of novel waveguide structures which may improve the fiber-to-chip coupling situation. Transmission loss measurements of the waveguides are described at the end of this section.

However, as already discussed in chapter 5, if the structure dimensions are further decreased the resolution limit of photolithography will be reached. Thus, an alternative method, E-beam lithography, was chosen. The investigated fabrication recipe for optical devices in the submicrometer regime is depicted in Figure 43 (a – e) and an overview of developed strip waveguides are given in Figure 62 (a – d).

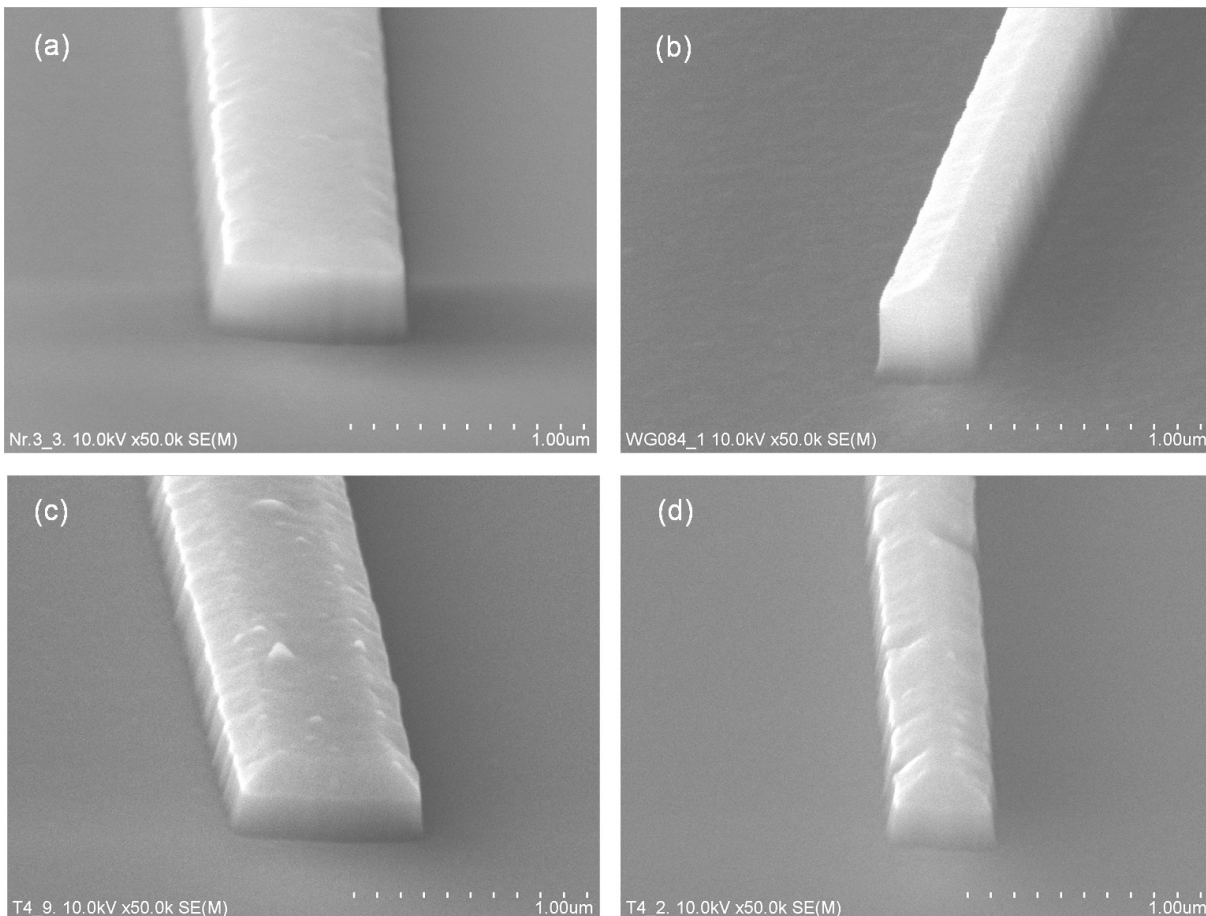


Figure 62: Straight waveguides fabricated by E-beam lithography and RIE (Al not removed); (a) $0.3 \times 0.8 \mu\text{m}^2$, (b) $0.3 \times 0.45 \mu\text{m}^2$, (c) $0.2 \times 0.8 \mu\text{m}^2$, (d) $0.2 \times 0.45 \mu\text{m}^2$

Besides the higher structural resolution obtained by E-beam lithography the side wall and surface roughness has been improved even for waveguides with cross-sections in the submicrometer range. The usage of an additional Al mask and an optimized RIE plasma power ($E_{\text{Plasma}} = 150$ W) due to previous studies was taken up again. As depicted above, the Al layer isn't removed yet which can be seen from the Al/Si₃N₄ interface in the REM pictures. Anyhow, the waveguides in Figure 62 (a, b) are based on a $0.3 \mu\text{m}$ thick core layer and widths less than $1 \mu\text{m}$. These as well as the even smaller structures in Figure 62 (c, d) show slanted side walls (see Table 8 for tilt angles) with an approximate roughness of 30 - 50 nm. In chapter 4 (Figure 32, 33) the effect of trapezoidal cross-sections on the vertical mode confinement was studied.

The mode field profiles have shown that the mode is still well confined and the optical properties of waveguides with tilt angles less than 90° correspond to those with rectangular shaped cross-sections [51, 52, 104]. Figure 63 (a – d) illustrates fabricated tapered and bended waveguides. Here, the side wall roughness represents again the limiting factor for propagation losses and the slanted front faces can be clearly seen.

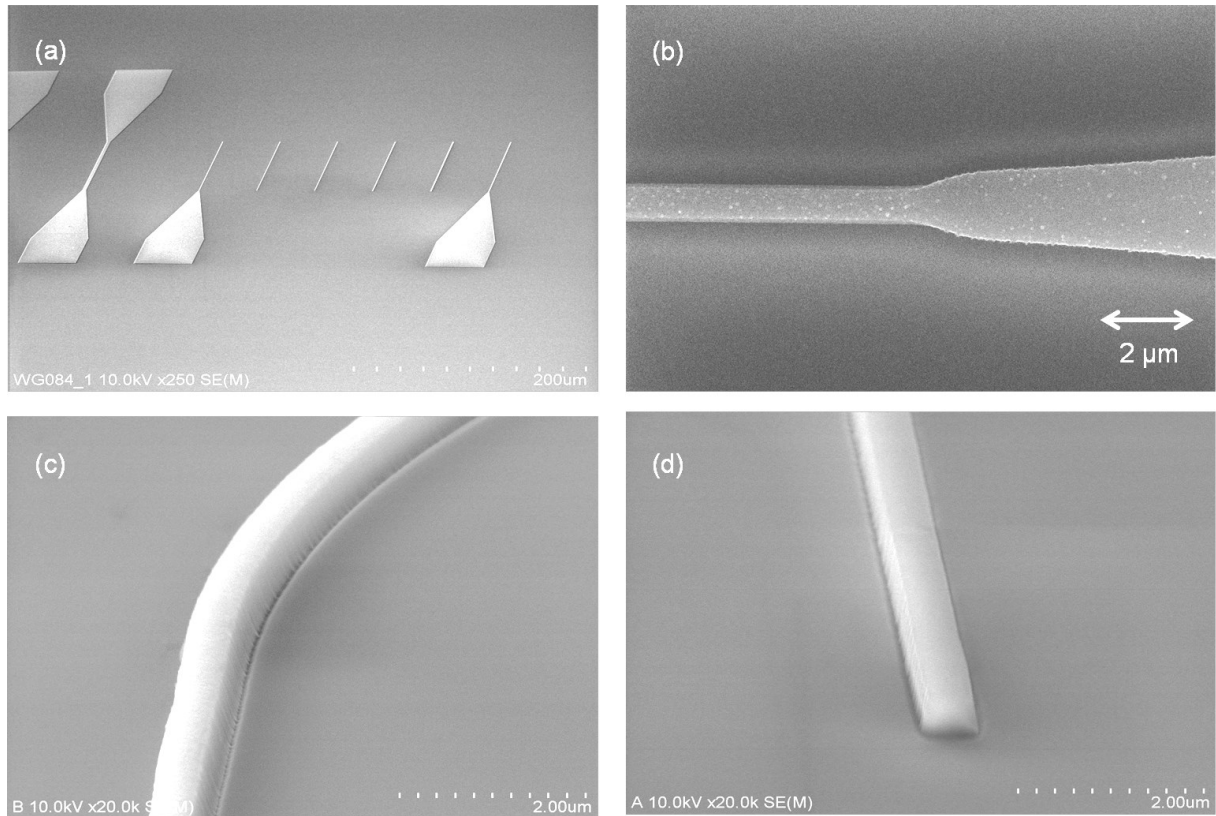


Figure 63: Tapered and bended waveguide with a cross-section of $0.5 \times 0.6 \mu\text{m}^2$; (b) tapered section, (c) curvature ($R = 10 \mu\text{m}$), (d) SM waveguide endface

Additionally, and as shown in the fabrication scheme (Figure 43 (e)), a polishing step of the waveguide fronts has been introduced. Despite the Fresnel reflection losses ((4), (5)) at both endfaces of the waveguide the FIB method significantly reduces the surface roughness leading to decreased interface scattering and coupling losses. Especially, end-fire or butt-coupling allow almost perpendicular incidence of the light to the front. Thus, for an air/ Si_3N_4 interface the reflection (49) is approximately 11 %, which introduces an additional loss of 0.56 dB/facet [34]. In order to further reduce coupling losses Figure 64 (a, b) shows that the chosen surface preparation technique produces sufficiently smooth facets so that the optical scattering is minimized.

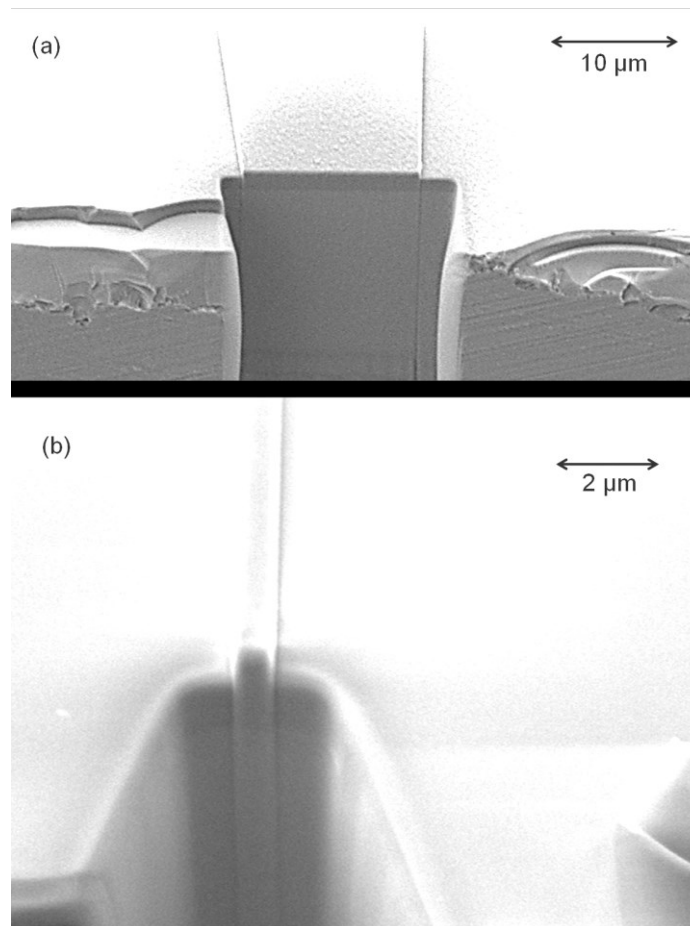


Figure 64: Smoothed waveguide fronts by FIB technique, (a) Taper ($0.5 \times 16 \mu\text{m}^2$), (b) SM waveguide ($0.5 \times 1 \mu\text{m}^2$)

Furthermore, besides straight SM/MM waveguides, tapered sections as well as bends the manufacturing of two-dimensional photonic crystals (PhC) by E-beam were carried out. As a result, in Figure 65 clearly demonstrates that more detailed experiences on E-beam lithography or other structuring method for the generation of well-defined very small features are required.

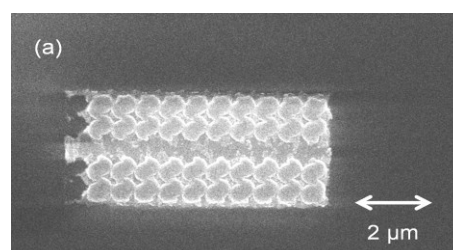


Figure 65: Processed two-dimensional PhC (after E-beam lithography) with $r = 0.4 \mu\text{m}$, $a = 0.9 \mu\text{m}$

In summary, the developed fabrication schemes (Figure 43, 41) led to well-structured straight and bended waveguides as well as tapers in the (sub)micrometer range. The RIE step needs improvement to achieve a further reduction of the surface and side wall roughness. In addition, other lithography techniques, e.g. UV-lithography, should be considered for the fabrication of two-dimensional PhC.

However, this work focuses on transmission loss characteristics of fabricated photonic structures as well as butt-coupled Si-based light emitters. Figure 66 (a, b) shows pictures of the investigated MM waveguide with free edge-overlapping endings and a cross-section of $1 \times 50 \mu\text{m}^2$. As can be seen in Figure 66 (a), before the transmission loss measurements were performed, a Helium-Neon laser ($\lambda = 632 \text{ nm}$) was used for the alignment of the fibers (setup in Figure 51). Afterwards, transmission spectra for TE and TM modes (Figure 66 (b)) were obtained by the usage of a tunable IR laser source (1490 nm – 1600 nm).

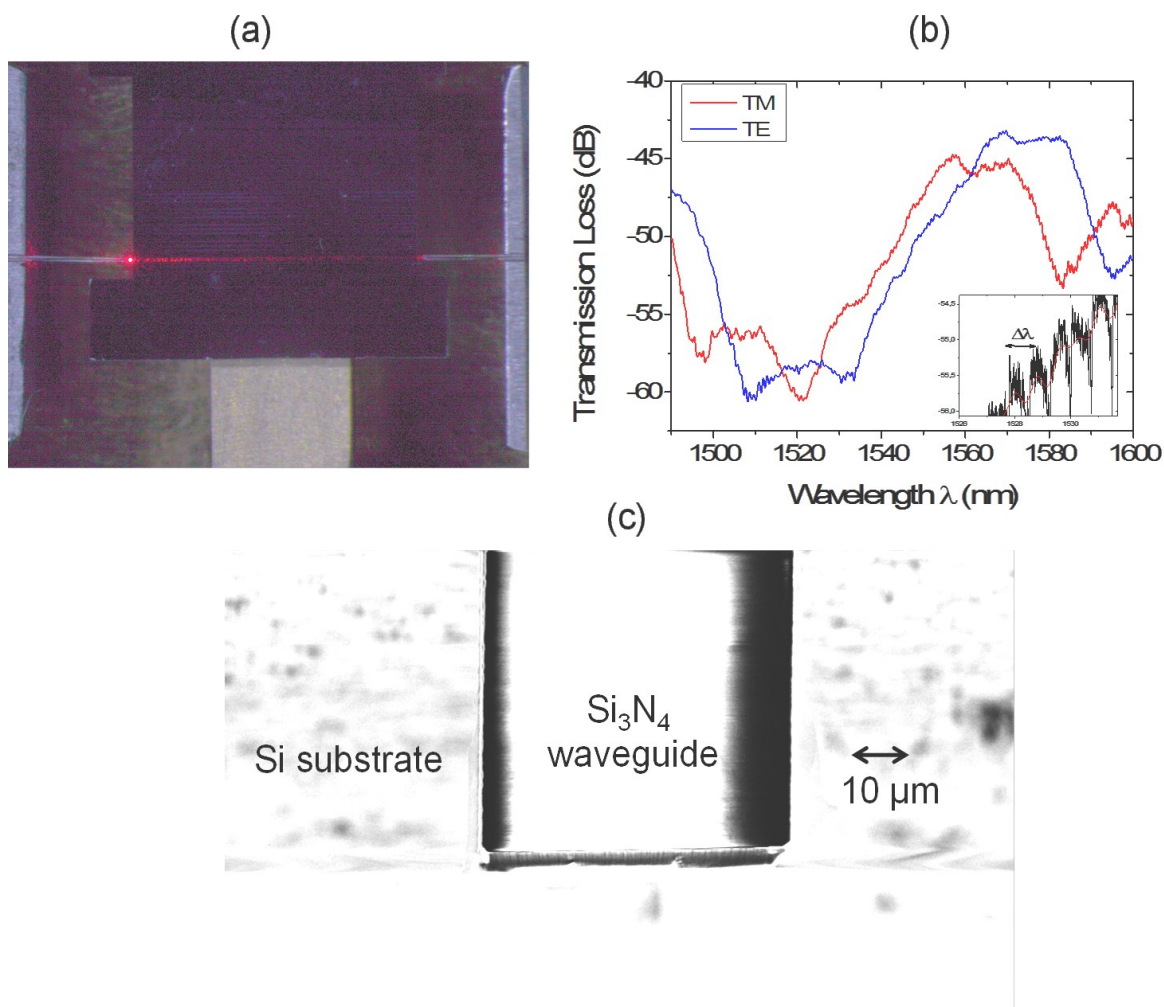


Figure 66: Measurement results of (c) a MM waveguide ($1 \times 50 \mu\text{m}^2$); (a) Laser light (632 nm) coupled into a fabricated MM waveguide, (b) Transmission loss characteristics between 1490 nm – 1600 nm (inset: non-smoothed signal, free spectral range $\Delta\lambda$)

The typical effective coupling efficiency for the chosen measurement setup and the coupling method is roughly 55 % [69] arriving from scattering losses by air/material interfaces as well as fiber connectors (insertion and return loss). Additionally, back scattering at the waveguide endfaces and modal dispersion due to MM propagation are resulting in signal noise. Therefore, signal smoothing of the obtained data was carried out, whereas the inset image in Figure 66 (b) illustrates the non-smoothed signal. The waveguide can be compared with a laser specified by a characteristic spacing, named as free spectral range ($\Delta\lambda$), between two successive reflected or transmitted optical intensity maxima or minima (standing waves) [71]. Anyhow, the measured transmission loss is given in dB, which is a logarithmic unit used to express the ratio between the in- and output intensity (61). The data is compared with a reference level (0 dB), while negative values correspond to intensity losses. Usually, a conversion of the measured damping

values into the attenuation coefficient α (dB/cm) (67) is used to make statements about the transmission losses per length. In the case of an Er:LED (1532 nm, 1545 nm) transmission coefficients of $\alpha = 68.13$ dB/cm, 62.0 dB/cm for the TM polarization and $\alpha = 73.5$ dB/cm, 65.1 dB/cm for the TE polarization were found. As explained in chapter 2.4 (Figure 16), Si-based waveguides and optical fibers show a characteristic low loss “window” at 1550 nm, thus Rayleigh scattering losses and OH-ion absorption losses can be excluded. Nevertheless, surface scattering losses due to the fabrication techniques are counting as the most important loss factor in semiconductor based photonic devices. In chapter 4.1.2.1, theoretically scattering values of 26.8 dB/cm were calculated. In the chosen model, SM operation and lower roughness value (rms = 10 nm) produce divergent results. However, interband and free carrier absorption can be neglected, because the Si excess of the guiding Si_3N_4 layer remained unchanged. Furthermore, radiation and dispersion losses (modal dispersion) caused by the dissipation of the energy of high-order modes and the energy exchange between low- and high-order modes can lead to the higher transmission losses in MM waveguides. Radiation losses into the Si substrate can be excluded by the significant thick SiO_2 box layer (1 μm) investigated in chapter 4.1.2.1. It should be taken into account, that the measured propagation losses exclude coupling losses. Nevertheless, the free edge-overlapping waveguides improved the alignment of the optical fibers and offered a promising alternative to conventional fiber-to-chip coupling methods. Yet, the used fabrication techniques must be improved in the future to take advantage of lower side wall and front face roughness of the waveguides in comparison to optimized structures of other groups [133, 135]. Thus, improved photonic devices can act as a connecting link between several on-chip or external optical and electrical components.

7.3 BUTT-COUPLED SI-BASED LIGHT EMITTERS

This study concentrates on the fabrication and characterization of monolithically integrated Si-based light emitting devices coupled with photonic structures. The connection of different optoelectronic components was facilitated by a specially developed fabrication scheme (Figure 44). The quality of the created waveguide structures as well as the electrical and optical properties of fabricated single Er/Tb: SiO_2 and Er/Tb: SiN_x LEDs have already been examined and discussed in chapter 7.1. and 7.2. This section deals with the transmission characteristics of the butt-coupled Si-based LEDs as shown in Figure 67 (a – c) due to the light guiding properties of the integrated waveguide and the RE-implanted light source.

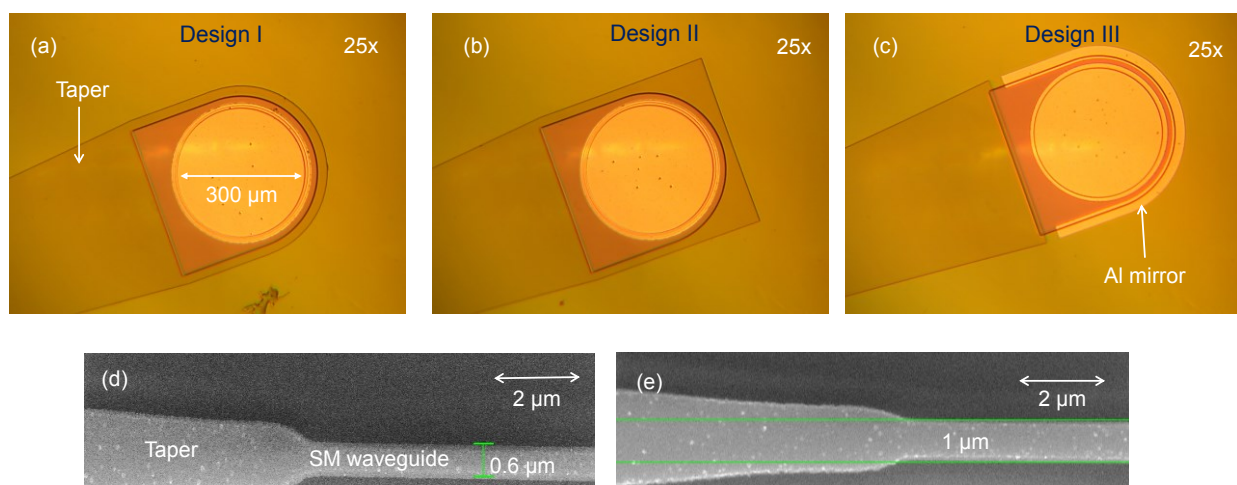


Figure 67: Butt-coupled Si-based LEDs; (a) embedded LED (round Si_3N_4 barrier), (b) embedded LED (square Si_3N_4 barrier), (c) Al mirror (30 μm), (d, e) tapered SM waveguides ($w = 0.6, 1 \mu\text{m}$, $\theta_T = 5.7^\circ$)

As can be seen from above, the invented fabrication pathway successfully results in monolithically integrated waveguide butt-coupled Si-LEDs. Furthermore, three different system geometries (I – III) have been developed for the optical interconnects between the light sources ($d = 300 \mu\text{m}$) and the waveguides. Figure 67 (a, b) illustrate LEDs which are fully embedded in Si_3N_4 -based tapers with round (I) or square (II) barriers. In comparison, Figure 67 (c) shows a butt-coupled LED surrounded with an additional $30 \mu\text{m}$ wide Al mirror (III) to increase the amount of coupled light into the connected waveguide. Additionally, tapered SM waveguides are depicted in Figure 67 (d, e) whereas the tapered sections have an angle around 5.7° . As already discussed in chapter 4, the length L_T (or angle θ_T) of the taper determine the energy transfer between two different sized devices and should not be too short, so that scattering and insertion losses do not get too large. However, the transmission characteristics of the presented structures have been measured by using the created setup as it is shown in chapter 6 (Figure 50).

The experiments of the waveguide butt-coupled LEDs based on Tb^{3+} -implanted (1.5 % RE) active SiO_2 layers with a down-tapered SM waveguide ($0.5 \times 0.6 \mu\text{m}^2$) disclosed two important facts. Firstly, a weak green vertical emission above the LEDs has been detected. Secondly, horizontal light emission of waveguide butt-coupled $\text{Tb}:\text{SiO}_2$ devices was measured. The observed EL spectra are illustrated in Figure 68 (a, b).

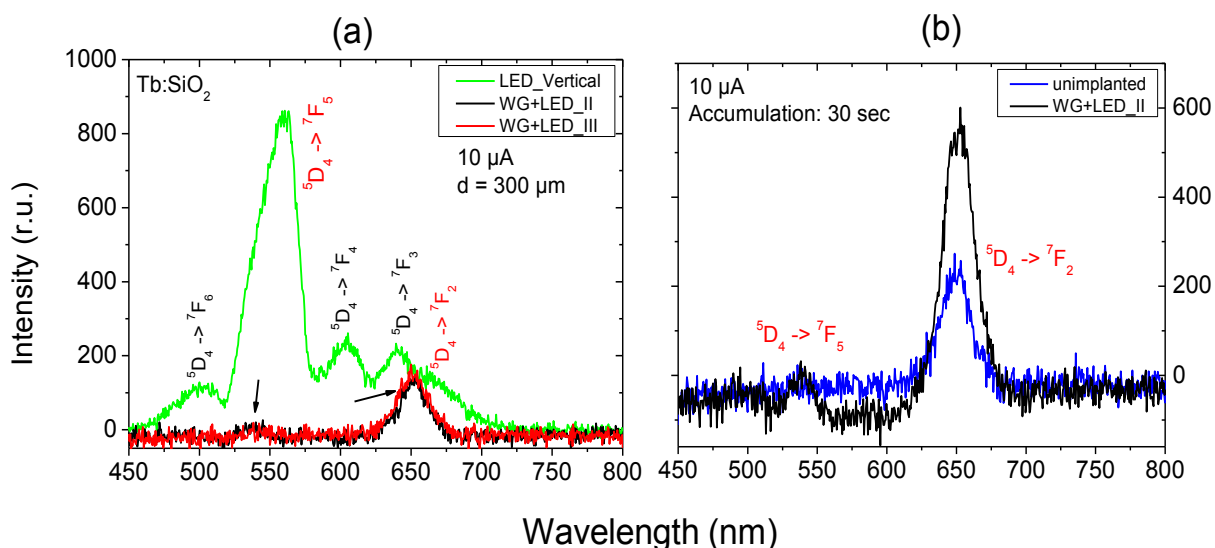


Figure 68: (a, b) EL spectra of measured vertical EL intensity of a $\text{Tb}:\text{SiO}_2$ LED (green) in comparison to waveguide-coupled $\text{Tb}:\text{SiO}_2$ LEDs (black: square Si_3N_4 barrier, red: Al mirror) and an unimplanted LED; dot diameter $d = 300 \mu\text{m}$

As can be seen from Figure 68 (a), the vertical detected emission lines of the $\text{Tb}:\text{SiO}_2$ LED (green) are red-shifted in comparison to the EL spectrum of a LED with a ITO top electrode (Figure 54). The cause for this is the dispersion when light is passing through several different layers. Anyhow, there are no recognizable differences of the measurement results of waveguide coupled LEDs with different designs. Both, the Si_3N_4 -embedded LED (II, black) as well as the device surrounded with an additional Al mirror (III, red), are showing a weak EL signal at $\lambda = 538 \text{ nm}$ and a stronger one at $\lambda = 650 \text{ nm}$. Therefore, the observed emission signals successfully prove the invented principle of waveguide butt-coupled Si-based LEDs.

In order to determine the origin of these emission lines, Figure 68 (b) depicts the horizontal detected transmission characteristics of a waveguide butt-coupled $\text{Tb}:\text{SiO}_2$ LED in contrast to

an unimplanted LED (100 nm SiO₂, 200 nm Si_yON_{2x}, x = 0.5). Firstly, it is obvious, that the unimplanted device does not show any EL signal at the peak position of $\lambda = 538$ nm, because this signal perfectly fits to the main Tb³⁺ transition (⁵D₄ - ⁷F₅) [128, 129]. According to the obtained low EL intensity of the peak it is not possible to make a concrete statement about the coupling efficiency between both devices. However, the coupling efficiency is undoubtedly below the theoretically assumed value in chapter 4.1.2.3 ($\eta_{\text{eff}} \sim 40$ %). However, an emission at $\lambda = 650$ nm was measured for both devices. In the case of the unimplanted sample the emission can clearly assigned to a Non Bridging Oxygen Hole Center (NBOHC) ($\equiv\text{Si}-\text{O}\cdot$) [156]. This is one of the most studied defects in amorphous silicon dioxide. Oxygen dangling bonds may be created by rupturing of the strained Si–O bonds ($\equiv\text{Si}\cdots\text{O}-\text{Si}\equiv$) in the silica network [156]. Furthermore, the same EL peak has been detected for the waveguide coupled Tb:SiO₂ sample. At the same wavelength, however, it should be noted that the Tb³⁺-ion shows an identically EL signal. Thus, the emission line at $\lambda = 650$ nm can either corresponds to the optical transition of a NBOHC or can be attributed to the ⁵D₄ - ⁷F₂ transition of the Tb³⁺-ion. Nevertheless, the waveguide coupled Tb:SiO₂ device shows a stronger EL intensity of the discussed signal in comparison to the unimplanted sample. Unfortunately, a clear distinction between both mechanisms could not be established, whereby a signal amplification caused by a higher number of defects generated during the implantation cannot be excluded [157].

In the case of developed waveguide coupled LEDs based on a Tb:SiN_x matrix (12 % Si excess) no vertical emission was detected. Generally, the integrated photonic circuits showed lower operation voltages (~ 23 V), but less operation life times and lower power efficiencies regarding to the lower EQE (0.1 %) [127]. Thus, only a few measurements results could be collected during this study. The EL spectrum of SM and MM waveguide butt-coupled LEDs (design III – Al mirror) is depicted in Figure 69.

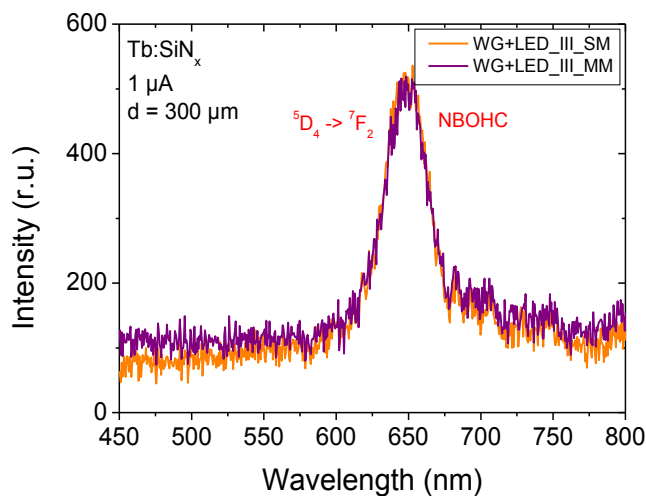


Figure 69: EL spectra of developed Tb:SiN_x LEDs with integrated SM (orange) or MM waveguides (violet)

As a result, no horizontal emission of the Tb³⁺-ion was measured in both samples, but the signal at $\lambda = 650$ nm was found once again independent of the sample design. Due to the fact that the EL intensity of this red light emission is similar whether or not there is a SM or MM waveguide connected the detected EL peak may corresponds to the optical transition of a NBOHC in SiN_x. In conclusion, the observed defect centres are not know beforehand, thus further studies about the optical transitions of the implanted ion due to the host material are required.

Fabricated Er³⁺-doped LEDs consisting of a SiO₂ or SiN_x (12 % Si excess) active layer with integrated waveguide structures have been also examined. Unfortunately, no signal in the IR

range could be measured which is due to the fact of the low EQE [127] of the SiN_x -system as well as the lower EL intensity of the Er^{3+} -transition between 1530 nm – 1560 nm. Generally, EL signals of Er^{3+} in the visible range are mostly suppressed in Si-based hosts [153]. Nevertheless, horizontal transmission measurements were performed and are illustrated in Figure 70 (a, b). As a result, the EL spectrum of a waveguide coupled $\text{Er}:\text{SiO}_2$ LED (red) shows an emission line at $\lambda = 650$ nm (Figure 70 (a)). This EL signal was also found and is shown for the unimplanted device (blue) as well as for a single Si-rich $\text{Er}:\text{SiO}_2$ (SRO, 12 % Si excess) LED (black). Here, the strongest emission was detected for the SRO sample, which has the same RE concentration (1.5 %) as the LEDs in the integrated photonic circuits apart from the Si excess of the SiO_2 . Thus, the higher amount of Si may lead to an increased defect formation during deposition and implantation resulting in an enhanced EL signal of the NBOHC [156, 157]. On the other hand, a weak EL peak of the investigated SRO $\text{Er}:\text{SiO}_2$ LED was detected at $\lambda = 515$ nm which might correspond to the ${}^2\text{H}_{11/2} \rightarrow {}^4\text{I}_{15/2}$ transition of the Er^{3+} -ion. Moreover, the unimplanted sample and the waveguide coupled LED show a similar EL intensity at $\lambda = 650$ nm. Overall, it is difficult to assess whether or not there is any light transmission of the $\text{Er}:\text{SiO}_2$ devices in the visible range. Thus, detailed statements about the coupling efficiency between the LED and the integrated waveguide are quite inadequate.

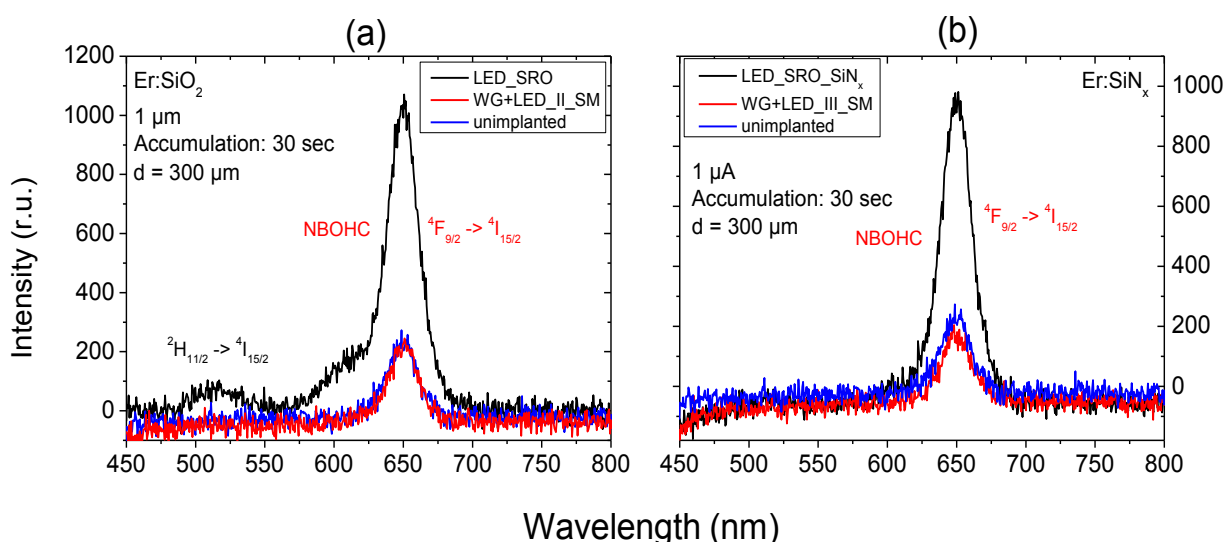


Figure 70: EL spectra of (a) waveguide coupled $\text{Er}:\text{SiO}_2$ and (b) $\text{Er}:\text{SiN}_x$ LEDs in comparison to Si-rich SiO_2 (SRO, 12 % Si excess), SRO/ SiN_x LED and unimplanted single LEDs

Figure 70 (b) illustrates the measured EL spectra of a waveguide coupled $\text{Er}:\text{SiN}_x$ LED (red, 12 % excess), a single $\text{Er}:\text{SiN}_x$ LED (black, SRO 12 % Si excess, SiN_x) and an unimplanted device (blue). Also here is obvious, the single $\text{Er}:\text{SiN}_x$ LED shows the strongest EL intensity at $\lambda = 650$ nm due to used SRO layer. Again, no difference of the observed EL intensity of the signal for the investigated unimplanted device and the integrated LED was discovered. It can be concluded from this, that the discussed emission line may corresponds to the NBOHC of the SiO_2 . Anyhow, in comparison to Figure 70 (a), no light emission in the green range of the spectrum was detected for all samples.

Summing up the experimental findings of this section, it becomes clear that the coupling principle between the integrated waveguide and the Si-based LED was successfully proven. The observed EL spectra demonstrate at least the following facts. Firstly, the $\text{Tb}:\text{SiO}_2$ systems, in contrast to the SiN_x -based active layers, show a weak EL signal at the main transition line of the Tb^{3+} -ion ($\lambda = 538$ nm). Secondly, lower intense vertical light transmission above the LED was detected in comparison to the devices with ITO top electrodes. Thirdly, an emission line in

the red region of the spectrum has been discovered which either corresponds to a further optical transition of Tb^{3+} or a NBOHC in SiO_2 . Fourthly, no signal in the infrared range was established for the Er^{3+} -doped systems caused by the low external EQE of the Er^{3+} implanted Si-based LEDs [127]. Nevertheless, transmission measurements between 450 nm – 800 nm lead again to the result that an emission at $\lambda = 650$ nm is either caused by an optical transition of Er^{3+} or initialized by the NBOHC. The above-mentioned facts led to the conclusion, that a fully monolithically integration and connection between both devices has been established. However, the obtained optical transmission clearly shows, that the $Tb:SiO_2$ LEDs are the most promising components regarding their power efficiency and observed EL intensity. Studies about the optical transition of defect centers of the implanted samples due to the host material are required in future. Optical leaks as the vertical emission of the Al top electrodes should be limited by an optimized LED design. The integration of an additional Al mirror was a good approach, but needs further improvement. Finally, the invented coupling method as well as the possibility of the usage of an alternative more efficient light source apart from the Si-based LED should be considered.

8 SUMMARY

8.1 REFLECTIONS

This study was conducted for the purpose of the design, fabrication and characterization of integrated optical waveguide structures and their coupling to Si-based light emitters for their application as potential biosensor components.

At the beginning, high-index-contrast strip waveguides, bends, two-dimensional PhC and tapers have been designed and theoretically analyzed regarding light propagation at $\lambda = 541$ nm and 1550 nm. The main focus was on their integration and coupling with Si-based LEDs, which should remain unchanged in their design. However, the LEDs differed concerning their RE implanted ions (Tb^{3+} , Er^{3+}) and active layers (SiO_2 , SiN_x), thus their related external power efficiency. The dielectric layer system of the devices may lead to a very narrow waveguiding layer resulting in light confinement and sideways propagation. The fabrication of single photonic structures in the (sub)micrometer range was established by the usage of standard CMOS technologies, e.g. E-beam lithography and RIE, and was further optimized. Secondly, it followed the development of a monolithically fabrication pathway for waveguide butt-coupled Si-based LEDs on a silicon substrate. Thirdly, and finally, optical loss characteristics of the fabricated photonic structures as well as the integrated photonic circuits were achieved by transmission loss measurement.

The main findings of this thesis are theoretical investigation and the design of Si_3N_4 strip waveguides based on a cross-section of $0.5 \times 1 \mu m^2$ to allow SM operation at $\lambda = 1550$ nm and resulting in high modal confinement (87 %). For light propagation in the visible range ($\lambda = 541$ nm) SM propagation is excluded if the core height is not further decreased. The obtained theoretical propagation losses for the lowest-order TE/TM mode are in a range of 0.3 - 1.3 dB/cm for an interface roughness of 1 nm. The lower SiO_2 waveguide cladding should be at least $1 \mu m$ to avoid substrate radiations. In the case of bended waveguides, an idealized device with a radius of $10 \mu m$ was developed which shows a reflection minimum ($S_{11} = -22$ dB) at $\lambda = 1550$ nm resulting in almost perfect transmission of the signal. Additionally, adiabatic down-tapered waveguides established an optimized light coupling between high-aspect-ratio devices. Moreover, fabrication lines including photo- and E-beam lithography and RIE with an Al mask were developed and lead to photonic structures in the (sub)micrometer range with surface roughness parameters of 10 nm – 20 nm. FIB milling was invented for smoother front faces of the waveguides. Additionally, an alternative fabrication pathway for first-time designed waveguides with free-edge overlapping endfaces was presented. Anyhow, the primary result of this work is the fabrication of monolithically integrated photonic circuits consisting of Si-based LEDs coupled to waveguides. Furthermore, by transmission loss measurements in the range of the telecommunication wavelength propagation loss coefficients of $\alpha \sim 65$ dB/cm of the free-edge overlapping MM waveguides were obtained. Electroluminescence measurements due to the implanted RE ions (Er^{3+} , Tb^{3+}) and the active layers (SiO_2 , SiN_x) of the waveguide butt-coupled Si-based LEDs discovered a weak emission signal at the main transition line of the Tb^{3+} -ion ($\lambda = 538$ nm). A second optical signal was detected in the red region of the spectrum either corresponding to a further optical transition of Tb^{3+} or a NBOHC in the SiO_2/SiN_x host material. No light emission in the infrared range was established for the Er^{3+} -doped systems. Transmission measurements between 450 nm – 800 nm lead again to the result that an emission at $\lambda = 650$ nm is either caused by an optical transition of Er^{3+} or initialized by the NBOHC again. Finally, successful coupling between the integrated waveguide and the Si-based LED was achieved, but no concrete statements about the coupling efficiency can be made, since the generation of the obtained EL signals is properly understood.

8.2 CONCLUSION

Pathogen microorganisms in food and drinking water are a real and increasing risk for human health, especially in view of internationalized automated food production with longer storage times and transport routes as well as by increased human mobility. For instance, since 2012 the quick on-site verification of pathogens as *Legionella* in drinking water pipes [2] or *Salmonella* in food [158] is becoming increasingly important and is strictly governed by the Federal Ministry of Health [159].

In this context, innovative label-free bioelectronic diagnostic systems are required for fast and flexible detection of pathogen microorganisms. Conventional biochemical tests are usually limited by the extensive enrichment cultivation of bacteria required prior to detection. New concepts and practical issues for accomplishing complete miniature sensor modules have been demonstrated [11 – 18]. Anyhow, the main drawback of optical biosensors relates to the unresolved manufacturability issues encountered when attempting monolithic integration of the light source and the detector [19, 20].

This fact implies the motivation of this study regarding the design and fabrication of a photonic circuit based on a Si-based light emitter and an integrated waveguide. The above-mentioned results regarding the interface roughness and transmission losses of the fabricated (sub)micrometer scaled waveguides clearly show the improvement potential of the fabrication processes. Nevertheless, FIB milling represents an innovative polishing method for waveguides endfaces. An alternative manufacturing pathway for novel designed waveguides with free-edge overlapping endfaces offers a strong potential for an enhanced fiber-chip coupling. The main finding of this work is the first-time implementation of fully monolithically integrated waveguide butt-coupled Si-based LEDs enabled through standard CMOS fabrication technologies on a single chip. As it is clear from the results, the ion implanted active layer of the LED may represent a narrow waveguiding layer for light confinement and sideways propagation. A reduction of optical leaks as the vertical emission of the Al top electrodes and an improved design of the integrated Al mirror are starting points for further photonic circuits. The experimental studies clearly showed that the coupling principle between the two devices is successfully proven, but investigations of the defect centers due to the implanted ions and the host materials are required for concrete statements about the coupling efficiency. In contrast, the usage of a more efficient light source, e.g. laser diode, should be taken into account with respect to the unsuccessful results for the system performance in the infrared range. Moreover, considerations should also be given to introducing alternative coupling methods, e.g. grating coupling that could lead to an improved system operation.

Finally, the presented integrated photonic circuit shows, on the one hand, the necessary procedure for the design of several system components as well as coupling concepts, and on the other hand, the possibility of fabrication of lab-on-chip systems via standard CMOS technologies. This clearly demonstrates the high potential of fundamental cross-innovations between biotechnology and microelectronics for life science and health care applications.

9 FUTURE PROSPECTS

The current studies also raised many important issues that should be considered in future research. Besides the improvement of the presented fabrication processes alternative technologies, e.g. UV- or ion-beam lithography could be used. The design and material characteristics as well as the power efficiency of the selected system components should be better analyzed and optimized beforehand. Moreover, for the achievement of a high coupling efficiency and a powerful throughput the Si-based LED should be rethought from scratch regarding the implementation in an integrated photonic circuit. It would surely be more advisable to utilize a laser diode, but this would result in a more complicated monolithically integration process apart from bonding techniques. Furthermore, alternative coupling concepts, as the usage of integrated gratings, demonstrate another possibility to increase the coupling efficiency between both devices further. Ultimately, the design and used fabrication technologies of the sensor components depend on a number of factors, especially on the application field and systems requirements of the lab-on-chip system.

10 LIST OF LITERATURE

- [1] "Sensormagazin," 1 10 2010. [Online]. Available: <http://www.sensormag.com/specialty-markets/medical/strong-growth-predicted-biosensors-market-7640>.
- [2] "LVZ Online," 21 8 2013. [Online]. Available: <http://www.lvz-online.de/leipzig/citynews/legionellen-fund-in-leipzig--behoerde-raet-zur-ruhe--geringer-wasserverbrauch-foerdert-keim/r-citynews-a-202687.html>.
- [3] C. Cherkouk, L. Rebohle, S. Howitz and W. Skorupa, "Microfluidic system for endocrine disrupting chemicals detection in waterish solution," *Procedia Engineering*, no. **25**, pp. 1185-118, 2011.
- [4] L. Rebohle, C. Cherkouk, S. Prucnal, M. Helm and W. Skorupa, "Rare-earth implanted Si-based light emitters and their use for smart biosensor applications," *Vacuum*, no. **83**, pp. 524-528, 2009.
- [5] L. Rebohle, T. Gebel, R. T. Yankov, T. Trautmann, W. Skorupa, J. Sun, G. Gauglitz and G. Frank, "Microarrays of silicon-based light emitters for novel biosensor and lab-on-chip-applications," *Optical Materials*, no. **27**, pp. 1055-1058, 2009.
- [6] R. G. Hunsperger, A. Yariv and A. Lee, "Parallel end-butt coupling for optical integrated circuits," *Applied Optics*, no. **16**, pp. 1026-1032, 1977.
- [7] M. Ramuz, L. Bürgi, R. Stanley and C. Winnewisser, "Coupling light from an organic light emitting diode (OLED) into a single-mode waveguide: Toward monolithically optical sensors," *J. Appl. Phys.*, no. **105**, p. 084508, 2009.
- [8] R. E. Kunz, "Miniature integrated optical modules for chemical and biochemical sensing," *Sensors and Actuators B*, no. **38-39**, pp. 13-28, 1997.
- [9] S. Feng, Y. Geng, K. M. Lau and A. W. Poon, "Epitaxial III-V-on-silicon waveguide butt-coupled photodetectors," *Optical Letters*, no. **37**, pp. 4035-4037, 2012.
- [10] J. Kubby and G. T. Reed, in *SPIE Silicon Photonics VIII*, S.F., California, USA, 2013.
- [11] R. Slavik, J. Homola and J. Ctyroky, "Single-mode optical fiber surface plasmon

- resonance sensor," *Sensors and Actuators B*, no. **54**, pp. 74-79, 1999.
- [12] R. J. Walters, R. V. A. van Loon, I. Brunets, J. Schmitz and A. Polman, "A silicon-based electrical source of surface plasmon polaritons," *Nature Materials*, no. **9**, pp. 21-25, 2010.
- [13] C. R. Lavers and J. S. Wilkinson, "A waveguide-coupled surface plasmon sensor for an aqueous environment," *Sensors and Actuators B*, no. **22**, pp. 75-81, 1994.
- [14] T. Mappes, C. Vannahme, M. Schelb, U. Lemmer and J. Mohr, "Design for optimized coupling of organic semiconductor laser light into polymer waveguides for highly integrated biophotonic sensors," *Microelectronic Engineering*, no. **86**, pp. 1499-1501, 2009.
- [15] N. Daldosso, D. Navarro-Urrios, M. Melchiorri, C. Garcia, P. Pellegrino, B. Garrido, C. Sada, G. Battaglin, F. Gourbilleau, R. Rizk and L. Pavesi, "Er-Coupled Si Nanocluster Waveguide," *Journal of Selected Quantum Electronics*, no. **6**, pp. 1607-1617, 2006.
- [16] J. Dostálek, J. Čtyroký, J. Homola, E. Brynda, M. Skalský, P. Nekvindová, J. Špirková, J. Škvor and J. Schröfel, "Surface plasmon resonance biosensor based on integrated optical waveguide," *Sensors and Actuators B*, no. **76**, pp. 8-12, 2001.
- [17] R. J. Welty, T. C. Bond, E. Behymer and M. Pocha, "Integrated laser with low-loss high index-contrast waveguides for OEIC," in *International Symposium on Integrated Optoelectronic Devices (SPIE)*, San Jose, CA, United States, 2005.
- [18] J. Ozhikandathil and M. Packirisamy, "Silica-on-silicon waveguide integrated polydimethylsiloxane lab-on-a-chip for quantum dot fluorescence bio-detection," *J. Biomed. Opt.*, no. **17**, p. 017006, 2012.
- [19] S. Rodriguez, S. Reder, M. L. de Alda, G. Gauglitz and D. Barceló, "Biosensors for environmental monitoring of endocrine disruptors: a review article," *Biosens Bioelectron.*, no. **19**, pp. 633-640, 2004.
- [20] J. Tschmelak, "Automated water analyser computer supported system (AWACSS) Part I: Project objectives, basic technology, immunoassay development, software design and networking," *Biosensors and Bioelectronics*, pp. 1499-1508, 2005.
- [21] J. T. Kim and S.-Y. Choi, "Graphene-based plasmonic waveguides for photonic integrated

- circuits," *Optics Express*, no. **19**, pp. 24557-24562, 2011.
- [22] C. Lamprecht, A. Tschupp, M. Čajlaković, M. Sagmeister, V. Ribitsch and S. Köstler, "A luminescence lifetime-based capillary oxygen sensor utilizing monolithically integrated organic photodiodes," *Analyst*, no. **138**, pp. 5875-5878, 2013.
- [23] P. Ma, D.-Y. Choi, Y. Yu, X. Gai, Z. Yang, S. Debbarma, S. Madden and B. Luther-Davies, "Low-loss chalcogenide waveguides for chemical sensing in the mid-infrared," *Optics Express*, no. **21**, pp. 29927-29937, 2013.
- [24] J. M. Sun, L. Rebohle, S. Prucnal, M. Helm and W. Skorupa, "Giant stability enhancement of rare-earth implanted SiO₂ light emitting devices by an additional SiON protection layer," *Appl. Phys. Lett.*, no. **92**, p. 071103, 2008.
- [25] D. G. Hall, "Survey of Silicon-Based Integrated Optics," *Computer*, no. 20, pp. 25-32, 1987.
- [26] R. Shubert and J. H. Harris, "Optical Surface Waves on Thin Films and Their Application to Integrated Data Processors," *Trans. on Microwave Theory and Technology*, pp. 1048-1054, 1968.
- [27] S. Valette, S. Renard, J. P. Jadot, P. Gidon and C. Erbeia, "Silicon-based integrated optics technology for optical sensor applications," *Sensors and Actuators A21-A23*, pp. 1087-1091, 1990.
- [28] S. Anthony, "Extreme Tech," 10 December 2012. [Online]. Available: <http://www.extremetech.com/computing/142881-ibm-creates-first-cheap-commercially-viable-silicon-nanophotonic-chip>.
- [29] P. Hua, J. Hole, J. Wilkinson, G. Proll, J. Tschmelak, G. Gauglitz, M. Jackson, R. Nudd, H. Griffith, R. Abuknesha, J. Kaiser and K. P., "Integrated optical fluorescence multisensor for water pollution," *Opt. Express*, no. **13**, pp. 1124-1130, 2005.
- [30] T. Okamoto, M. Yamamoto and I. Yamaguchi, "Optical waveguide absorption sensor using a single coupling prism," *Journal of the Optical Society of America A*, no. **17**, pp. 1880-1886, 2000.
- [31] C. Barrios, "Optical Slot-Waveguide Based Biochemical Sensors," *Sensors*, no. **9**, pp.

- 4751-4765, 2009.
- [32] T. May, T. Abel, B. Enko, S. Borisov, C. Konrad, S. Köstler, B. Lamprecht, S. Sax, E. J. W. List and I. Klimant, "A planar waveguide optical sensor employing simple light coupling," *Analyst*, no. **134**, pp. 1544-1547, 2009.
- [33] H. Mukundan, A. S. Anderson, W. K. Grace and K. M. Grace, "Waveguide-Based Biosensors for Pathogen Detection," *Sensors*, no. **9**, pp. 5783-5809, 2009.
- [34] G. T. Reed, *Silicon Photonics: The State of the Art*, John Wiley & Sons, Ltd, 2008.
- [35] L. Pavesi and G. Guillot, *Optical Interconnects*, Springer, 2006.
- [36] W. Lukosz and K. Tiefenthaler, "Directional Switching in Planar Waveguides Effected by Absorbtion-Desorbtion Processes," in *Institution of Electrical Engineers, 2nd European Conference of Integrated Optics*, Florence, Italy, 1983.
- [37] Z. Gu, "Towards two-dimensional optics," Diplomarbeit, Leiden Universiy, 2009.
- [38] R. Paschotta, "RP Photonics Encyclopedia," [Online]. Available: http://www.rp-photonics.com/numerical_aperture.html.
- [39] N. J. Cronin, *Microwave and Optical Waveguides*, Taylor & Francis, 1995.
- [40] "Wikipedia," [Online]. Available: http://en.wikipedia.org/wiki/Evanescent_wave.
- [41] B. West, "Wilfrid Laurier University," 2013. [Online]. Available: https://www.wlu.ca/page.php?grp_id=2590&p=15978.
- [42] W. Bogaerts, R. Baets, P. Dumon, V. Wiaux, S. Beckx and D. Taillaert, "Nanophotonic Waveguides in Silicon-on-Insulator Fabricated With CMOS Technology," *Journal of Lightwave Technology*, no. **23**, pp. 401-412, 2005.
- [43] C. Sibilia, T. Benson and M. Marciniak, *Photonic Crystals: Physics and Technology*, Italien: Springer, 2008.
- [44] G. Lifante, *Integrated Photonics: Fundamentals*, England: Wiley, 2003.
- [45] P. Donohoe, "Mississippi State University," [Online]. Available:

<http://www.ece.msstate.edu/~donohoe/>.

- [46] J.-M. Liu, *Photonic Devices*, Cambridge University Press, 2005.
- [47] M. Marcuvitz, *Waveguide Handbook*, UK: Peter Peregrinus Ltd., 1993.
- [48] F. Ladouceur, J. D. Love and T. Senden, "Effect of side wall roughness in buried channel waveguides," *IEEE Proc. Optoelectron.*, no. 141, pp. 242-248, 1994.
- [49] K. Lee, D. Lim, C. S. J. Kimerling and F. Cerrina, "Fabrication of ultralow-loss Si/SiO₂ waveguides by roughness reduction," *Optics Letters*, no. **26**, pp. 1888-1890, 2001.
- [50] C. Poulton, C. Koos, M. Fujii, A. Pfrang, T. Schimmel, L. J. and W. Freude, "Radiation Modes and Roughness Loss in High Index-Contrast Waveguides," *IEEE Journal of selected Topics in Quantum Electronics*, no. **12**, pp. 1306-1321, 2006.
- [51] E. Popescu and S. Song, "Trapezoidal waveguides: first-order propagation equivalence with rectangular waveguides," *J. Phys. A: Math. Theor.*, no. **40**, pp. 14555-14574, 2007.
- [52] D. Clark and I. Dunlop, "Method for analysing trapezoidal optical waveguides by an equivalent rectangular rib waveguide," *Electronics Letters*, no. **24**, pp. 1414 - 1415, 1988.
- [53] W. Ye, "Stress engineering for polarization control in Silicon-on-Insulator waveguides and its applications in novel passive polarization splitters/filter," Carleton University, Canada, 2006.
- [54] W. Bogaerts and S. Selvaraja, "Compact Single-Mode Silicon Hybrid Rib/Strip Waveguide With Adiabatic Bends," *IEEE Photonics Journal*, no. **3**, 2011.
- [55] A. Melloni, F. Carniel, R. Costa and M. Martinelli, "Determination of Bend Mode Characteristics in Dielectric Waveguides," *Journal of Lightwave Technology*, no. **19**, pp. 571-77, 2001.
- [56] K. Sakoda, *Optical Properties of Photonic Crystals*, Springer-Verlag Berlin Heidelberg, 2001.
- [57] N. Nuesse, "Hybridstrukturen aus Nanodiamanten, nanoplasmonischen Elementen und photonischen Kristallen," TUB, Berlin, 2011.

- [58] S. Johnson and J. Joannopoulos, "Introduction to Photonic Crystals: Bloch's Theorem, Band Diagrams, and Gaps (But No Defects)," MIT, 2003.
- [59] E. Yablonovitch, "Inhibited spontaneous emission in solid-state physics and electronics," *Phys. Rev. Lett.*, no. **20**, pp. 2059-2062, 1987.
- [60] S. John, "Strong localization of photons in certain disordered dielectric superlattices," *Phys. Rev. Lett.*, no. **58**, pp. 2486-2489, 1987.
- [61] A. Gomyo, J. Ushida and M. Shirane, "Highly drop-efficient channel-drop optical filters with Si-based photonic crystal slabs," *Thin Solid Films*, no. **508**, pp. 422-425, 2006.
- [62] H. Chien, C. Chen and P. Luan, "Photonic crystal beam splitters," *Optics Communications*, no. **259**, pp. 873-875, 2006.
- [63] P. B. Xing, L. Frandsen, A. Harpøth and M. Kristensen, "Optimization of bandwidth in 60° photonic crystal waveguide bends," *Optics Communications*, no. **248**, pp. 179-184, 2005.
- [64] M. Y. T. Loncar, A. Scherer, P. Gogna and Y. Qiu, "Low-threshold photonic crystal laser," *App. Phy. Lett.*, no. **81**, pp. 2680-2682, 2002.
- [65] J. Joannopoulos, R. Meade and J. Winn, *Photonic Crystals*, Princeton: Princeton University Press, 1995.
- [66] S. Johnson, "The Joannopoulos Research Group at MIT," 2000. [Online]. Available: <http://ab-initio.mit.edu/photons/tutorial/L2-defects.pdf>.
- [67] P. Kramper, "Mikroskopie und Spektroskopie an photonischen Kristallen: Einschluss von Licht auf Subwellenlängen-Bereiche," Universität Konstanz, 2002.
- [68] E. Palen, "Optical coupling to monolithic integrated photonic circuits," in *Photonics Packaging, Integration, and Interconnects VII*, San Jose, California, USA, 2007.
- [69] R. G. Hunsperger, *Integrated Optics: Theory and Technology*, New York, USA: Springer, 2009.
- [70] J. Reinhard, "Volpi - Grundlagen der Faseroptik," 2000. [Online]. Available: <http://www.volpi.ch/>.

- [71] R. Quimby, *Photonics and Lasers: An Introduction*, New Jersey: John Wiley & Sons., 2006.
- [72] I. Moermann, P. Van Daele and P. Demeester, "A review on fabrication technologies for the monolithic integration of tapers with III-V semiconductor devices," *Selected topics in Quantum Electronics*, no. **3**, 1997.
- [73] A. Hosseini, J. Covey, D. N. Kwong and R. Chen, "Mode Order Converter Using Tapered Multi-mode Interference Couplers," *Journal of Optics*, no. **12**, p. 075502, 2010.
- [74] A. Nelson, "Coupling optical waveguides by tapers," *Applied Optics*, no. **14**, pp. 3012-3015, 1975.
- [75] A. Barkai, L. Ansheng, K. Daewoong and R. Cohen, "Efficient Mode Converter for Coupling between Fiber and Micrometer Size Silicon Waveguides," in *4th IEEE International Conference on Photonics*, Tokyo, 2007.
- [76] D. Dai and J. Bowers, "Novel concept for ultracompact polarization splitter-rotator based on silicon nanowires," *Opt. Express*, no. **19**, pp. 10940-10949, 2011.
- [77] J. Galán, P. Sanchis and J. Martí, "Low-loss coupling technique between SOI waveguides and standard single-mode fibers," in *European Conference on Integrated Optics*, Copenhagen, 2007.
- [78] D. Dai, Y. Tang and J. Bowers, "Mode conversion in tapered submicron silicon ridge optical waveguides," *Optics Express*, no. **20**, pp. 13425-13439, 2012.
- [79] K. Mertens, M. Sennewald and J. Schmitt, "Polarization conversion by hybrid modes: Theory and applications," *Radio Science*, no. **31**, pp. 1773-1779, 1996.
- [80] A. Hosseini, J. Covey, D. Kwong and R. Chen, "Tapered multi-mode interference couplers for high order mode power extraction," *Journal of Optics*, no. **12**, 2010.
- [81] T. Lim, B. Garside and J. Marton, "An Analysis of Optical Waveguide Tapers," *Appl. Phys.*, no. **18**, pp. 53-62, 1979.
- [82] A. Boudrioua, *Photonic Waveguides: Theory and Applications*, Frankreich: Hermes Science/Lavoisier, 2006.

- [83] P. Tien, "Light Waves in Thin Films and Integrated Optics," *Appl. Opt.*, no. **10**, pp. 2395-2413, 1971.
- [84] K. Yap, A. L. J. Delage and S. Janz, "Correlation of Scattering Loss, Sidewall Roughness and Waveguide Width in Silicon-on-Insulator (SOI) Ridge Waveguides," *Journal of Lightwave Technology*, no. **27**, pp. 3999-4008, 2009.
- [85] A. Mrotzek, "Struktur und optoelektronische Eigenschaften von siliziumreichen SiO₂- und Si₃N₄-Schichten für MOS- und Wellenleiterstrukturen," Westsächsische Hochschule Zwickau, Zwickau, 2013.
- [86] R. Soref and J. Lorenzo, "All-silicon active and passive guided wave components for $\lambda=1.3$ and $1.6\mu\text{m}$," *IEEE Journal of Quantum Electronics*, no. **22**, pp. 873-879, 1986.
- [87] S. Miller, *Bel Syst. Tech. J.*, no. **43**, p. 1727, 1964.
- [88] J. Goell, "Loss mechanisms in dielectric waveguides," in *Introduction to Integrated Optics*, New York, Plenum, 1974, p. 118.
- [89] I. Redbooks, Understanding Optical Communications, IBM Corporation, 1998.
- [90] D. Gill, "Fabrication and characterisation of thin film optical waveguides by pulsed laser deposition," University of Southampton, 1996.
- [91] DBNCST, "Data Base for Noteworthy Contributions for Science and Technology (Japan)," 2010. [Online]. Available: <http://dbnst.nii.ac.jp/english/detail/931>. [Accessed 2014].
- [92] O. Gili de Villasante, "Design and Simulation of Vertical Grating Coupler for Photonic Integrated System-in-Package," Universitat Politècnica de Catalunya, Master Thesis, 2010.
- [93] W. Tsai, S. Ting and P. Wei, "Refractive index profiling of an optical waveguide from the determination of the effective index with measured differential fields," *Optics Express*, no. **20**, pp. 26766-26777, 2012.
- [94] J. Jin, The finite element method in electromagnetics, New York: Wiley, 2002.
- [95] Q. Wang, D. Ng, J. Pu and S. Ho, "Heterogeneous Si/III-V integration and the optical

- vertical interconnect access," *Optic Express*, no. **15**, pp. 16745-16756, 2012.
- [96] E. Marcatili, "Dielectric rectangular waveguides and directional couplers for integrated optics," *Bell Syst. Tech. J.*, no. **48**, pp. 2071-2102, 1969.
- [97] D. Siong, "Device Integration for Silicon Microphotonic Platforms," PhD Thesis, MIT, 2000.
- [98] K. Lee, "Transmission and routing of optical signals in on-chip waveguide for silicon microphotronics," MIT, PhD Thesis, 2001.
- [99] H. Zmuda, "Zmuda Course Pages, University of Florida," 2012. [Online]. Available: http://www.zmuda.ece.ufl.edu/Photonics/2b_Rectangular_Waveguide.pdf.
- [100] M. Golio, *Microwave and RF Product Applications*, Florida: CRC Press, 2001.
- [101] H. Srinivasan, "Finite Element Analysis and Experimental Verification of SOI Waveguides," University of Kentucky, PhD Thesis, 2007.
- [102] T. Li, "Complex Mode Calculation by Finite Element Method," McMaster University, Master Thesis, 2012.
- [103] S. Sridaran and S. Bhave, "Nanophotonic devices on thin buried oxide SOI substrates," *Optics Express*, no. **18**, pp. 3850-3857, 2010.
- [104] C. Xiong, W. Pernice, K. Ryu, C. Schuck and K. Fong, "Integrated GaN photonic circuits on silicon (100) for second harmonic generation," *Optics Express*, no. **19**, pp. 10462-10470, 2011.
- [105] L. Stern, B. Desiatov, I. Goykhman and U. Levy, "Nanoscale light-matter interactions in atomic cladding waveguides," *nature communications*, 2013.
- [106] I. Goykhman, B. Desiatov, J. Khurgin, J. Shappir and U. Levy, "Waveguide based compact silicon Schottky photodetector with enhanced responsivity in the telecom spectral band," *Optics Express*, no. **20**, pp. 28594-28602, 2012.
- [107] R. Kou, H. Nishi, T. Tsuchizawa, H. Fukuda, H. Shinojima and K. Yamada, "Single silicon wire waveguide based delay line interferometer for DPSK demodulation," *Optics Express*, no. **20**, pp. 11037-11045, 2012.

- [108] A. Washburn and R. Bailey, "Photonics-on-a-Chip: Recent Advances in Integrated Waveguides as Enabling Detection Elements of Real-World, Lab-on-a-Chip Biosensing Applications," *Analyst*, no. **136**, p. 227–236, 2011.
- [109] K. Schmitt, K. Oehse, G. Sulz and C. Hoffmann, "Evanescent field Sensors Based on Tantalum Pentoxide Waveguides – A Review," *Sensors*, no. **8**, pp. 711-738, 2008.
- [110] A. Selle, C. Kappel, M. Bader, G. Marowsky, K. Winkler and U. Alexie, "Picosecond-pulse-induced two-photon fluorescence enhancement in biological material by application of grating waveguide structures," *Optics Letters*, no. **30**, pp. 1683-1685, 2005.
- [111] B. You, J.-Y. Lu, T.-A. Liu and J.-L. Peng, "Hybrid terahertz plasmonic waveguide for sensing applications," *Optics Express*, no. **21**, pp. 21087-21096, 2013.
- [112] K. Cottier, "A polymer waveguide grating sensor Based on Integrated Optical Waveguide Gratings," Univeriste de Neuchatel, PhD Thesis, 2004.
- [113] F. Song, J. Xiao, A. Xie and S.-W. Seo, "A polymer waveguide grating sensor integrated with a thinfilm photodetector," *Journal of Optics*, no. **16**, 2014.
- [114] S.-H. Hsu, "Reflectively Coupled Waveguide Photodetector for High Speed Optical Interconnection," *Sensors*, no. **10**, pp. 10863-10875, 2010.
- [115] D. Ahn, L. Kimerling and J. Michel, "Evanescent Coupling Device Design for Waveguide-Integrated Group IV Photodetectors," *Journal of Lightwave Technology*, no. **28**, pp. 3387-3394, 2010.
- [116] J. Soole, Y. Silberberg, A. Scherer, H. S. H. LeBlanc and U. Erben, "Fast high-efficiency integrated waveguide photodetectors using novel hybrid vertical/butt coupling geometry," *Applied Physics Letters*, no. **61**, 1992.
- [117] N. Harris, "Fabrication, Design and Noise Analysis of a High-Gain Waveguide-Coupled Photoconductive Detector," University of Washington, Master Thesis, 2012.
- [118] S.-Q. Liu, X.-H. Yang, Y. Liu, B. Li and Q. Han, "Design and fabrication of a high-performance evanescently coupled waveguide photodetector," *Chin. Phys. B*, no. **22**, pp. 108503-108508, 2013.

- [119] H. Park, A. Fang, R. Jones, O. Cohen, O. Raday, M. Sysak, M. Paniccia and J. Bowers, "A hybrid AlGaInAs-silicon evanescent waveguide photodetector," *Optics Express*, no. **15**, pp. 6044-6052, 2007.
- [120] R. Shafiiha, D. Zhenf, S. Liao, P. Dong, H. Liang, N. Feng, B. Luff, D. Feng, L. Guoliang, J. Cunningham, R. Kannan, K. Ashok and M. Asghari, "Silicon Waveguide Coupled Resonator Infrared Detector," in *Optical Fiber Communication Conference*, San Diego, USA, 2010.
- [121] H.-G. Park, C. Barrelet, Y. Wu, B. Tian, F. Qian and C. Lieber, "A wavelength-selective photonic-crystal waveguide coupled to a nanowire light source," *Nature Photonics*, no. **2**, pp. 622-626, 2008.
- [122] S. Khasminskaya, F. Pyatkov, B. Flavel, W. Pernice and R. Krupke, "Waveguide-Integrated Electroluminescent Carbon Nanotubes," *Advanced Materials (accepted)*, 2014.
- [123] H. Shimizu, N. Hatori, M. Okano, M. Ishizaka and Y. Urino, "High Density Hybrid Integrated Light Source with a Laser Diode Array on a Si Optical WG Platform for Inter-Chip Optical Interconnection," in *IEEE International Conference on Group IV Photonics*, London, UK, 2011.
- [124] H. Yamada, "Analysis of Optical Coupling for SOI Waveguides," *Piers Online*, no. **2**, pp. 165-168, 2010.
- [125] X. Xu, T. Maruizumi and Y. Shiraki, "Waveguide-integrated microdisk light-emitting diode and photodetector based on Ge quantum dots," *Optics Express*, no. **22**, pp. 3902-3910, 2014.
- [126] L. Rebohle and W. Skorupa, "Rare-Earth Implanted MOS Devices for Silicon Photonics", Verlag C.H. Beck, 2010.
- [127] Y. Berencen, R. Wutzler, L. Rebohle, D. Hiller and J. Rodriguez, "Intense green-yellow electroluminescence from Tb⁺ implanted silicon-rich silicon nitride/oxide light emitting devices," *Applied Physics Letters*, no. **103**, p. 111102, 2013.
- [128] J. Sun, W. Skorupa, T. Dekorsy and M. Helm, "Bright green electroluminescence from Tb³⁺ in silicon metal-oxide-semiconductor devices," *Applied Physics*, no. **97**, p. 123513,

2005.

- [129] J. Sun, W. Skorupa, T. Dekorsy and M. Helm, "Efficient electroluminescence from rare-earth implanted SiO₂ metal-oxide-semiconductor structures," in *IEEE International Conference on Group IV Photonics*, Belgien, 2005.
- [130] S. Yerci and L. Negro, "Electroluminescence from Er-doped Si-rich silicon nitride light emitting diodes," *Applied Physics*, no. **97**, p. 081109, 2010.
- [131] W. Karthe and R. Müller, *Integrierte Optik*, Geest & Portig, 1991.
- [132] N. Daldosso, M. Melchiorri, F. Riboli, M. Girardini, G. Pucker, M. Crivellari, P. Bellutti, A. Lui and L. Pavesi, "Design, Fabrication, Structural and Optical Characterization of thin Si₃N₄ Waveguides," in *Lasers and Electro-Optics Europe 2003*, 2003.
- [133] M. Melchiorri, N. Daldosso, F. Sbrana, L. P. G. Pavesi, C. Kompocholis, P. Bellutti and A. Lui, "Propagation losses of silicon nitride waveguides in the near-infrared range," *Applied Physics Letters*, no. **86**, 2005.
- [134] S. C. Mao, S. H. Tao, Y. L. Xu, X. W. Sun, M. B. Yu, G. Q. Lo and D. L., "Low propagation loss SiN optical waveguide prepared by optimal low-hydrogen module," *Optics Express*, no. **16**, p. 20809–16, 2008.
- [135] J. Kageyama, K. Kintake and J. Nishii, "Transmission loss characteristics of silicon nitride waveguides fabricated by liquid source plasma enhanced chemical vapour deposition," *Thin Solid Films*, no. **515**, pp. 3816-3819, 2006.
- [136] J. Galan, "Addressing Fiber-to-Chip Coupling Issues in Silicon Photonics," Universidad Polit écnica de Valencia, Valencia , 2010.
- [137] J. Bauters, M. Heck, D. John and D. Daim, "Ultra-low-loss high-aspect-ratio Si₃N₄ waveguides," *Optics Express*, no. **19**, pp. 3163-3174, 2011.
- [138] D. Vermeulen, K. Van Acoleyen, S. Ghosh, S. Selvaraja, W. De Cort, N. Yebo, E. Hallynck and K. De Vos, "Efficient Tapering to the Fundamental Quasi-TM Mode in Asymmetrical Waveguides," *Optics Express*, no. **20**, pp. 13425-13439, 2012.
- [139] D.-X. Xu, A. Densmore and E. Post, "High Index Contrast Photonic Waveguide

- Components for Biological Sensing," in *210th ECS Meeting*, Mexico, 2006.
- [140] K. Luke, A. Dutt, C. Poitras and M. Lipson, "Overcoming Si₃N₄ film stress limitations for High Quality factor ring resonators," *Optics Express*, no. **21**, pp. 22829-22833, 2013.
- [141] "University, Nanyang Technological," [Online]. Available: http://homepage.ntu.edu.tw/~dwhuang/courses/sp/sp_08a.pdf. [Accessed 2014].
- [142] C.-W. Lee and M.-K. Chin, "Design of lateral-modes filter based on high-index contrast waveguides," *Optics Communications*, no. **253**, pp. 87-94, 2005.
- [143] L. Yucheng, "Choose the best element size to yield accurate FEA results while reduce FE model's compelxity," *British Journal of Engineering and Technology*, no. **1**, pp. 13-28, 2013.
- [144] S. Germer, L. Rebohle and W. Skorupa, "MOS-basierter Lichtemitter mit verbesserter Einkopplung in einen Streifenwellenleiter". Patent 6453-p1306-130514, 25 4 2013.
- [145] W. Skorupa, J. Sun, S. Prucnal, L. Rebohle, T. Gebel, A. Nazarov, I. Osiyuk, T. Dekorsy and M. Helm, "Rare earth ion implantation for silicon based light emission: From infrared to ultraviolet," *Material Research Society Symposium*, no. **V**, p. 866, 2005.
- [146] K. Lee, D. Lim, H.-C. Luan, A. Agarwal, J. Foresi and L. Kimerling, "Effect of size and roughness on light transmission in a Si/SiO₂ waveguide: Experiments and model," *Applied Physics Letters*, no. **11**, pp. 1617-1619, 2000.
- [147] J. Bauer, "Optical Properties, Band Gap, and Surface Roughness of Si₃N₄," *phys. stat. sol.*, no. **39**, pp. 411-418, 1977.
- [148] J. Galan, P. Sanchis, J. Marti, S. Marx and H. Z. L. Schröder, "CMOS compatible silicon etched V-grooves integrated with a SOI fiber coupling technique for enhancing fiber-to-chip alignment," in *Proc. IEEE International Conference on Group IV Photonics*, San Francisco/Calif., 2009.
- [149] Y. Shi, L. Zhang, P. Chen and S. He, "Fabrication of High Precision Self-Aligned V-Grooves Integrated on Silica-On-Silicon Chips," *IEEE Photonics Technology Letters*, no. **26**, pp. 1169-1171, 2014.

- [150] J. Lehmann, "Correlation between electrical and optical properties of Europium doped SiO₂-layers," Diploma Thesis, Dresden, 2009.
- [151] "Wikipedia," [Online]. Available: <http://de.wikipedia.org/wiki/Sellmeier-Gleichung>.
- [152] "Wikipedia," [Online]. Available: http://en.wikipedia.org/wiki/Atomic_force_microscopy.
- [153] A. Kenyon, "Erbium in silicon," *Semicond. Sci. Technol.*, no. **20**, pp. R65-R84, 2005.
- [154] A. Polman, "Erbium implanted thin film photonic materials," *Journal of Applied Physics*, vol. **82**, no. **1**, 1997.
- [155] Y. Vlasov and S. McNab, "Losses in single-mode silicon-on-insulator strip waveguides and bends," *Optics Express*, no. **12**, pp. 1622-1631, 2004.
- [156] R. Salh, Crystalline Silicon - Properties and Uses, In Tech, 2011.
- [157] L. Rebohle, J. von Borany, H. Fröb and W. Skorupa, "Blue photo- and electroluminescence of silicon dioxide layers ion-implanted with group IV elements," *Applied Physic B*, no. **70**, 2000.
- [158] R. K. Institut, 21 05 2012. [Online]. Available: http://www.rki.de/DE/Content/Infekt/EpidBull/Archiv/2012/20/Art_01.html.
- [159] B. f. Gesundheit, 14 12 2012. [Online]. Available: <http://www.bmg.bund.de/glossarbegriffe/t-u/trinkwasser/trinkwasserverordnung-und-regelungen-fuer-legionellen.html>.

11 SOURCE CODE MATLAB

Source code to calculate the eigenvalues (propagation constants, ERIs) for different polarizations in a planar waveguide.

```
function [beta_TE,beta_TM] = DispRel_slap%(lambdarange,d,n)
n=[1.4 2 1];
lambdarange=[1550 541];
d=1000;

if length(n)~=3
    error('n does not have a proper length!');
end;
n1=n(1);
n2=n(2);
n3=n(3);
prec = 1e-4;           %precision for beta (digits)

lauflambda=1;
for lambda=lambdarange
    k0=2*pi./lambda;
    n_high=max(n1,n3);
    beta_scan=n2*k0:-prec:n_high*k0;       %scan for guided modes
    n_high*k0<beta<n2*k0

    u=sqrt(k0^2*n2^2-beta_scan.^2);
    v=sqrt(beta_scan.^2-k0^2*n1^2);
    w=sqrt(beta_scan.^2-k0^2*n3^2);

    beta(2,1)=0;

    % case1: TE polarization
    pol='TE';
    switch pol
        case 'TE'
            q1=1;
            q2=1;
            q3=1;
        case 'TM'
            q1=n1^-2;
            q2=n2^-2;
            q3=n3^-2;
    end
    disprel = (q2.^2.*u.^2-q1.*q3.*v.*w) - (q2.*u.*(q1.*v+q3.*w)) ./
tan(u.*d);
    disprel = abs(disprel);

    beta=(zeros(length((beta_scan)-3),1));

    found=0;
    for lauf=2:(length(beta_scan)-1)
        if (disprel(lauf) - disprel(lauf-1)<0) && (disprel(lauf+1) -
disprel(lauf)>0)
            found = found+1;
            beta(1,found)=beta_scan(lauf);
        end
    end
end
```

```

% case2: TM polarization
pol='TM';
switch pol
    case 'TE'
        q1=1;
        q2=1;
        q3=1;
    case 'TM'
        q1=n1^-2;
        q2=n2^-2;
        q3=n3^-2;
end
disprel = (q2.^2.*u.^2-q1.*q3.*v.*w) - (q2.*u.*(q1.*v+q3.*w)) ./
tan(u.*d);
disprel = abs(disprel);

found=0;
for lauf=2:(length(beta_scan)-1)
    if (disprel(lauf) - disprel(lauf-1)<0) && (disprel(lauf+1) -
disprel(lauf)>0)
        found = found+1;
        beta(2,found)=beta_scan(lauf);
    end
end

% write current beta into result (transpose!)
for lauf=1:size(beta,2)
    beta_TE(lauf,lauflambda)=beta(2,lauf);           %prints only beta_TE or
TM, for TM_case change 1 into 2 and 2 into 1!
    beta_TM(lauf,lauflambda)=beta(1,lauf);
    beta_TE(lauf,lauflambda)=beta(1,lauf);
    beta_TM(lauf,lauflambda)=beta(2,lauf);
end
beta_TE(beta_TE==0)=NaN;
beta_TM(beta_TM==0)=NaN;
clear beta;
lauflambda=lauflambda+1;
end %end lamdba loop

% calculates the n_eff form beta for all modes
% TE_case

fprintf('n_eff of beta_TE: \n mode')
n_eff_TE=[(beta_TE(:,1)*1550/(2*pi))]
n_eff_TE=[(beta_TE(:,2)*541/(2*pi))]
n_eff_TE=[(beta_TE(:,3)*618/(2*pi))]
n_eff_TE=[(beta_TE(:,4)*850/(2*pi))]
n_eff_TE=[(beta_TE(:,5)*1550/(2*pi))]
% n_eff_TE=[(beta_TE(:,6)*2000/(2*pi))]

% for TM_case change only the 1 to 2 and 2 to 1 in for loop abouve and use
the fprintf line for TE!

fprintf ('hello world')

```

```
subplot(2,2,1);
plot(lambdarange, beta_TE, 'o-');
axis([500 1600 0 0.05]);
xlabel('\lambda [nm]');
ylabel('\beta [rad/nm]');
title('TE Moden');
grid on;

subplot(2,2,2);
plot(lambdarange, beta_TM, 'o-');
axis([500 1600 0 0.05]);
xlabel('\lambda [nm]');
ylabel('\beta [rad/nm]');
title('TM Moden');
grid on;

subplot(2,2,3);
plot(beta_TE, n_eff_TE, 'o-');
axis([0 0.05 1 2]);
xlabel('\beta [rad/nm]');
ylabel('n_{eff}');
title('n_{eff} of TE Moden');
grid on;

% subplot(2,2,4);
% plot(beta_TM, n_eff_TM)
% axis([0 0.02 1 2]);
% xlabel('\beta [rad/nm]');
% ylabel('n_{eff}');
% title('n_{eff} of TM Moden');

end %end function
```

12 EIDESSTATTLICHE ERKLÄRUNG

Hiermit erkläre ich, dass die Dissertation von mir selbstständig angefertigt wurde und alle von mir genutzten Hilfsmittel angegeben wurden. Ich erkläre, dass die wörtlichen oder dem Sinne nach anderen Veröffentlichungen entnommenen Stellen von mir kenntlich gemacht wurden.

Datum

Unterschrift